University of Alberta

Fatigue Rehabilitation of Coped Steel Beams Using Carbon Fibre Reinforced Polymers

by

Theresa Anne Holden

A thesis submitted to the Faculty of Graduate Studies and Research
in partial fulfillment of the requirements for the degree of

Master of Science
in
Structural Engineering

Department of Civil and Environmental Engineering

Spring 2012
Edmonton, Alberta

Abstract

Coped beams are susceptible to fatigue cracking in the web at the cope radius when subjected to tension in the coped region. Traditional repair methods such as gouging and re-welding the fatigue crack can cause residual stresses in the heat affected zone where new crack growth can be initiated. Drilling a stop-hole at the crack tip can cause a reduction in net section. Use of an adhesively bonded composite patch over the cracked area can reduce the stress concentration at the crack tip, delaying further crack growth. This research contains the results of a full-scale experimental study on the fatigue mitigation of coped beams using Carbon Fibre Reinforced Polymer (CFRP) patches. Six coped beams were tested. The specimens were pre-cracked to 10 mm prior to repair. Three of the specimens had three layer patches of different configurations of SikaWrap Hex 103C applied to one side. Two specimens had six layer patches; one with all six layers applied to one side, while the other had three layers applied to each side of the web over the crack. The sixth specimen remained unrepaired as a control specimen. This study showed that the single sided repairs provided a marginal increase in fatigue life over the unrepaired beam. The double sided repair was found to increase the fatigue life over three times the fatigue life of the unrepaired specimen. A small-scale experimental study of the effects of varying the pre-crack length prior to specimen repair was also conducted. It was found that the CFRP patch is much more effective at smaller pre-crack lengths. An analytical study of the fatigue mitigation method is also investigated.

Table of Contents

List of Tables

List of Figures

1 Introduction

Canadian infrastructure is aging. A large number of North American bridges are approaching the end of their design lives. In 2007, more than 40% of Canadian bridges were over 50 years old (Hammad, Yan and Mostofi 2007), while the average age was 24.5 years (Gagnon, Gaudreault and Overton 2008).

As urban centres grow, many bridges are also experiencing more and heavier traffic than accounted for in their original designs. It is economically infeasible to replace all aging and overloaded bridges. A more cost-effective solution is to find methods to extend the design lives of existing bridges. This can be done through rehabilitation and repair. Rehabilitation schemes may include strengthening or repair of structural members which contain moderate to light fatigue damage or understrength, and replacement of others which are beyond repair. This is an emerging market in the steel construction industry.

Fibre Reinforced Polymers (FRPs) are a composite material which contains fine synthetic fibres, such as aramid, glass or carbon, of within a polymer matrix. FRPs are a strong, lightweight material. Because the material is entirely manmade the strength and modulus of elasticity can be made to order. FRP strength and modulus of elasticity can exceed those of steel, depending on the type of fibre used or the composition of the material. Adhesively bonded to steel, FRPs can be used to increase the overall strength of a member. Adhesively bonded over a fatigue crack, they can also slow crack growth.

Coped beams are steel I-shaped beams which have had one flange cut away (Figure 1-1). This can be done to create a flush fit with another member to which it is attached. Flush fit is important to create a flat surface on which to lay a floor or roadway, or from which to hang a ceiling.

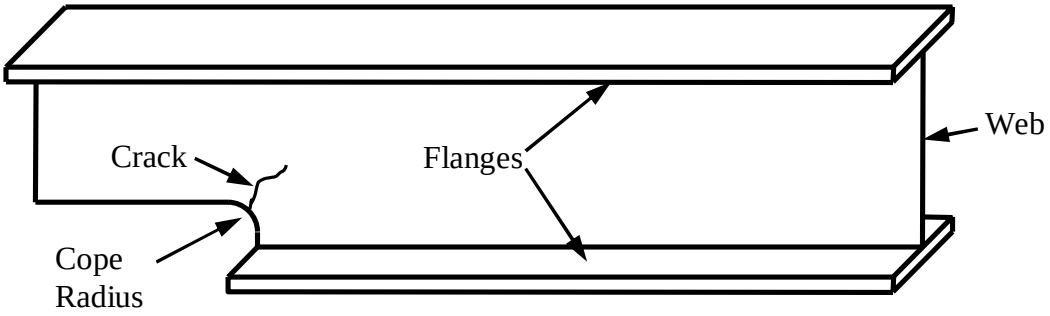

Figure 1-1 Coped beam

The change in geometry of the beam creates a stress concentration at the cope radius. This intensifies any stresses in that region. When the beam is loaded with gravity loads, it goes into bending, which would put the bottom flange into tension. It has been shown, however, that if the connection to the adjacent girder or column is sufficiently rigid, a point of inflection may occur putting a top flange cope in tension. When the cope is subjected to cyclic tensile loading, the stress concentration at the cope may be sufficient to create a fatigue crack initiation point.

The fatigue behaviour of coped beams is relatively well understood. Yam and Cheng (1990) conducted a series of full-scale tests on coped beams to determine the effects of a cope detail of a beam under cyclic loading. They recommended using Category C of the S-N curves in CAN/CSA S16-06 (2006) combined with the stress concentration factor at the cope region when designing coped beams for fatigue.

FRPs have been successfully applied to extend fatigue life in steel in several experiments. These experiments have all used composite patches on steel in under pure tension loading; either in small-scale coupons or on the bottom flange of a beam in positive bending (Zhao and Zhang 2007). In all cases, the fibre direction is aligned perpendicular to the direction of crack growth to obtain optimal FRP strength. The web of a coped beam, where a fatigue crack would initiate, has a much more complex stress state. The web is subject to variable

tension stresses as well as shear stresses. This makes the angle of fatigue crack propagation less predictable. Orientation of FRP for optimal strength is more difficult.

1.1 Objective and Scope

Carbon fibre reinforced polymers (CFRPs) are FRPs in which the main fibre used is made of graphite or carbon. CFRPs are resistant to corrosion and can be made with strength and stiffness similar to steel. CFRPs are less expensive than composites with aramid fibres, and they are typically stiffer than those made with glass fibres. For these reasons, CFRPs are the type of composite material considered in this study.

The objective of this project was to determine the effectiveness of a CFRP patch for fatigue repair of coped beams. Six full-scale specimens were tested. The parameters under consideration included eccentricity of repair (single sided vs. double sided); orientation of repair; and effective thickness ratio (ETR).

The tests took into account the stress ranges ($\Delta\sigma_n$) typical of those seen in bridge girders. $\Delta\sigma_n$ was chosen as 80 MPa. This value should be representative of the values seen on a typical bridge member in Alberta, based on the current bridge design criteria (Alberta Infrastructure and Transportation 2007), and the current bridge design standard CAN/CSA S6-06 (2006).

1.2 Organization of Thesis

Chapter 1 consists of the introduction to the project and objective and scope of the experiment. Chapter 2 details previous works in coped beams and the area of FRP repairs on steel structures and fatigue cracks.

The main experimental work for this project is presented in Chapters 3, 4 and 5. Chapter 3 presents the test methodology and an in-depth examination of the parameters studied. The results of the experiment are presented and discussed in

Chapter 4. An analytical model of fatigue life prediction for the repair method is presented in Chapter 5.

Chapter 6 presents a complementary experimental study on the effect of varying pre-crack length. This study used small-scale specimens under direct tensile loading.

A summary of all works is presented in Chapter 7. This chapter also contains conclusions drawn and recommendations for future study in the area.

2 Previous Works

2.1 Coped Beams

Yam and Cheng (1990)[1] did extensive experimental, analytical and finite element modelling work to understand the fatigue behaviour of coped steel beams. They tested nine coped W410 x 54 steel specimens under three-point bending. Figure 2-1 shows the experimental set-up and instrumentation for the experiment. In addition to the instrumentation shown, longitudinally oriented strain gauges were applied along the central axis of the beam on the top and bottom flanges at a cross section 720 mm from the cope.

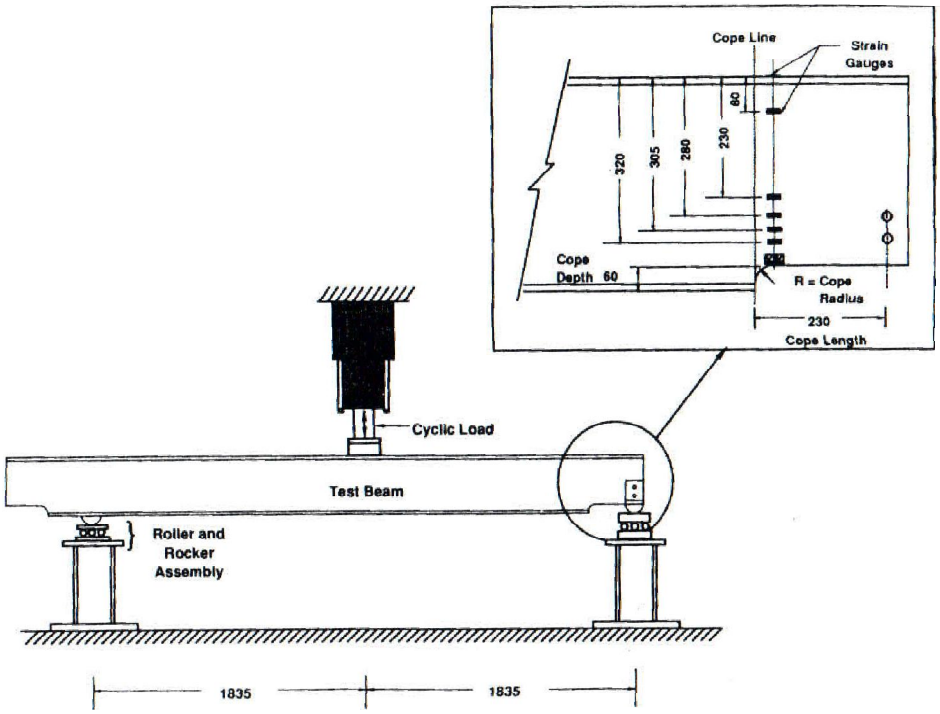

Figure 2-1 Coped beam experimental set-up (Yam and Cheng 1990)

The specimens were tested at a cyclic rate of 3 to 5 Hz. Table 2-1 shows the test matrix. The parameters varied in the experiment were cope radius, stress range,

[1] The Journal of Structural Engineering article cited here is based on work done by Yam and Cheng in Yam's Master's thesis (Yam and Cheng, SER 160 1988). Much of the data and results contained in the thesis were republished in this article. Some of the data used in the research for this report, however, was not republished. In all cases where the data is available in both the thesis and article, the article is cited; otherwise SER 160 is cited.

and cope surface preparation. The beams coped by flame cut (F), flame cut and ground smooth (FG) and by drilled hole and cut (D). The nominal cope radii listed are the intended radius for the beam. The flame cut fabrication method caused distortions in the steel which increased the actual radius somewhat. The nominal stress ranges at the cope were 45, 50 and 70 MPa.

Table 2-1 Coped beam experimental matrix (Yam and Cheng 1990)

Specimen Designation	*Nominal Cope Radius (mm)*	*Actual Cope Radius (mm)*	*Nominal Stress Range (MPa)*	*Fabrication Procedure*
CB-0	0	0	50	F
CB-10A	10	15	50	F
CB-20B	20	25	50	FG
CB-20A	20	25	50	F
CB-30	30	32	50	F
CB-10B	10	15	40	F
CB-10C	10	15	70	F
CB-10D	10	15	70	FG
CB-10E	10	10	70	D

Table 2-2 shows the experimental results of the study. The stress range had a large effect on the crack growth rate. CB-10B, with a nominal stress range of 40 MPa, had a fatigue life to a 30 mm crack length that was 3.2 times greater than CB-10C which had a nominal stress range of 70 MPa. The cope radius was also found to have a large effect. CB-30 with a 32 mm measured cope radius had a fatigue life to a 30 mm crack length that was 8.6 times greater than CB-0 with a square cope and 3.4 times greater than CB-10A with a 15 mm cope. The effect of fabrication method from this experiment was inconclusive.

The effect of grinding the cope smooth produced a drastic 8.0 times increase in fatigue life of CB-20B over CB-20A, but produced only a marginal 1.1 times increase in the fatigue life of CB-10D over CB-10C. Drilling the hole decreased the fatigue life. This can be attributed partially to the fact that the actual cope radius is smaller for the drilled specimen.

Table 2-2 Experimental results (Yam and Cheng 1990)

Specimen Designation	*Nominal Stress Range (MPa)*	*Crack Location (mm)*	*Cycles to failure*	*Cycles to 30 mm crack*
CB-0	50	0	297,000	165,500
CB-10A	50	9.98	575,200	405,800
CB-20B	50	12.09	8,944,700	8,632,000
CB-20A	50	16.23	1,295,300	1,080,000
CB-30	50	2.89	1,657,900	1,390,000
CB-10B	40	4.81	1,335,600	928,000
CB-10C	70	6.47	437,800	292,500
CB-10D	70	7.53	400,900	318,600
CB-10E	70	4.00	269,000	211,500

Finite element models of the beam were created to determine the stress concentration factor in the coped region (Yam and Cheng 1988)[2]. The stress concentration factor was then included in a stress gradient correction factor using Green's function. This was then applied to an analytical Linear Elastic Fracture Mechanics (LEFM) model to predict the fracture behaviour of the cracks. The LEFM model was limited to a crack length of 30 mm. The crack length limit was chosen because LEFM is more reliable with shorter cracks, and 30 mm is easily detectable by visual inspection.

Table 2-3 shows the results of the analytical model in comparison with the experimental results. The initial crack length of one millimetre was chosen for CB-10A based on an observed notch in the specimen at the location of fatigue crack initiation. The remainder of the specimens were modelled with an initial crack size of 0.38 mm based on the assumed depth of the martinsite layer due to flame cutting. These assumptions yielded a test to predicted ratio between 0.37 and 0.75.

Yam and Cheng compared the results of the experimental data to the existing categorization of S-N curves, which is in use today in CAN/CSA S6-06 (2006). To account for the variability due to cope radius, the theoretical stress range was

[2] The stress concentration factor gradients were not published in the 1990 paper, and are only available in SER 160, published in 1988.

used to plot the S-N curve. They determined that though the use of category B produced reasonable predictions of fatigue life, due to scarcity of data, category C should be used to predict the fatigue life of coped beams.

Table 2-3 Comparison of fatigue life predictions by Green's Function method (Yam and Cheng 1990)

Specimen Designation	*Theoretical Stress Range (MPa)*	*Initial Crack Size (mm)*	*Predicted Fatigue Life to 30 mm*	*Measured Fatigue Life to 30 mm*	*Test to Predicted Ratio*
CB-10A	200	1.00	244,800	405,800	0.60
CB-10B	160	0.38	698,900	928,000	0.75
CB-10C	280	0.38	108,300	292,500	0.37
CB-10D	280	0.38	131,700	318,600	0.41
CB-10E	314	0.38	121,900	211,500	0.58
CB-20A	173	0.38	479,000	1,080,000	0.44
CB-30	164	0.38	713,800	1,390,000	0.51

Cheng (1993) presents a design model for coped beams which encompasses formulae for lateral torsional buckling of unbraced coped beams; local buckling in the compression flange and in the web at the coped section; and fatigue design. Equation [2-1] was proposed to correlate stress concentration factor to cope radius.

$$log(SCF) = 0.937 - 0.285(R) \qquad \textbf{[2-1]}$$

where SCF is the stress concentration factor at the cope and R is the cope radius. This equation was determined by fitting a logarithmic curve to stress concentration factors determined by finite element modelling. The stress concentration factors were determined for coped beams with cope radii of 10 mm, 15 mm, 20 mm, 25 mm, and 30 mm. Use of doubler plates and cope stiffeners was also recommended to mitigate fatigue.

Roeder et al. (2005) performed an experimental study of fatigue mitigation methods on coped beams. Sixteen W21 x 62 (W530 x 92 metric) specimens were prepared with copes on the upper flanges. These beams were then rigidly

attached to a strong wall and loaded cyclically at 2 Hz. The rigid attachment created a small negative moment region at the connections, putting the top flange cope into tension. Crack mitigation methods used included drilled stop-hole; drilled stop hole with pretensioned bolt, and reducing the shear connection stiffness by removal of shear connection bolts. Three cope details were employed for the study: square cut, at 22 mm radius flame cut, and notched 22 mm radius flame cut.

The researchers found that the surface roughness of the cope radius had a large effect on fatigue crack initiation. Rough and notched copes generated cracks much more quickly, consistent with fatigue category E', while smooth radius copes were consistent with fatigue category D. These results are specific for the 22 mm radius cope from the experiment. They also found that the connection stiffness to the strong wall affected the cope stress and consequently the crack growth rate. Secondary crack growth was observed in the stop-hole specimens, with a marginal increase in fatigue life. Insertion of a pretensioned bolt in the stop hole effectively controlled crack growth. Cracks were observed in washers under the nut and bolt head prior to detection in the steel, acting as warning indicators for further crack growth. In some cases the stop hole with inserted bolt effectively stopped crack growth at that location, only to have secondary cracks initiate at other locations. Reducing the rigidity of the connection to the strong wall was the most effective fatigue crack mitigation method. It effectively stopped crack growth by eliminating the negative moment region.

2.2 FRP in Steel Strengthening

Kennedy and Cheng (1998) conducted an experimental study of eleven specimens centre cracked and repaired with a single sided CFRP patch. The schematic for the specimens is shown in Figure 2-2. The patches were varied by width, length, number of layers, and end taper and shape. All steel specimens were 400 mm x 750 mm x 6.35 mm. The plates were prepared with a central crack of 80 mm in length. The effect of the CFRP patches on the strain distribution at the crack tip

was examined. The researchers found that the stress concentration at the crack tip was reduced by application of a patch. The stiffness of the patch with respect to the steel affected the reduction in stress concentration. A stiffer patch reduced the stress concentration at the crack tip; however, a less stiff patch reduced stress concentrations at the ends of the patch. The researchers also observed out-of-plane bending in the specimens due to eccentricity of load distribution from the single sided patch.

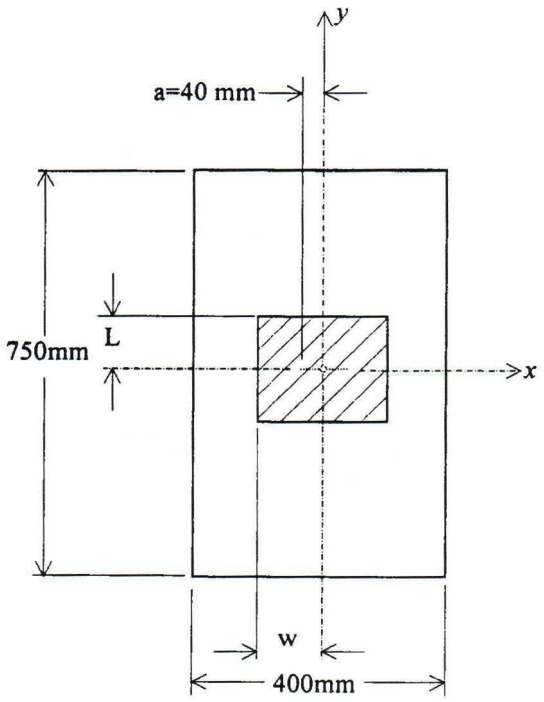

Figure 2-2 Schematic of bonded patch test specimen (Kennedy and Cheng 1998)

Lam et al. (2007) performed an experimental study of nineteen steel double-lap joint specimens. The specimen width, thickness, CFRP type, taper, lap length and number of layers were varied. Variation of steel thickness, CFRP type and number of layers resulted in a variation of Effective Thickness Ratio (ETR) (Equation [2-2]) :

$$ETR = \frac{E_{CFRP} t_{CFRP}}{E_S t_S} \quad \textbf{[2-2]}$$

where E_{CFRP} is the modulus of elasticity of the CFRP patch, E_S is the modulus of elasticity of the steel adherend, t_{CFRP} is the cumulative thickness of CFRP patches and t_S is the thickness of the steel adherend.

All specimens failed by debonding of the CFRP patch. The researchers observed similar behaviour in the different types of CFRP patch. Brittle failure was observed in specimens with short lap length. The axial capacity of the patch increased with lap length until a threshold lap length was reached, at which the axial capacity reached constant. Axial load carrying capacity increased with patch thickness for specimens with the same steel thickness. Researchers also noted that the end taper had virtually no effect on the axial load carrying capacity. The researchers also created a nonlinear finite element model which predicted the axial carrying capacity of the specimens to within 14% accuracy.

Phoutiou et al. (2006) tested HSS 120 x 80 x 5 mm rectangular hollow sections in bending about the strong axis to determine the effectiveness of a CFRP strengthening system. The bottom flanges of the sections were milled to half their original thickness to ensure a tensile failure mode. The specimens were then repaired with High Modulus (HM) and Ultra High Modulus (UHM) CFRP. Flange width and U-shaped patch configurations were used. Both configurations consisted of alternating layers of GFRP and CFRP with the first GFRP layer adjacent to the steel. All GFRP layers were single-ply with fibre directions ±45°. The CFRP was applied as a double-ply laminate with fibres in the longitudinal direction. In the flange width configuration, all layers extended only to the edge of the bottom flange, while in the U-shaped configuration, the GFRP layers extended to the neutral axis of the beam.

For the HM repairs, the behaviour of the beams was nearly identical. The ultimate load capacity of the repaired beams was greater than the original

undamaged capacity of the beams and full ductility was achieved without fibre breakage. For the UHM repairs, the behaviour of the beams was nearly identical in the first loading cycle. On the U-shaped patch, the FRP failure was localized with no apparent debonding of the patch away from the failure site. The flange width repair, however, experienced catastrophic debonding of the FRP patch. On the second cycle, applied after FRP failure, the UHM U-shaped repair showed some continued composite action, while the UHM flange width repair exhibited only the response of the steel. All four upgraded beams reached the plastic collapse load for the undamaged/unrepaired steel beams. UHM beams failed as a result of fibre breakage, while HM exhibited ductile response. By applying a U-shaped repair, failure was localized in the fibre breakage zone, and did not lead to catastrophic debonding such as was seen on the flange only repairs.

Many other experiments have been conducted on the use of CFRP in steel strengthening. Zhao and Zhang (2009) did a state of the art review of FRP strengthened steel structures. They classified the specimens by type of FRP, size of specimen, type of bond and type of joint. They found that the majority of experiments for FRP used in steel strengthening were done on small-scale coupon type specimens in uniaxial tensile loading. A few full-scale experiments had also been done, but those all consisted of FRPs applied to the tensile flange of a beam in bending. None of the experiments examined had been performed with the intent of strengthening a member loaded in shear. Most specimens were found to fail by the mechanism of adhesive debond at the steel-FRP interface. This shows a concern for the type of adhesives being used and the possibility of creating an effective bond to steel. Chalmers University of Technology has also done extensive work in this field from small-scale specimens to full-scale specimens to finite element modelling (Linghoff, Hagani and Al-Emrani 2009).

Testing has also been conducted on adhesive bond between steel and CFRP (Deng and Lee 2009) and effective splice methods for CFRP (Dawood, Guddati and Rizkalla 2009). These tests focussed on optimizing the strength of the bond, and

minimizing the stress concentrations within the bond by varying the surface treatment, configuration, and epoxy.

2.3 FRP in Fatigue Repair – Small-Scale Testing

The majority of CFRP testing on steel has been conducted on small-scale specimens loaded uniaxially. This is an ideal testing scenario. The load application and direction are easily controlled. From these tests, basic understanding of the behaviour of CFRP repairs on steel was gained.

Jones and Civjan (2003) performed fatigue tests on 29 specimens. The specimens were A36 steel bars 510 mm x 51 mm x 6.5 mm thick. These were machined with either a centre notch or an edge notch. The researchers varied the lap length, number of layers and number of sides to which the repairs were applied. Two types of patch were used. These were Sika Carbodur paired with Sikadur 30 epoxy or Sika Wrap Hex 103C paired with Sikadur 300 epoxy. The specimens were loaded uniaxially in tension at 25 Hz with a load range of 37.4 kN. An increase in fatigue life of 170 % was observed on four pre-cracked specimens. Out-of-plane bending was observed on the single sided repair specimens. All failures were initiated by CFRP patch debonding. The Carbodur/Sikadur 30 repair was found to have virtually no advantage over bare steel. The researchers postulated this was because the Sikadur 30 adhesive was designed to bond to concrete or masonry, not to steel. A finite element model was also done for the specimens. Based on the model, it was predicted that using higher ETRs would yield an increase in fatigue life.

Bocciarelli et al. (2009) performed an experimental fatigue study of strengthened steel plate. The plates in question were uncracked, 100 mm x 50 mm x 6 mm. The specimens were patched on both sides with full-width Sika Carbodur plates bonded with Sikadur 30 epoxy. The specimens were loaded cyclically at stress ranges of 83 MPa, 100 MPa, 120 MPa or 160 MPa. The chief failure mechanism observed was CFRP debonding beginning at the plate ends, and debond propagation along the plate. Debond was observed to take place at the end of the

CFRP plate where the thickness of the adhesive appeared to be thinner. The debonding also tended to occur at the steel-adhesive interface. Fatigue debonding appeared in the data as a progressive loss of stiffness in the specimen. A 2% loss in stiffness corresponded with debond initiation and a 5% loss in stiffness indicated the beginning of rapid debond progression. The overall member stiffness dropped to 85% when debond reached midspan. The researchers concluded that the fatigue resistance of adhesively bonded CFRP plate was competitive with welded steel cover plates.

Lui, Al-Mahaidi and Zhao (2009b) tested 21 specimens, 500 mm x 90 mm x 10 mm, machined with a central notch in the transverse direction of the plate. Both one-sided and two-sided repairs were tested. The patch configurations tested were: no repair; full width repair covering the central notch; one partial width patche covering the central notch; and two partial width patches, located on either side of the notch, not extending to the edge of the plate or covering the centre notch. The bond length and width were varied, as was the repair material and number of layers of repair. One layer of GFRP was applied between the CFRP repair and the steel to reduce galvanic corrosion and to enhance bond performance. Specimens were cyclically loaded with minimum and maximum loads of 13.5 kN to 135 kN applied in a constant amplitude sine-wave and periodically beach marked by a reduced stress range over a number of cycles. All specimens repaired with normal modulus CFRP failed by interfacial debonding. Specimens repaired with high modulus CFRP failed by fibre breakage. An asymmetrical crack front was observed on single-sided repairs, demonstrating out-of-plane bending moment due stress path eccentricity. Fatigue life increased 2.2 to 2.7 times for specimens repaired on one side and 4.7 to 7.9 times for specimens repaired on both sides. High modulus were repairs more efficient to extend fatigue life. Bond length did not significantly affect fatigue life beyond a threshold value. Longer bond widths were found to increase fatigue life. Repairs covering the centre notch were more effective than those not covering the centre

notch for one sided repairs, but no significant effect was obseved for two-sided repairs.

Taljsten, Hansen and Schmidt (2009) did a similar experiment on centre notched specimens with patching to either side of the notch. The specimens were fabricated from the webs of old bridge girders and dimensioned 670 mm x 205 mm. The CFRP laminate, adhesive and prestressing tension were varied. Increases in fatigue life of 8 to 34 times the unrepaired value were observed in the prestressed specimens and 2.5 to 3.7 times the unrepaired value for non-prestressed specimens. The variability in fatigue life was accounted for by observed out-of-plane bending in the specimens which occurred during fabrication and possible misalignment of the laminates and adhesives during curing.

2.4 FRP in Fatigue Repair – Full-Scale Testing

Large scale tests for fatigue repair of steel using FRPs have also been done. The most common configuration is for the application of the repair on the tension flange in the constant moment region of a beam in four-point bending (Figure 2-3).

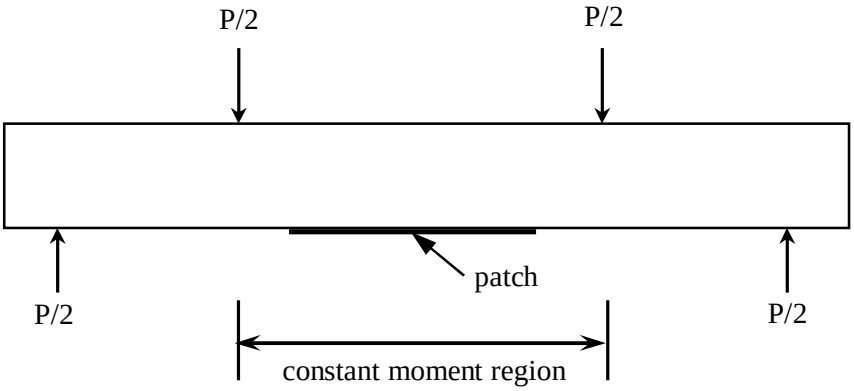

Figure 2-3 Four-point bending

Tavakkolizadeh and Saadatmanesh (2003, 2003a, 2003b) conducted a series of experimental tests on the strengthening and repair of steel-concrete composite girders. While these were full-scale tests, the repairs took place only in the

longitudinal direction on the tension flange of the steel girders. The work was expanded to include fatigue repair of the steel-composite girder system. The fatigue specimens were machined with a cut in the flange, over which the repair was applied. The specimens were then loaded in four-point bending. The researchers observed an increase in fatigue life of up to 3.4 times and longer crack lengths prior to loss of stiffness for the repaired specimens. The increase in fatigue life was deemed to be equivalent of increasing the detail from AASHTO category D to category C. The slope of the S-N curve, however was smaller than the slope used in the AASHTO design curves, therefore no definite fatigue category was applied. The repaired specimens were found to have a more ductile behaviour, carrying load for a few more cycles after the fatigue crack had propagated through the flange.

Dawood, Rizkalla and Sumner (2007) did a similar experiment, expanding it to include fatigue overloading of strengthened steel-concrete composite girders. The test was taken to three million cycles at 20% simulated overload. The researchers found that the application of a CFRP patch for strengthening the undamaged structure reduced the residual deflection after overloading. The reduction in residual deflection was projected to minimize the need for replacement and repair of the structure in use.

Basetti et al. (2000) performed full-scale fatigue testing of riveted bridge girders with the tension flange repaired using prestressed CFRP. Use of prestressed CFRP patching on the tension flange gave an essentially infinite extension to the fatigue life of the specimen over unrepaired girders from the same bridge. This experiment also considered application of the CFRP to a uniaxial tension loaded element of the beam.

2.5 Finite Element and Analytical Modelling of FRP Repairs

Naboulsi and Mall (1996) proposed a three layer model for modelling of a single-sided FRP repair using Mindlin plate theory. The three layers of FRP, adhesive

and steel substrate were all modelled as shell elements with specific geometric conditions applied at the interfaces. These geometric conditions could be changed depending on the properties of the system being modelled. For example, the geometric conditions linking the adhesive to the steel plate could be deleted in the case where an adhesive debond has occurred in the system. The researchers classified cracks in a system as adhesive or cohesive, with cohesive cracks being through thickness cracks in the steel plate, while adhesive cracks are any cracks in the adhesive or FRP which would cause debond of the repair from the steel. A system was developed to determine the stress intensity factor at both adhesive and cohesive crack tips. The researchers concluded that the three layer model gave results with minimal difference in results to a three dimensional model

Liu, Zhao and Al-Mahaidi (2009a) performed a three dimensional boundary element analysis of steel plates reinforced with CFRP. In this model, the CFRP and steel layers were modelled as surface elements and the adhesive a springs. The researchers varied the patch configuration, length and width; the number of layers of CFRP; the elastic modulus of CFRP and the shear modulus of the adhesive. From this model, the researchers concluded that the presence of a patch would reduce the stress intensity factor (SIF) at the crack tip, thereby increasing the fatigue life. Wider patches were determined to be more effective at reducing the SIF. Increasing the length of patch increased the fatigue life up to a threshold patch length, past which there was no obvious fatigue life increase gained. Increasing the elastic modulus or number of layers of CFRP was both found to decrease the SIF at the crack tip. Increasing the shear modulus of the adhesive was also found to significantly reduce the SIF, however the rate of reduction was found to be less significant with shear moduli above 700 MPa.

Liu et al. (2009c) also created an analytical fracture mechanics model to predict the fatigue life of steel plates repaired with CFRP. The model incorporates both single- and double- sided repair. It takes into account the crack closure effects as well as the effects of out-of-plane bending due to asymmetry of single sided repairs. Assuming that out-of-plane bending effects counteracted the crack

closure effect was found to be an efficient assumption. The model results have shown good agreement with experimental results (Liu, Al-Mahaidi and Zhao 2009b)

Lam et al. (2010) conducted extensive finite element analysis based on single sided CFRP repair of cracked members. The purpose of this study was to determine the exact change in stress intensity factor (SIF) at the crack tip and use it to predict the fatigue life of various members. The researchers compared the results from a three layer model (Naboulsi and Mall 1996) and modified three layer model of the CFRP, adhesive, and steel plate. In the modified three layer model, the steel was modelled as brick elements, while the adhesive and CFRP layers were modelled as shell elements, as shown in Figure 2-4. The model varied the patch length, width, taper, number of layers of CFRP repair and elastic modulus of CFRP repair.

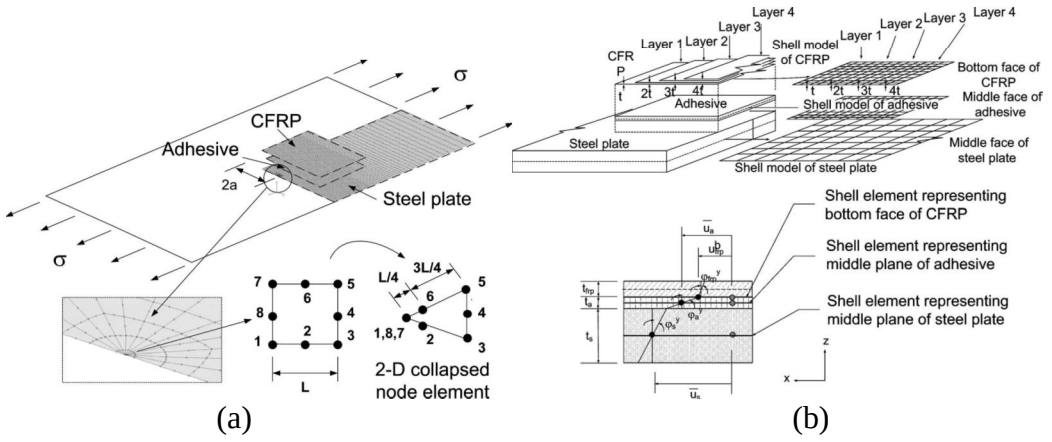

Figure 2-4 (a) Three layers model and (b) Modified three layers model (Lam et al. 2010)

Figure 2-5 shows a comparison of the two models. The researchers found that a single sided repair significantly decreased the stress intensity factor of a cracked member. For a cracked plate, the out-of-plane bending induced in the member from the eccentricity of the repair was found to cause a slight increase in SIF at the crack tip. This increase was not as apparent in the three layer model.

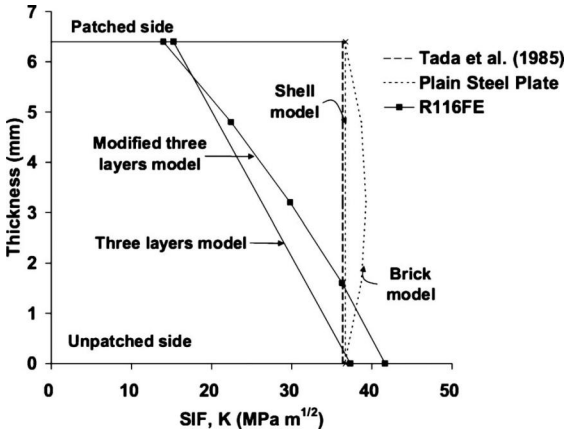

Figure 2-5 Comparison of SIF for three layers model and modified three layers model (Lam et al. 2010)

The researchers also provided a case study which applied the modified three layers model to a CFRP repair on a cracked tubular member. For a cracked tubular member, however, the geometry of the member prevented significant out-of-plane bending. This gave a significant decrease in SIF on both the patched and unpatched sides. The patch length and width had only a marginal effect on the stress intensity factor with the ETR giving a much more significant change in SIF. The researchers recommend a minimum patch width of double the crack length. A much higher ETR is also recommended for single sided repair of plate members to counteract bending effects.

2.6 Galvanic Corrosion

Galvanic corrosion is a concern when using a CFRP repair on steel in a moist environment. Graphite, the form of carbon used for the fibres in CFRP, is a noble conductive material (Roberge 2008) and acts as a cathode when connected to steel. One main concern is how to mitigate or prevent galvanic corrosion in this type of repair, particularly in outdoor and marine environments. All galvanic cells require four things: anode, cathode, an electrical connection between the two, and moisture. If one of these four elements is eliminated, galvanic corrosion cannot occur.

Whether in a marine environment, over freshwater, or simply as a highway overpass, Canadian bridges are exposed to both water and salt. Sodium Chloride and Calcium Chloride are the two most commonly used de-icers on Canadian highway bridges and overpasses (Environment Canada and Health Canada 2001). When exposed to water, this creates an ionic solution which is an aggressive corrosion environment. Further, the moisture is one of the essential elements in a galvanic half-cell, as listed above. Several tests have been done on exactly what the galvanic effects are of direct connection between metals and CFRP in a marine environment.

Tucker and Brown (1989) performed an experiment to determine the effect of stressed CFRP galvanically coupled to steel. CFRP samples were machined from two different types of cross-ply composite materials. The first CFRP system consisted of hand lay-up of a prepreg graphite fibre tape with an ester vinyl resin, while the second system consisted of a Narmco system designated T300/5208 for Union Carbide T300 fibres in Narmco 5208 Resin. The specimens were machined to 8" x ½" x 3/8" (203.2 mm x 12.7 mm x 9.5 mm) according to ASTM D790. They were then preconditioned according to ASTM D618. Five samples of each composite were placed on an acrylic plastic bridge and stressed using a c-clamp (Figure 2-6). The stressed samples were then submerged in natural filtered seawater and samples taken after one week, one month, three months and six months. Control samples of CFRP were also placed in the tank with no stresses applied and no galvanic connection to steel.

The experiment was originally intended to observe the effects of CFRP under constant strain in a saline environment. However after the first week of the test, the clamps were observed to be experiencing severe corrosion. This corrosion was deemed to be due to galvanic coupling with the CFRP. The rate of corrosion was so severe that the six month samples were galvanically isolated from the clamp by use of an acrylic plastic pad between the clamp and the CFRP. All one week, one month, and three month samples, which were galvanically connected to the steel, exhibited growth of aragonite crystals. The galvanically connected

samples with the ester resin experienced both blistering and crystal growth. The six month sample, which was stressed but not galvanically connected to steel, experienced neither blistering nor crystal growth. The control samples, which were neither galvanically connected nor stressed, also did not experience any blistering or crystal growth.

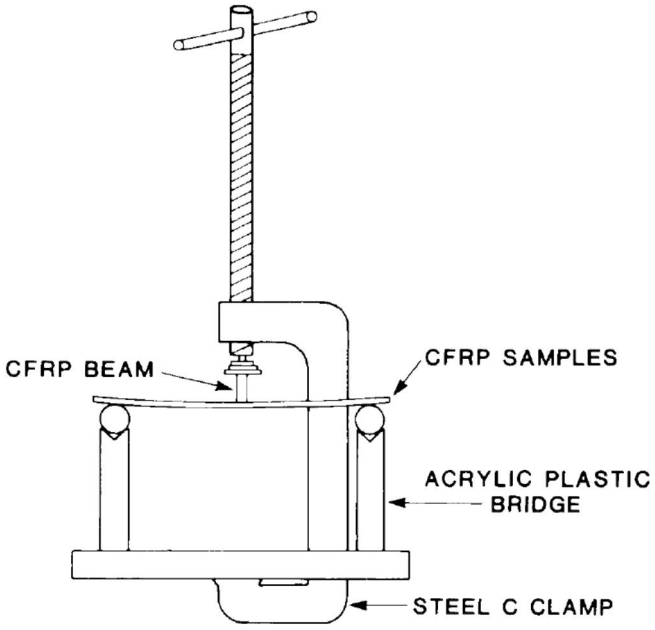

Figure 2-6 CFRP stressing test setup (Tucker and Brown 1989)

Blistering is a common phenomenon on glass fibre/polymer composites in marine environments. It is described as growth of fluid filled bubbles within the polymer matrix. This is caused by osmotic pressured drawing water into the resin. When the osmotic pressures rise above the failure pressure of the resin, blisters form. The fluid in the blisters tends to be highly acidic due to the dissolution of water soluble components of the resin. Aragonite crystal formation is caused by local changes in the pH of the water.

Tucker et al. (1990) performed tests coupling CFRP composite to various metals exposed to natural seawater. The specimens consisted of one-inch square by ¼ inch thick (25.4 mm x 25.4 mm x 6.4 mm) samples of CFRP joined to metal samples of the same size. Slots were machined into the graphite fibre to

accommodate the metal samples. Metals used were stainless steel, monel, pure grade titanium, and Al 2014 with and without a hard anodized coating. The samples were then submerged in natural seawater in two locations. The first group was submerged into filtered seawater in the lab and the second group was submerged directly into the ocean. Visual examination was done frequently over the six month test period.

Only the stainless steel results are reported here as the other results are not relevant to this report. Stainless steel had different corrosion deposit patterns in the lab sample and the ocean sample. On the lab sample, rust was evident at the interface between the carbon and steel, where in the ocean sample the visible extent of the corrosion was not as great. The researchers postulate this is due to the motion of the seawater removing the corrosion products as they form. Crevice corrosion was evident in both samples. Aragonite crystal deposits were observed on the CFRP surface on the laboratory sample. Detection of similar crystal deposits as impossible on the oceanic sample due to marine growth on the surface of the CFRP. The researchers postulate the crystal formation is due to local pH changes in the seawater caused by corrosion.

Sloan and Talbot (1992) tested 40 specimens of 26 ply isotropic T-300/934. The purpose of the tests was to determine the effects of galvanic corrosion on the CFRP composite material itself. The specimen dimensions were 76 mm x 13 mm x 3.6 mm for the eight control and sixteen soaked specimens. The galvanically coupled specimens, however, were cut to 90 mm x 13 mm x 3.6 mm. The added length was necessary to accommodate a drilled hole for galvanic connection to the magnesium sacrificial anode. The eight control specimens were placed in a sealed plastic bag. Eight specimens each were completely immersed in 2L tanks filled with pacific sea water and tap water at 40°C. The remaining sixteen specimens were each galvanically coupled to a magnesium rod sacrificial anode, attached to a corrosion rack, and suspended in a separate seawater tank (Figure 2-7(a)). Weights of all specimens were taken prior to immersion, periodically during the test, and at the end of the test. The periodic weighing was done with

surface dry specimens, whereas at the end of the test the specimens were baked in a drying oven at 200°C for several days until the daily weight loss was less than 0.1%. All specimens were then tested in four-point bending (Figure 2-7(b)) with an L/h ratio of 12 to ensure failure by interlaminar shear. The bending tests were done to determine changes in strength caused by chemical changer during corrosion.

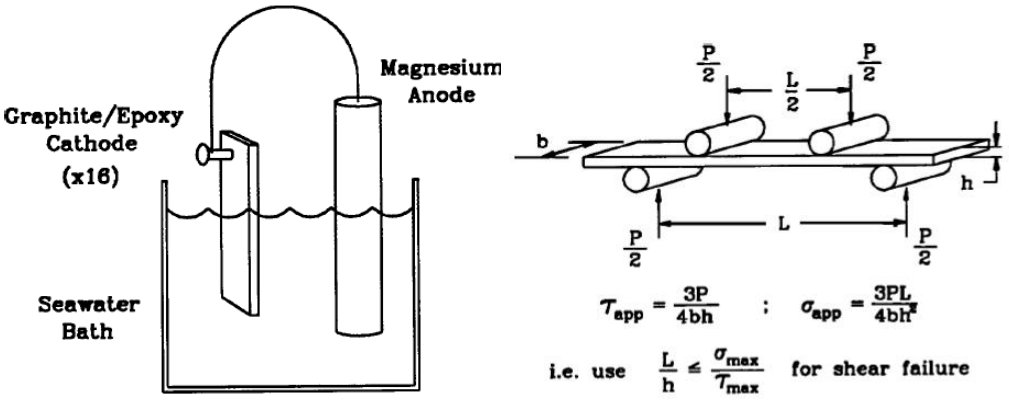

a b

Figure 2-7 Schematic of test setup for a) galvanic corrosion and b) four-point bending (Sloan and Talbot 1992)

The researchers found that after drying, the soaked specimen weights were higher than the control, which had a net weight loss of 2.13%. This was attributed to the formation of a small layer of deposits formed on the specimens, and from absorbed moisture. The corrosion specimens showed a decrease in overall weight after baking and with deposit formations removed. In this case, the loss of weight was attributed to a leaching mechanism in the electrochemical environment. The researchers also postulated that since the drying temperature was 20°C higher than the epoxy curing temperature, possible post-cure reactions may cause evaporation of volatile epoxy components which may be mistaken for moisture content.

The soaked specimens showed no significant change in shear strength, but a slight increase in shear strength data scatter. A 30% loss in shear strength was also

observed in the galvanically active specimens. This loss was caused by localized corrosion in the composite. Delaminated areas spreading from the specimen edges reduced the effective width of these specimens by 20% to 40%. When viewed under a scanning electron microscope, the fibres in the delaminated areas appeared to be completely detached from the polymer matrix. Analysis was also done on chemical changes within the composite material. Their recommendations were to avoid use of vinyl ester resin based CFRP matrices in sweater environments. They also recommend to galvanic isolation of CFRP from metals in a marine environment.

The research listed above shows the disastrous effects that can occur both in the steel substrate and in the CFRP when galvanically connected to steel in aggressive environments for corrosion. By eliminating one of the four components of a galvanic cell, galvanic corrosion can be prevented. If using CFRP on steel, the anode (steel) and cathode (CFRP) will be present. Any structures with exposed beams, such as bridges or heavy machinery, will have an ionic solution present. Isolation from the ionic solution can be done by use of paint or other sealants. These sealants must be inspected regularly to ensure no damage is present, which may permit water ingress. Another method of preventing galvanic corrosion is to ensure there is no electric connection between the CFRP and steel. This can be done by use of an interstitial layer of glass fibres or other non-conductive material between the steel and first layer of CFRP repair. By isolating the FRP and steel galvanically, either by preventing electrical connection or access to ionic solution, we can prevent the damage to either component from occurring.

3 Experimental Program

3.1 Test Matrix

The original test matrix comprised thirteen experimental specimens in a parametric study of the variables: angle of repair, eccentricity of repair and ETR. The repair material used was SikaHex 103C unidirectional fabric. The fabric layers are to be bonded to the steel using Sikadur 330 as a primer and Sikadur 300 (Sika Canada Inc. 2007) as a saturant.

3.1.1 Parameters of Study

The parameters under consideration included eccentricity of repair (single sided vs. double sided); orientation of repair; and effective thickness ratio (ETR).

The tests took into account stress ranges typical of those seen in Canadian bridge girders. The nominal stress range ($\Delta\sigma_n$) was chosen as 80 MPa. This value is representative of the values seen on a typical bridge member in Alberta, based on the current bridge design criteria (Alberta Infrastructure and Transportation 2007), and the current bridge design standard CAN/CSA S6-06 (2006).

Some bridge girders may have limited access in the field. In many situations, a single sided repair may be all that is possible. The experimental design examines both single- and double-sided repairs and compares the effectiveness of the repairs.

Due to the nature of the specimens, installation can be done with greater ease along the longitudinal axis than at an angle. For this reason, three repair fibre orientations are considered. These are: longitudinal; angled at 45° to the longitudinal axis; and a multi-directional three layer repair at 0°, 45° and 90° where 0° is the longitudinal axis of the beam. Repairs are to be done using a wet-layup process for CFRP application. It is believed that the angled repair will be the most effective as it will be nearly perpendicular to the angle of the unrepaired crack.

Another aspect to be considered is the effective thickness ratio. In Equation [3-1], ETR is defined as:

$$ETR = \frac{E_{CFRP} t_{CFRP}}{E_S t_S} \quad \textbf{[3-1]}$$

where E_{CFRP} and E_S are the modulus of elasticity of the FRP repair and steel respectively, and t_{CFRP} and t_S are their respective thicknesses. The ETR is controlled by the number of layers of CFRP present. Three layers of CFRP on a single sided repair give an ETR of 0.132.

3.1.2 Specimen Nomenclature

The specimens are named in the XHZ#103C format, where X represents whether the specimen has a (S)ingle sided-, (D)ouble sided- or (N)o-repair; H represents a nominal stress range of 80 MPa at the cope location; Z represents whether the repair is at a 45° angle to the longitudinal axis (A), along the longitudinal axis (L) or a three layer orthogonal repair (O); # represents the number of layers of CFRP per side. Finally, the 103C represents the type of CFRP repair used. 103C is abbreviated from SikaHex® Wrap 103C. In the case of the unrepaired specimen, Z, # and 103C are omitted.

3.1.3 Modifications to Original Test Matrix

To do a full study of the effects of the four parameters listed below would require 1 (stress range) x 2 (eccentricities) x 2 (ETR) x 3 (patterns) = 12 repaired specimens (Table 3-1) and at least one unrepaired specimen for a total of 13 specimens.

Table 3-1 Original experimental test matrix

Specimen	*Repair Eccentricity*	*Pattern*	*Layers per side*	*ETR*	*ΔSIF*
NH	NONE	NA	NA	NA	1
SHA3103C	SS	Angle	3	0.132	0.783
SHA6103C	SS	Angle	6	0.264	0.707
SHL3103C	SS	Longitudinal	3	0.093	0.935
SHL6103C	SS	Longitudinal	6	0.187	0.917
SHO3103C	SS	Orthogonal	3	0.106	0.932
SHO6103C	SS	Orthogonal	6	0.213	0.912
DHA3103C	DS	Angle	3	0.264	0.707
DHA6103C	DS	Angle	6	0.528	0.554
DHL3103C	DS	Longitudinal	3	0.187	0.917
DHL6103C	DS	Longitudinal	6	0.374	0.880
DHO3103C	DS	Orthogonal	3	0.213	0.912
DHO6103C	DS	Orthogonal	6	0.425	0.870

In order to reduce the number of specimens and the testing time, several modifications were made to the test matrix. The number of tests was minimized by choosing a base case for the experiment, and parametrically varying the test cases from that base case. In this test program, the base test case chosen was a three layer single-sided angled repair, i.e. SHA3103C. The number of double sided tests was restricted due to difficulty in obtaining precise crack length measurements. Table 3-2 shows the revised test matrix, taking these factors into consideration. Upon completion of the fifth repaired specimen, testing facilities failed and no further specimens could be tested.

Table 3-2 Modified experimental test matrix

Specimen	*Eccentricity*	*Pattern*	*Layers per side*	*ETR*	*ΔSIF*
NH	NONE	NA	NA	NA	1
SHA3103C	SS	Angle	3	0.132	0.783
SHA6103C	SS	Angle	6	0.264	0.707
SHL3103C	SS	Longitudinal	3	0.093	0.935
SHO3103C	SS	Orthogonal	3	0.106	0.932
DHA3103C	DS	Angle	3	0.264	0.707

Figure 3-1 shows the three different repair orientations under consideration and the unrepaired control case. Yam and Cheng (1990) found that crack propagation

on an unrepaired coped beam is typically an angle (θ) to the vertical (Figure 3-1a) which varies with cope geometry, with an approximate $\theta = \pm 35°$. On a longitudinally repaired specimen (Figure 3-1b) the angle (ϕ) between the initial crack propagation and repair is not perpendicular to the crack direction, or $\phi < 90°$ (Figure 3-1b). Recognizing this concern, a focus was made on angle repaired specimens where the angle between the fibre orientation and the longitudinal axis of the member (ψ) is 45° (Figure 3-1c). The fourth type of repair, as shown in Figure 3-1d is a multi-directional three layer (ψ = 45°, 0°, 90°) repair, dubbed the orthogonal repair. The effect of the orthogonal repair on the strength, toughness and crack propagation angle are less clearly defined than that of the longitudinal repair (as defined below) or the angled repair due to the multiple possible stress paths of this repair.

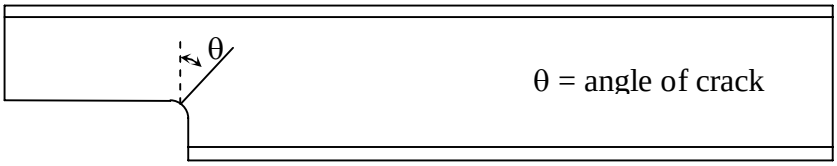

a) Unrepaired cracked specimen.

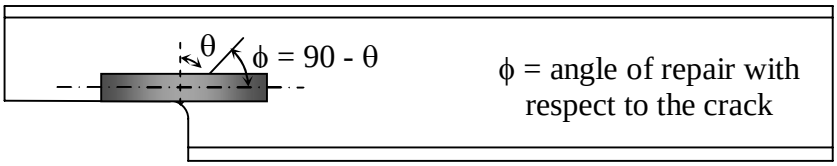

b) Longitudinally repaired specimen.

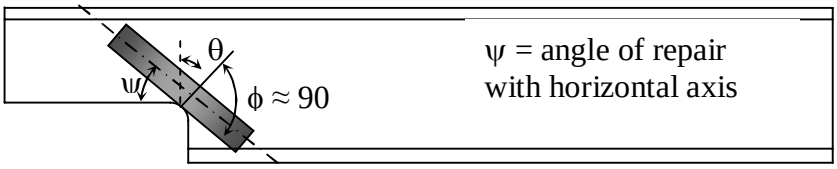

c) Angle repaired specimen

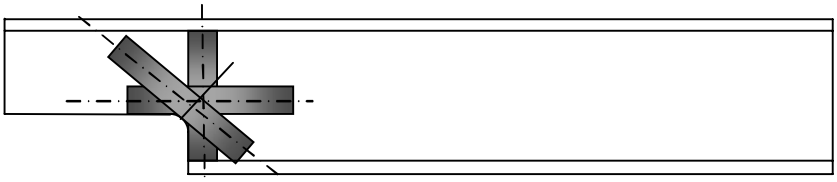

d) Orthogonally repaired specimen

Figure 3-1 Orientation of CFRP repairs

Crack propagation along the fibre direction is a concern for all of the longitudinally repaired specimens. CFRP is an anisotropic material with high strength in the fibre direction and comparatively negligible strength perpendicular the fibre direction. Since ϕ is less than 90°, the CFRP repair is acting at an angle to the principal tension field. The CFRP patch can take a portion of the stresses in the fibre direction. However, due to the anisotropic nature of the patch, the shared portions of the shear stresses and stresses perpendicular to the fibre direction are comparatively much smaller. This has the potential to shift principal tension field in the repaired steel towards the fibre direction, rendering the patch less effective.

Another concern in the testing is how to obtain crack length data. On single sided repairs, the crack length is clearly visible from the unrepaired side, and its length can be measured visually using a ruler or callipers. On double sided repairs, however, crack length measurement is a greater challenge. Different options available are crack propagation electronic gauges, demec gauges, strain gauges and image correlation.

Crack propagation gauges are electronic circuits which can be bonded directly to the steel in the anticipated path of the fatigue crack. The circuits consist of several thin metallic wires on a thin flexible backing. They work by recording the resistance across the series of wires. As the crack tip passes a wire, the wire will break, thus drastically changing the voltage output. These gauges, however, raise concerns regarding debonding and uncertainty in crack direction. The gauge must be bonded directly to the steel, between the steel and the CFRP repair. Any debonding of the gauge can initiate progressive debonding of the CFRP from the steel. Also, the wires which carry the signal for the propagation gauge must run either beneath the CFRP patch, creating imperfections in the steel-CFRP bond; or be pulled through the CFRP fabric during installation, making proper installation difficult. In addition to this, the crack direction is estimated. Should the interaction of the FRP repair with the steel change the direction of the crack, the

crack tip may extend out the side of the gauge, rendering any readings after that point ineffectual.

Another possible method to determine the crack length is to use a hand held demec gauge, where the demec points are epoxied to the outside of the repair. If the strain shows a significant increase between two demec points from the last data set, then the crack has passed the line between the two demec points. This is an imperfect method because it cannot detect the actual crack length, but rather that the crack tip is situated between two demec points. It also cannot tell at which cycle this happens, as the test must be stopped in order to take the readings. An image correlation program can approximate this method using images of the beam taken at regular intervals. The test must also be stopped for these readings, and the overall results are more variable. As the distance from the specimen edge can be selected in post-processing. In either case, it is impossible to know at what cycle count the crack tip passes a specific milestone.

To obtain more precise results, a focus was made on single sided repairs. Most of the double sided repaired specimens were eliminated in the revised testing program.

3.1.4 Parametric Testing

Table 3-3 shows the parametric sets for the tests. Enough specimens were selected to give at least two sets of data for each parameter, plus the unrepaired specimen.

Table 3-3 Parametric test matrix

Specimen	*Eccentricity*	*Pattern*	*ETR*
NH			
SHA3103C	X	X	X
SHA6103C			X
SHL3103C		X	
SHO3103C		X	
DHA3103C	X		

3.2 Specimen Description

Six beams, standard section W410 x 54 were used for the experiment. The beams were each 16 feet or 4877 mm long, and coped at each end (see Figure 3-2). Figure 3-3 shows the cope and end connection details for the beams. The copes are 280 mm long by 60 mm deep and have a radius of 15 mm. Three holes of 24 mm diameter were drilled at 50 mm, 75 mm, 75 mm spacing to support 7/8 inch (22 mm) bolts. The test span length is 3670 mm with one support bolted to the web in the coped section, and the other support under the bottom flange.

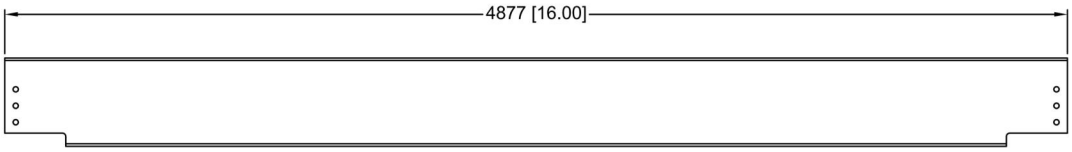

Figure 3-2 Test specimens, W410x54, 300W, gross view

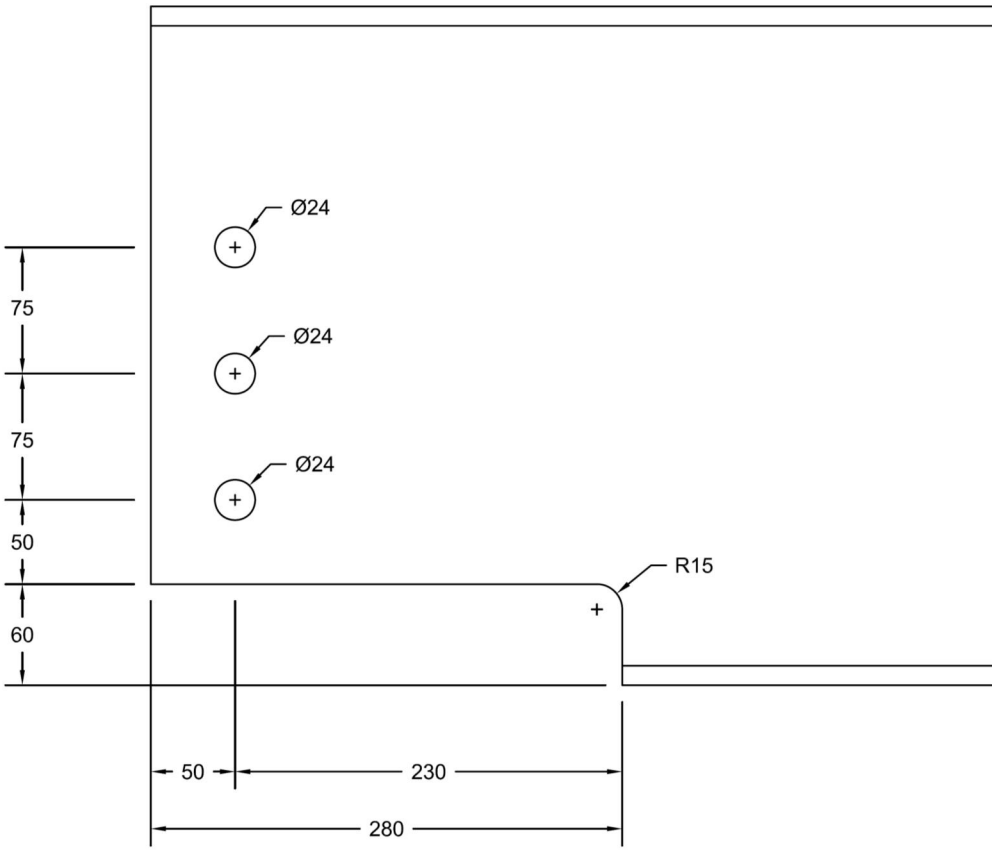

Figure 3-3 Test specimen end detail

The copes were prepared by computer assisted flame cut to an accuracy of ± 1 mm. The flame cut surface was then ground smooth to reduce variability in surface conditions from one test to the next. To introduce a flaw at which to induce fatigue crack initiation, all specimens were notched to approximately 0.5 mm with a sharp 60° Swiss file. The notches were located 7 mm from the cope line and angled perpendicular to the cope radius. The depth of the notch was measured such that inserting the tip of the file in the notch would give a flush profile.

3.2.1 Material Properties

A total of seven steel coupons were tested to determine the material properties of the steel beams. Three coupons were cut from the web and four from the flanges of a section of W410 x 54 beam. The coupons were cut and tested in accordance with ASTM A370-02(2002). All W410 x 54 sections tested were produced in the same heat as the section from which the coupons were cut. All coupons were cut parallel to the longitudinal axis of the beam. The coupon dimensions were 40 mm wide with a 50 mm gauge length. The thickness of the coupons was 11.1 mm for the flanges and 7.0 mm for the coupons cut from the web of the beam. The average material properties are reported below. The web coupons had an average elastic modulus of 209,600 MPa, static yield strength of 384.6 MPa and ultimate strength of 476.7 MPa. The flange coupons had an average elastic modulus of 204,700 MPa, static yield strength of 351.5 MPa and ultimate strength of 470.9 MPa.

A total of four CFRP coupons were tested. The coupons were prepared in accordance with ASTM D3039/D3039M-00(2006). Two three layer CFRP coupons and two six layer coupons were prepared with the dimensions 50 mm x 500 mm and the fibres running longitudinally. The thickness of the coupons was governed by the number of layers of CFRP. The average material properties of the coupons are reported below. The tensile behaviour of the FRP patches is linear elastic, so no yield strength is reported. The three layer CFRP coupons had an average elastic modulus of 70,100 MPa and an ultimate strength of 687.8 MPa.

The six layer coupons had an average elastic modulus and ultimate strength of 71,800 MPa and 636.1 MPa, respectively.

3.3 Instrumentation

3.3.1 Single Sided Repairs

For the most part, the single sided repaired specimens held the same instrumentation scheme. Figure 3-4 shows the instrumentation applied to the unrepaired side of the specimen. Five strain gauges were used, oriented such that the strain value detected is along the longitudinal axis of the beam. These strain gauges are 5 mm gauge length, 120 Ohm resistors. They are located at 80 mm, 230 mm, 280 mm and 310 mm from the top of the top flange. At the cope location, however, a rosette is applied to detect the orientation of principal stresses. This was located as close to the cope as possible, without allowing the machining at the radius to interfere with the placement. In most cases the actual location was at least 2 mm above the actual cope.

Application of the gauges was done using the M-bond 200 system. Prior to gauge installation, the surface of the steel was degreased, then ground smooth using a sandpaper wheel until the steel reached a mirror hue. This was done without removal of too much base material. Once the mirror hue was reached, the gauge placement lines were applied using a metal scribe tool. Sandpaper was then used to roughen the surface for bonding, and remove any roughness or burrs incurred by the scribing process. Any residues were then removed using the conditioner and neutralizer system recommended by the manufacturer, and the gauges were applied.

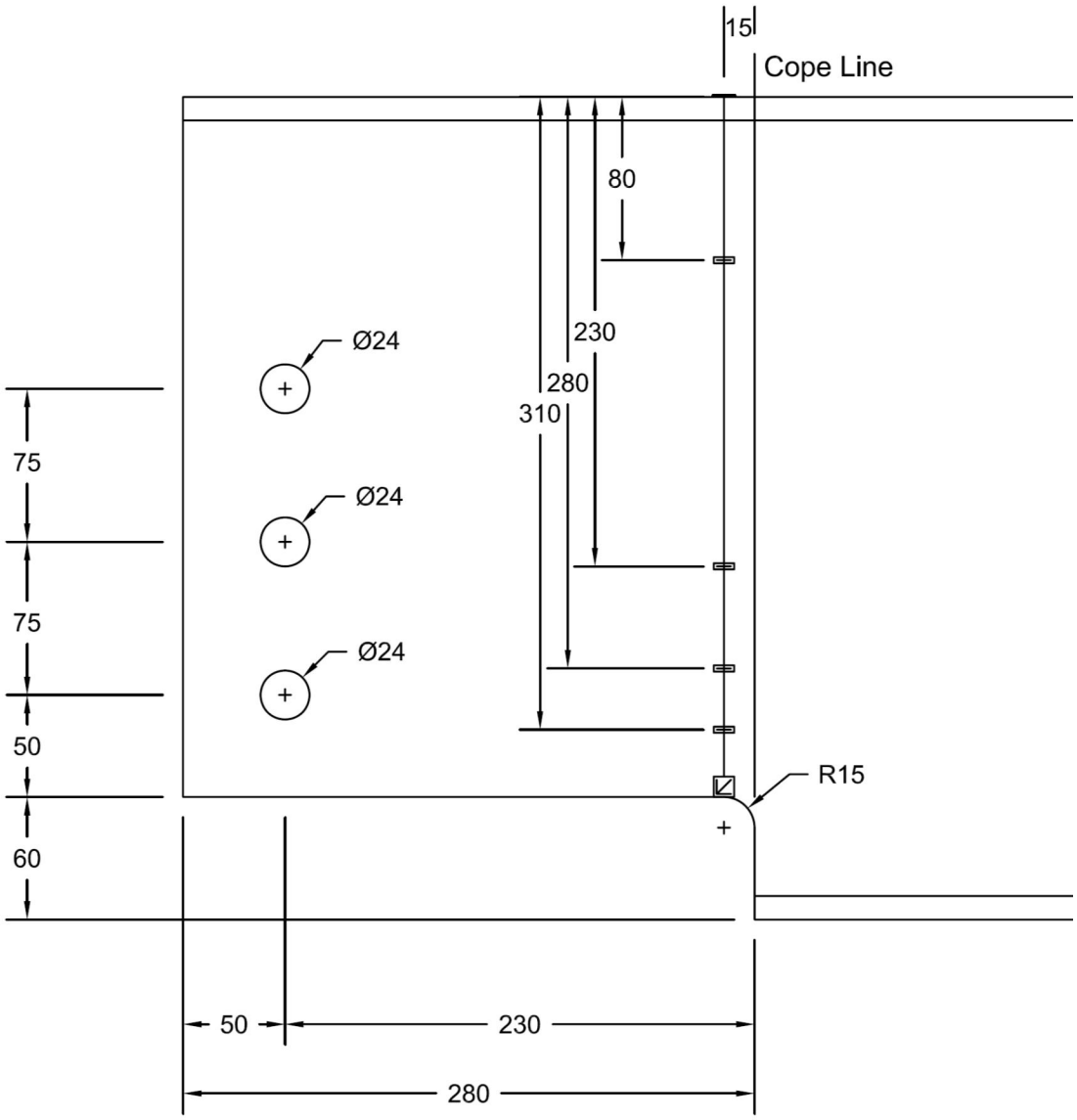

Figure 3-4 Single sided instrumentation at the cope line

3.3.2 Double Sided Repairs

The instrumentation for data collection on the double sided repairs consisted of strain gauges applied directly to the CFRP patch. Figure 3-5 shows a schematic of the strain gauges applied to the CFRP patch. The gauges are oriented in the fibre direction, and centred on a line 45° from the horizontal, originating at the initial notch location.

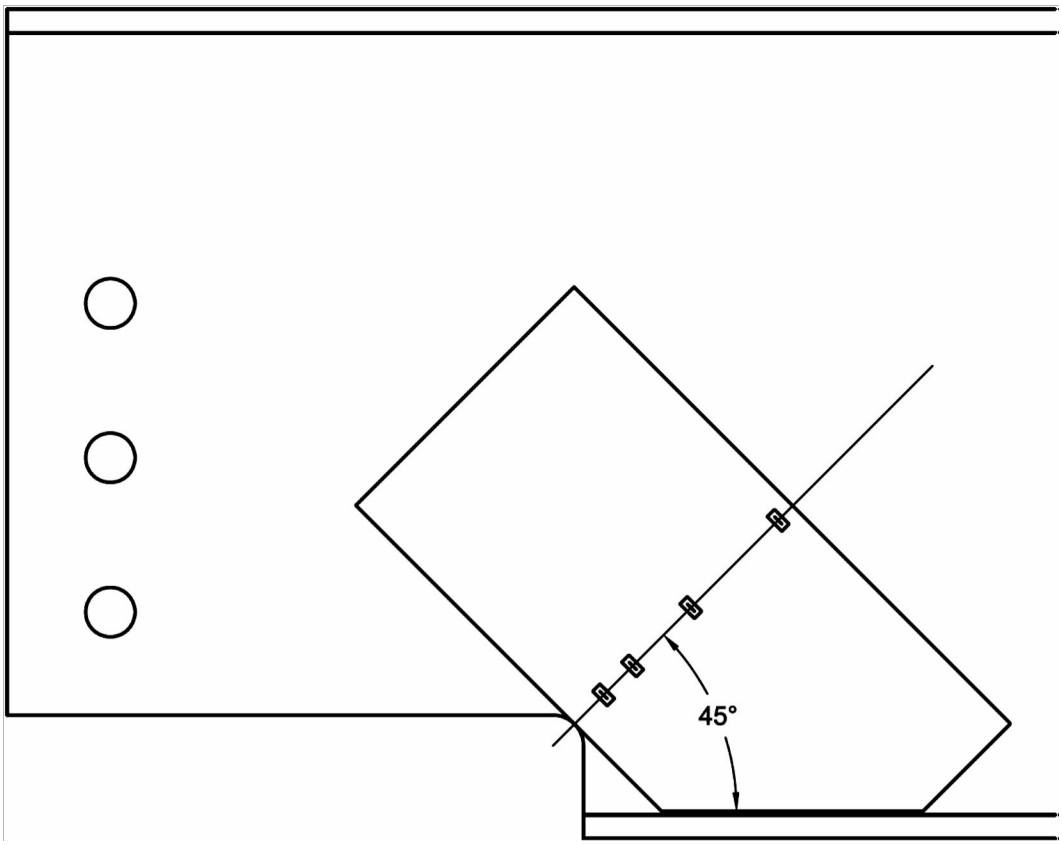

Figure 3-5 Schematic of CFRP mounted gauge placement

The crack length was then detected by finding the number of cycles at which the strain gauges showed a marked change in strain amplitude slope under cyclic loading. If the crack were to pass directly beneath the gauge location, then the strain amplitude slope ($d\varepsilon/dN$) would increase drastically as the crack would now also reflect crack opening strain. Conversely, if the crack were to pass alongside the strain gauge location, the gauge would show decrease in strain amplitude slope.

Figure 3-6 shows a schematic of this calibration method. The distance of gauge from the cope is plotted against the actual crack length at the point where a significant change in strain amplitude slope is observed. The data is then fit with a least squares trend line. The formula for the trendline will act as a calibration factor for the determining the crack length using the same method for the double sided repairs.

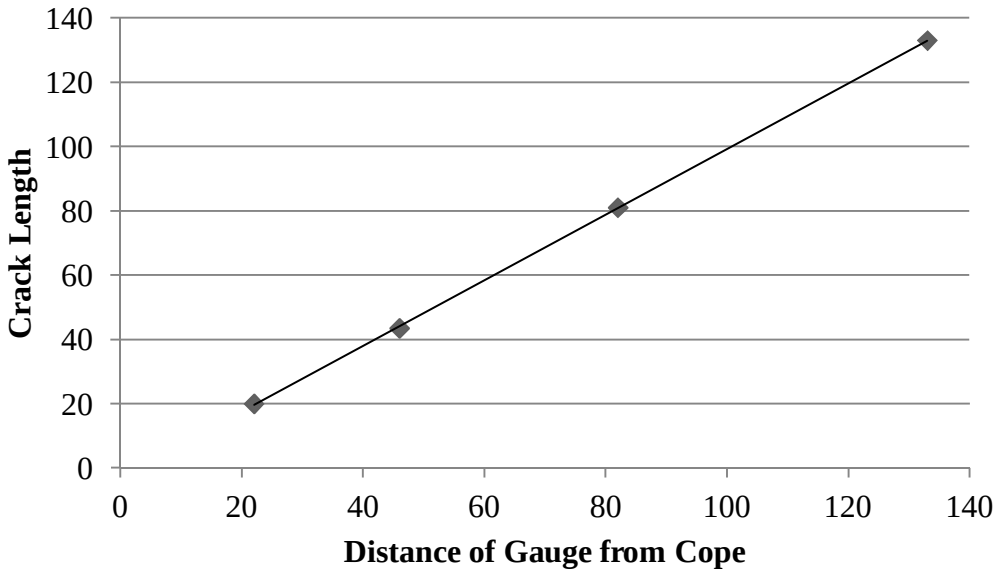

Figure 3-6 Schematic of correlation between change in slope of strain amplitude and observed crack length

In order to install the strain gauges, the surface was prepped to a smooth flat surface by sanding. 220 grit sandpaper was used for this process. After sanding, the centreline of the gauges was applied using a scribe tool or a fine tipped ballpoint pen. The scribing was not easily visible in the fibre direction. In many cases the fibre direction was used for longitudinal alignment of the gauge. After scribing, all residues were removed using Acetone. The acetone was applied using cotton tipped swabs until no discoloration was observed on the swabs. The gauges were then applied using the M-Bond 200 system, including the surface conditioner, neutralizer, catalyst and M-Bond glue.

Due to the nature of the CFRP patch, it is not always possible to place the gauges at the prescribed distance from the cope, and they must be relocated. Figure 3-7 illustrates some of the gauge placement challenges. The CFRP used for the repairs is a woven fabric, giving three types of possible gauge placement locations. These are Top, Bottom and Interface.

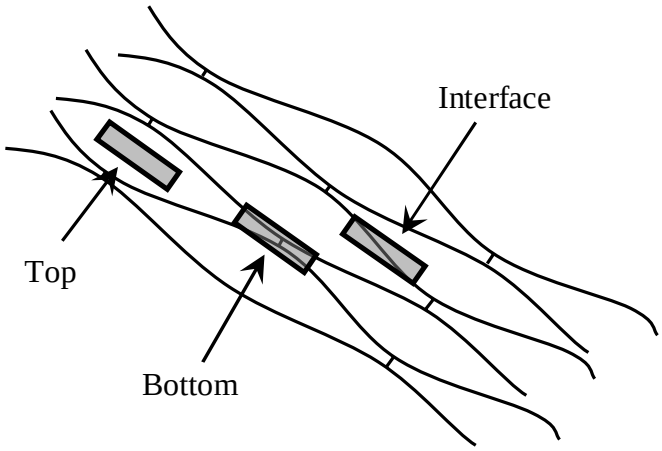

Figure 3-7 Gauge placement location types

The ideal location for gauge placement is the Top location. At this location, gauges are being installed on the same bundle of fibres, thus there is little shear between fibres. Sanding to a smooth flat surface is easy and requires very little removal of FRP. Top locations were mostly used.

Another possible location for strain gauge application was at the Interface between two fibre strands. Applicaton of strain gauges at this location required more work for sanding to a smooth flat surface. It was necessary to remove more CFRP than at the Top location. In addition, since this is an interface between two fibre strands, there is a high probability of a shear plane between strands intersecting the gauge. Few gauges were placed at interface locations. At the interface locations, the electronic circuit portion of the gauge was kept on a single fibre strand whenever possible. This required a minor relocation of 0.5-2 mm from the prescribed distance.

The Bottom location was not at all viable for gauge placement as it was necessary to remove the entire depth of the neighbouring strands before a smooth flat surface was possible. When the gauge placement prescribed fell upon a Bottom location, the gauge was relocated to a more viable location. The most severe example of this was the gauge with the prescribed distance of 140 mm from the cope on specimen SHA3103C which was relocated by7 mm.

3.3.3 Statics Check Gauges

Four more strain gauges were used for statics check. They were applied using the same method for the single sided repair gauges. These statics check gauges were monitored under cyclic loading to ensure the load amplitude remained constant. The gauges were located at two cross sections. The first cross-section was located 720 mm past the cope location and 885 mm from the centre of the load point. The second was located 885 mm past the centre of the load point, or 2770 mm from the end of the beam. At both cross sections, the location was sufficiently removed from the support, cope and load point to render local effects from those features negligible. The location of the cross sections was chosen such that for every 40 kN of load applied at the load point, the strain gauges report 100 $\mu\varepsilon$ change in strain.

3.4 Test Description

3.4.1 Test Set-up

Figure 3-8 shows the test set-up. The beams were tested in three-point loading with a span length of 3670 mm. The load point was centred between the two supports. The beam was supported by double angle brackets bolted to the web of the coped section and under the flange at the far end such that only one cope radius is experiencing cyclic loading during each test. The use of a much shorter span length and a double cope allows each specimen to be used for two tests. Only one cope radius experiences loading during a test.

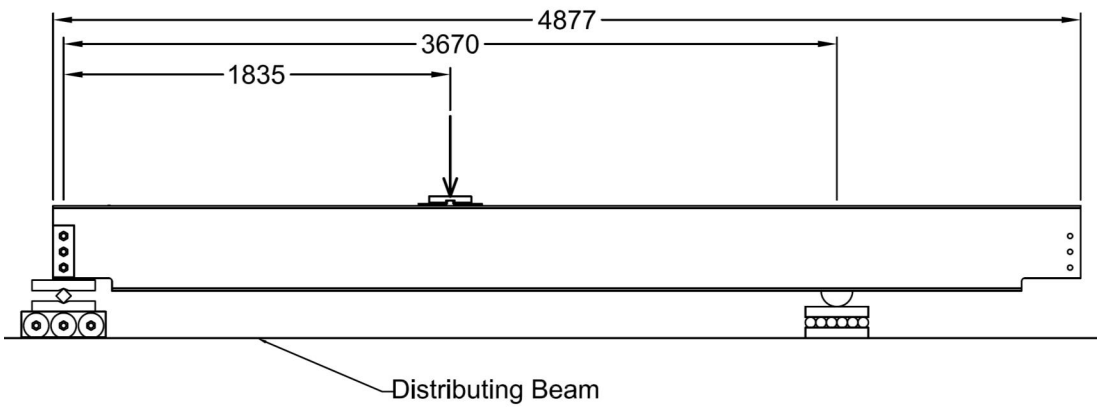

Figure 3-8 Experimental Test Setup

3.4.2 Static Testing

Prior to generation of any pre-crack, all beams were loaded statically from 0 kN to 200 kN. This was done by manually changing the load on the beam and holding it at that load until all strain readings had stabilized. Readings were taken from all steel mounted strain gauges at various load intervals and compared. The statics check strain gauge readings are of particular interest, as the readings from the statics check were used to control the loading during cyclic loading. The steel strain readings give a good indication of the actual stress gradient in the coped beam.

3.4.3 Generation of Pre-crack

The beams were loaded cyclically between an applied load at midspan of 40 kN and 200 kN. Testing was done at 4 Hz. The loading amplitude was maintained by monitoring the amplitudes of the statics check strain gauges (section 3.3.3). If the statics gauges showed a change in amplitude the load levels were adjusted accordingly to maintain constant loading amplitude.

Pre-crack length was measured visually by use of a ruled edge with one end attached to the beam at the cope radius. Whitewash consisting of one part plaster of paris to two parts lime was used to facilitate crack tip detection. When the crack reached 10 mm, the test was stopped and the repair was applied.

3.4.4 Application of Repair

The repair applied consisted of SikaWrap® Hex 103C. The patches were 300 mm long by 150 mm wide, with the fibres running in the long direction. All patches were laid using a wet layup procedure.

The fibres were cut to the correct dimensions using a straight edge and sharp blade. Scissors were found to fray the cut edges where a sharp blade left a crisp edge to the dry fibres. Once cut, the fibres were set aside for surface preparation on the steel to occur.

For ease of installation, the beams were laid on their sides such that the web provided a horizontal surface on which to apply the patch. Surface preparation for the steel consisted of degreasing, then sandblasting to a white metal finish.

a) b)

Figure 3-9 Beams prepared to white metal surface condition a) SHO3103C b) SHL3103C

Figure 3-9 shows beams SHO3103C and SHL3103C prepared to white metal finish. A white metal finish is such that there are no residues on the steel, and due to the roughness of the metal, the surface appears is no longer shiny, but appears to be white and dull. This was done with a portable sandblaster connected to a compressed air source. Once the metal surface was sufficiently roughened, any excess sand and particulate was removed from the surface using a wet/dry vac. It is very important that the patch be applied to the steel as soon after the metal surface preparation as possible, because the steel oxidizes when left exposed. A

thin layer of oxide may be enough to damage the bond between the CFRP patch and the steel.

As soon as surface preparation on the steel surface was completed, the Primer, Sikadur® 330 was mixed with an A:B ratio of 4:1 by weight. The primer mixed then was immediately applied to the steel in a thin layer (Figure 3-10). This epoxy is a thick creamy texture coming once mixed. A disposable sponge tipped paintbrush was used to apply it directly to the prepared steel. The primer was applied evenly to the steel surface until the surface was completely covered, and the opalescent hue was nearly gone.

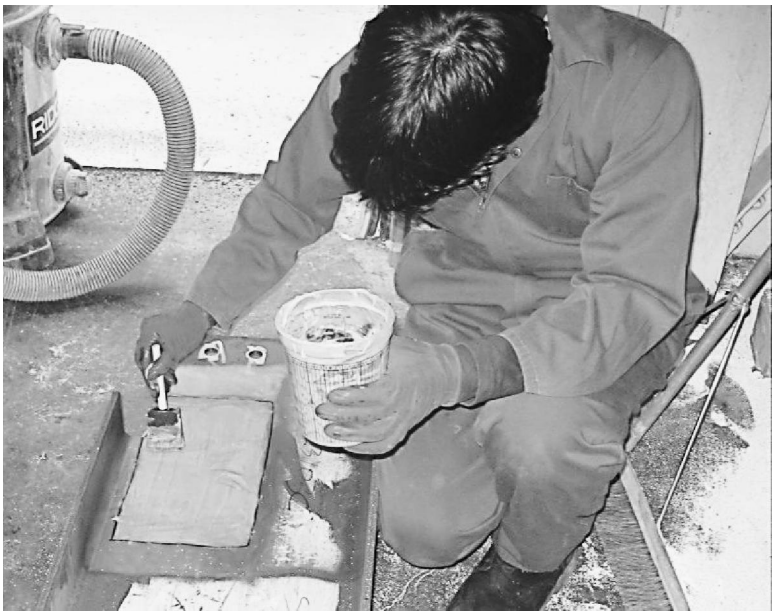

Figure 3-10 Application of Sikadur® 330 primer to SHL3103C

The fabric saturant, Sikadur® 300, was mixed with a component ratio A:B of 2.9:1 by weight. The saturant was applied to the fabric on a worktable coated with polyurethane. Figure 3-11 shows the polyurethane protected work surface. Also shown in the figure are the paint rollers and prepared saturant epoxy. The purpose of the polyurethane layer was to prevent any epoxy from becoming permanently affixed itself to the work surface. A bead of saturant the length of the patch was poured directly onto the protected work surface and spread into a thin layer using a paint roller. The dry fabric was placed directly onto the treated

work surface. A bead of saturant was then applied to the upper surface of the FRP layer and worked into the fibres using a paint layer. The fabric was ready to place on the beam once rolling firmly with the paint roller would cause excess saturant to ooze from the fibre ends.

Figure 3-11 Polyurethane protected work surface.

Figure 3-12 shows the patch application process. The saturated fabric was then placed on the primed steel. The process is wet-on-wet; therefore, the saturated (wet) fabric was placed directly on the uncured (wet) primer. Once placed, a paint roller was used to smooth out any air bubbles, remove excess saturant and ensure full contact between the steel and the fabric. Each subsequent layer of fabric was saturated and applied immediately wet-on-wet to the previous layer. No inter layer epoxies or primers were used. Once the patch was applied, it was allowed to cure for a minimum of twenty-four hours prior to moving the beam.

Figure 3-12 Application of FRP patch to steel beam

For the double-sided repair, DHA3103C, the patch on the first side was allowed to cure for 24 hours prior to moving the beam. Once cured, the beam was flipped and the entire procedure repeated on the opposite side. At some point the patch on the east side of the beam was handled prior to its cure. This caused a deformity in the patch.

3.4.4.1 Angled Repairs

Figure 3-13 shows the detail for the angled patches. Each layer of the applied patch was 150 mm wide by 300 mm long in the fibre direction. For the angled patches, the patch was applied at a 45° angle to the longitudinal axis, with the fibres on the long edge of the patch running tangent to the cope. The patch was centred around the pre-crack in length, however due to the geometry of the specimen, the patch was required to be trimmed at a 45° angle at the bottom edge to accommodate the flange.

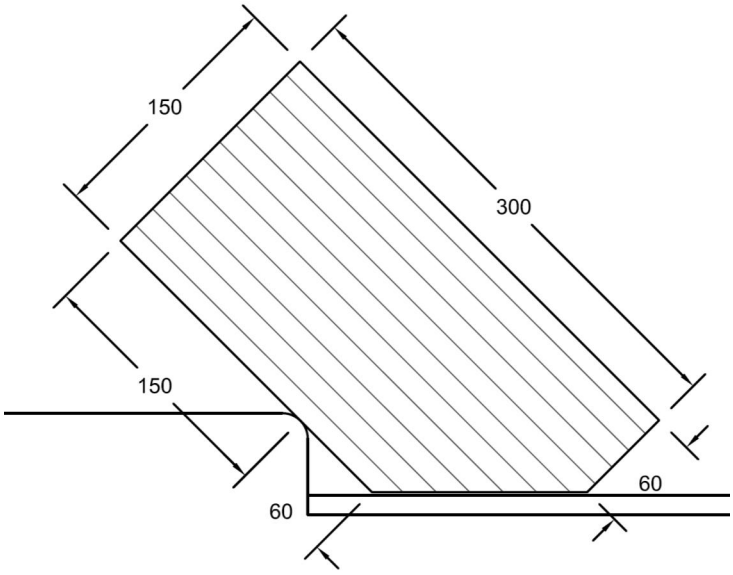

Figure 3-13 Angled repair detail

3.4.4.2 Longitudinal Repairs

Figure 3-14 shows the detail for the longitudinal repair. The patch applied was 150 mm wide by 300 mm long in the fibre direction. The patch was applied such that the end of the patch was located only 100 mm from the cope line towards the support. This offset was chosen due to the crack angle. The angle was predicted to angle away from the cope at a minimum of 35° from the vertical. Thus, as the crack grew, it would encounter more even development length on either side in the patch.

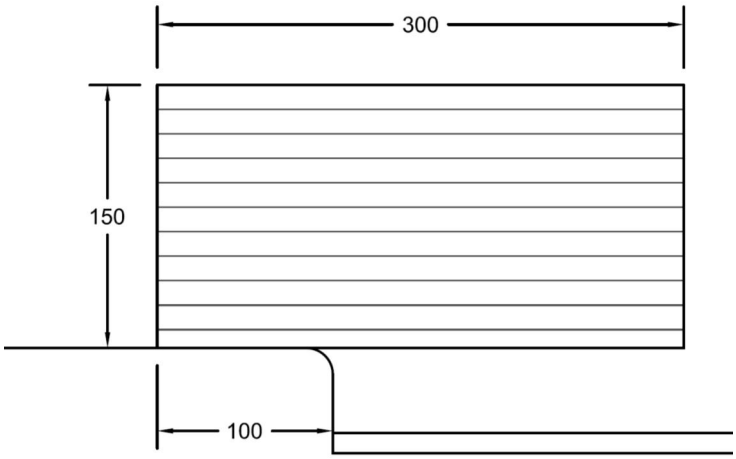

Figure 3-14 Longitudinal repair detail

3.4.4.3 Multidirectional Repairs

Figure 3-15 shows the detail for the multidirectional repair. The first layer was laid as an angled repair similar to that shown in section 3.4.4.1. Over this, the second layer was laid along the longitudinal axis of the beam. Again, the positioning of the patch is as shown in section 3.4.4.2. The third layer of repair was a transverse patch. This was laid with the fibres in the transverse direction of the beam. The layer was 300 mm long by 150 mm wide.

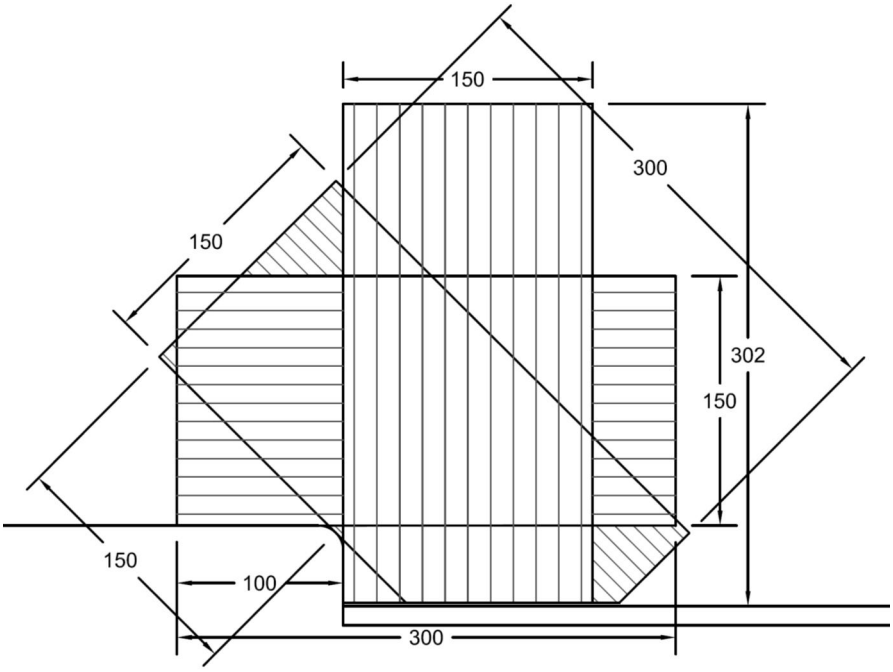

Figure 3-15 Multi-directional repair detail

Because the patches did not stack perfectly, the primer had to be applied under the entire area which a layer of FRP would be attached to the steel. This was done by placing the dry patches on the cleaned and prepared steel surface and tracing with a permanent marker approximately 10 mm around the outside edges of the patch. The primer was then applied within the traced outline. Figure 3-16 shows the finished repair on specimen SHO3103C. The drawn outline and primer are visible in the photo.

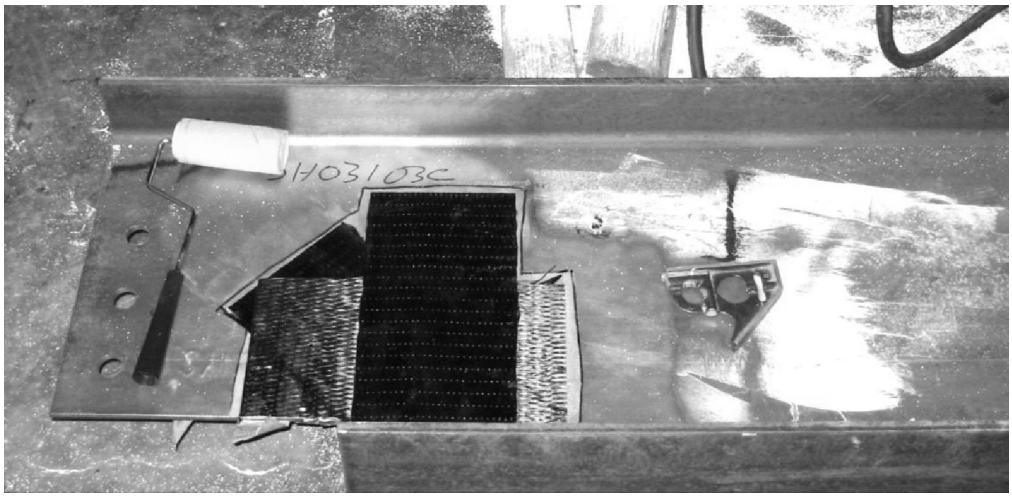

Figure 3-16 Finished repair on specimen SHO3103C

3.4.5 Cyclic Testing

The beams were loaded cyclically between an applied load at midspan of 40 kN and 200 kN. Testing was done at 4 Hz. The loading amplitude was maintained by monitoring the amplitudes of the statics check strain gauges (section 3.3.3). If the statics gauges showed a change in amplitude the load levels were adjusted accordingly to maintain constant loading amplitude. As the crack grew, the deflection also increased. To maintain loading levels once deflection increased significantly, the frequency of loading was dropped in increments of 0.05 Hz or 0.10 Hz until loading stabilized.

The load was then monitored again. During this process, strain amplitude readings were taken at intervals from all the strain gauges. Any major changes in strain amplitude were noted. Crack length was monitored visually for the single-sided repairs using a ruled edge and whitewash to emphasize the location of the crack tip. For DHA3-103C, crack length was monitored using strain gauges on the FRP as discussed in section 3.3.2.

4 Results and Discussion

4.1 Results

This section contains the experimental results of the test program described in chapter 3.

4.1.1 Static Testing

All specimens were statically loaded prior to cyclic testing to verify the stress gradient via the longitudinal strain gauges mounted on the cope line. Figure 4-1 shows the longitudinal stress in the steel beam versus the distance from the cope at the gauge location. All locations have very good agreement on the stress gradient.

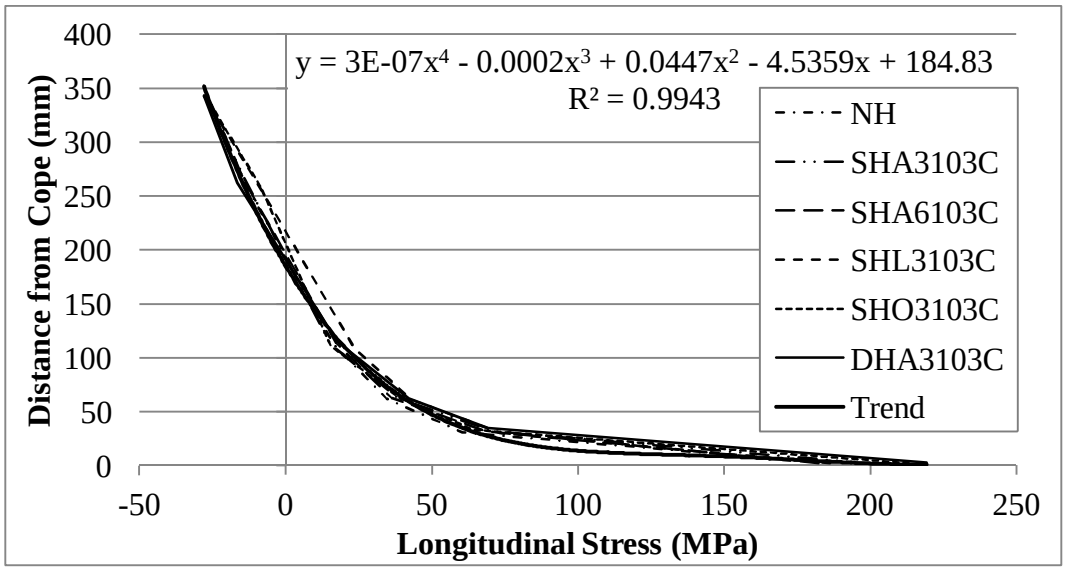

Figure 4-1 Comparison of longitudinal strain distribution for all specimens prior to pre-cracking

Table 4-1 shows the measured distance from the cope of each strain gauge. Variance in distance can be explained by errors in measurement and out of straight of the beam ends. As all strain locations were to be located from the top flange, the measurement technique for placement involved a tape measure and a square. Any out of straightness would therefore vary the resulting distance.

Table 4-1 Measured distance of longitudinal strain gauges from cope

Specimen	*Measured Distance from Cope (mm)*					
	R0	*310*	*280*	*230*	*80*	*0T*
NH	2	31	62	112	261	343
SHA3103C	2	32	63	112	265	343
SHA6103C	2	32	63	113	263	343
SHL3103C	4	30	61	108	258	343
SHO3103C	2	33	62	111	259	343
DHA3103C	3	35	62	115	262	343

Table 4-2 shows the stress taken from the strain gauges. The loading points for the stress are 40 kN and 200 kN, to represent the maximum and minimum load levels for the cyclic testing. The strain was converted to stress by multiplying the difference in strain from the two load levels by the modulus of elasticity for the beams (E_s = 209,600 MPa). For most gauge locations, the standard deviation of the stress was less than 4.6 MPa. The exception to this was the rosette gauge, which had a standard deviation across beams of 16.9 MPa. This is still less than ten percent of the average stress at that gauge location of 196.2 MPa. Possible reasons for variation in stress values are out of straightness of the rosette gauge, and local effects due to roughness of the cope section.

Table 4-2 Comparison of stresses at each gauge location for all specimens

Specimen	*Longitudinal Stress (MPa)*					
	R0	*310*	*280*	*230*	*80*	*0T*
NH	186.1	60.5	34.4	16.6	-13.8	-26.6
SHA3103C	198.1	70.4	38.3	15.3	-14.0	-27.7
SHA6103C	182.2	68.3	36.1	17.4	-14.0	-26.8
SHL3103C	178.4	73.4	43.2	23.6	-9.0	-28.0
SHO3103C	213.2	64.2	39.2	15.4	-8.7	-27.6
DHA3103C	219.2	69.0	42.0	17.6	-16.7	-28.1
Average	196.2	67.6	38.8	17.6	-12.7	-27.5
Standard Deviation	16.9	4.6	3.4	3.1	3.2	0.6

4.1.2 Cyclic Testing

Figure 4-2 shows the crack growth for the beams, normalized at the pre-crack length. The data has been normalized at 10 mm crack length. This represents the remaining fatigue life (N_R) of the specimens after the pre-cracked specimen has been repaired.

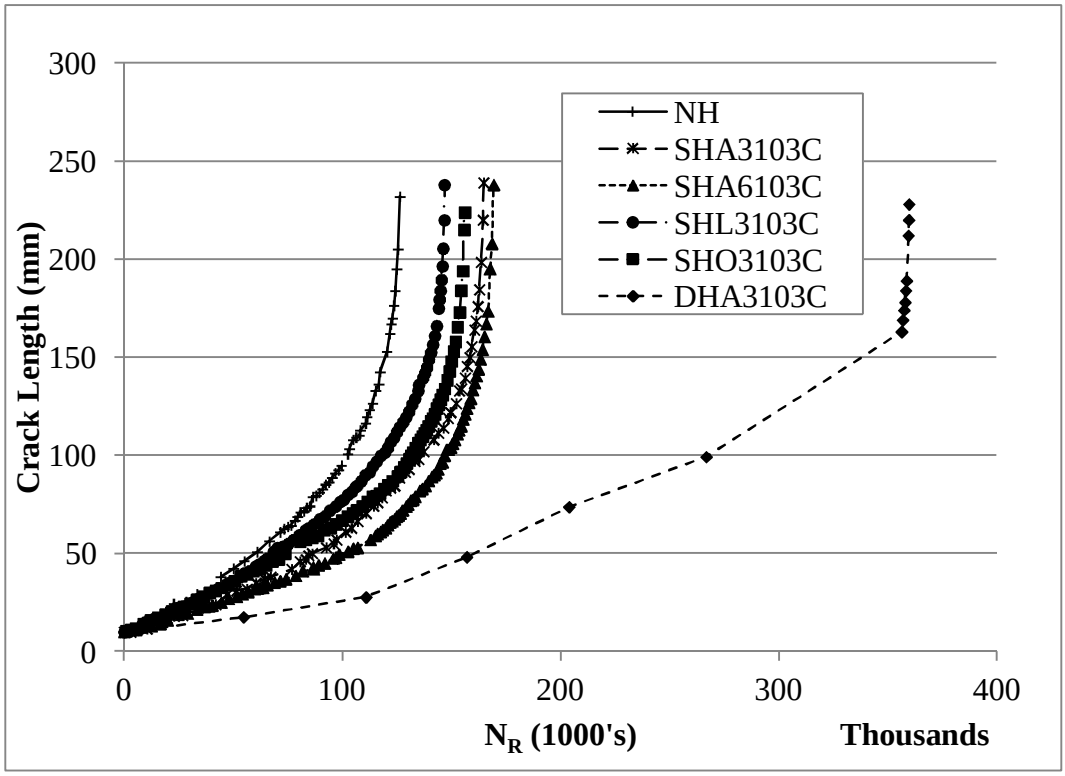

Figure 4-2 Crack propagation for all specimens versus remaining fatigue life after repairs have been applied

4.1.2.1 NH

NH was notched approximately 0.5 mm using a Swiss file with a sharp 60° edge prior to cyclic loading. The crack was first observed at 25,300 cycles, and grew to a 10 mm by 42,750 cycles. The test was continued and the specimen failed at 169,000 cycles and 232 mm crack length showing a remaining fatigue life of 126,250 cycles from the 10 mm pre-crack.

4.1.2.2 SHA3103C

SHA3103C was pre-cracked under cyclic loading at 4 Hz. The crack was first observed at 20,500 cycles. The 10 mm pre-crack length was reached after 40,127 cycles. At this point the CFRP repair was applied and allowed to cure for seven days. The cycle count was reset to zero and recorded along with the crack length. The beam failed at a remaining fatigue life (N_R) of 164,690 cycles and 239 mm. The total fatigue life of the beam was 204,817 cycles including the pre-crack.

Once cured, strain gauges were applied to the CFRP patch. Figure 4-3 shows the gauge placement with nominal distances from the cope. These strain gauges were monitored under cyclic loading to find changes in the slope of the strain amplitude. These changes would indicate the point at which the crack tip crossed the gauge location. Since the nature of the CFRP fabric can prohibit placement of a gauge at a prescribed point, the gauges were placed at the nearest potential mounting location to the prescribed distance. The gauges remained centred on the 45° diagonal and mounted in the fibre direction.

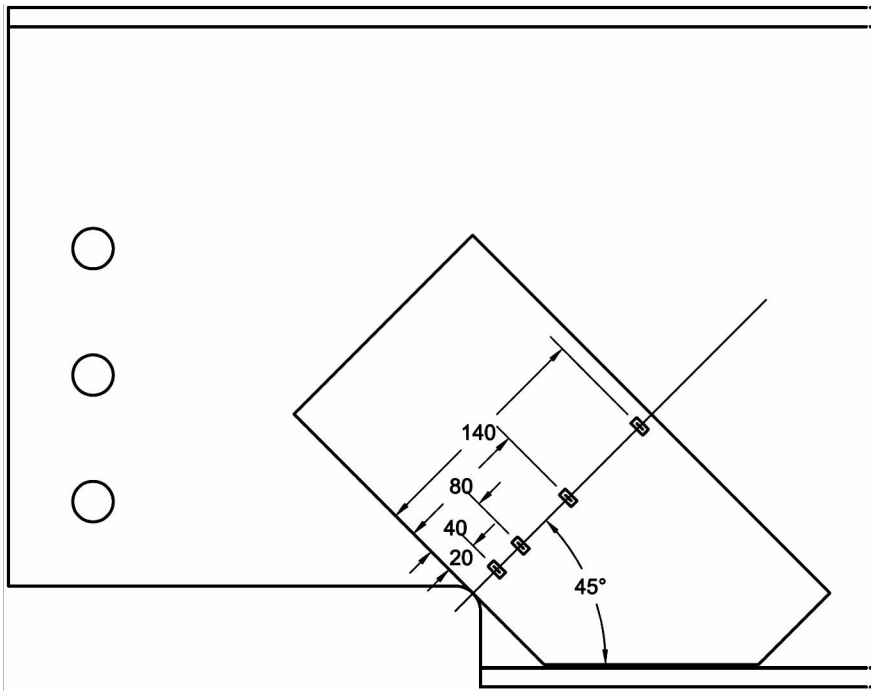

Figure 4-3 CFRP mounted strain gauge placement for SHA3103C

Figure 4-4 shows the strain amplitudes recorded for the CFRP mounted strain gauges during the test. The number of cycles at which the strain gauge showed a significant change in slope was recorded. The maximum value of strain amplitude for gauge 140 (140 mm from the edge of the repair as shown in Figure 4-3) was used in this case as this was the last point of usable data prior to the patch debonding completely from the beam.

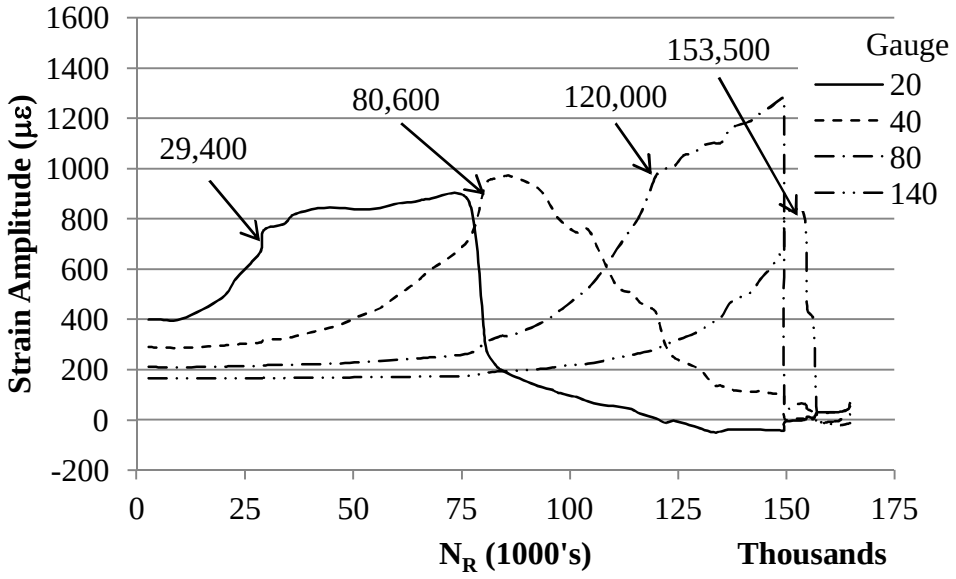

Figure 4-4 Strain amplitudes for CFRP mounted strain gauges on specimen SHA3103C

Table 4-3 summarizes the results of the strain amplitude study. The number of cycles at which the significant change in slope occurs, the crack length at this point, and the actual distance of the gauge from the cope are reported. The crack length was then plotted against the distance from cope in Figure 4-5 and the data fit with a linear trend line. The relationship proved to be linear with an R^2 value of 0.9999. The resulting linear relationship is:

$$L_{cr} = 0.9792\ D_g + 2.8196 \qquad \textbf{[4-1]}$$

where L_{cr} represents the crack length and D_g represents the distance of the gauge from the cope. The relationship was then used to calibrate the use of strain gauges mounted to the CFRP as a means of crack length detection for specimen DHA3103C.

Table 4-3 CFRP strain gauge calibration data SHA3103C

Gauge	N_R	*Distance from Cope (mm)*	*Measured Crack Length (mm)*
20	29400	20	22
40	80600	43.5	46
80	120000	81	82
140	153500	133	133

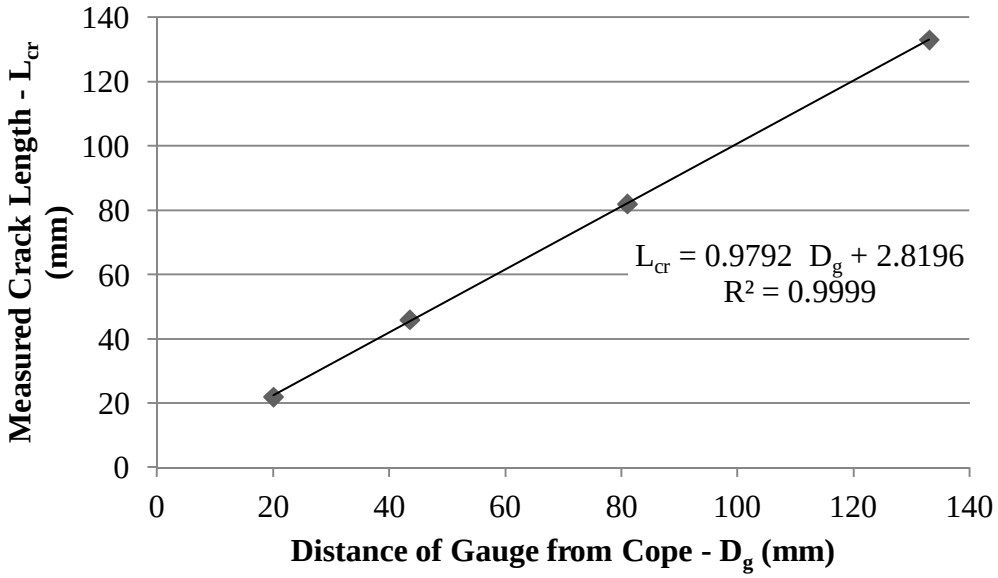

Figure 4-5 Correlation between the location of the CFRP mounted gauges and the crack length at which the gauges show a marked change in strain amplitude for SHA3103C

4.1.2.3 SHA6103C

SHA6103C was pre-cracked under cyclic loading. The crack was first observed at 17,200 cycles. The 10 mm pre-crack length was reached after 51,401 cycles. At this point the CFRP repair was applied and allowed to cure for seven days.

The cycle count was reset to zero and recorded along with the crack length. The beam failed at a remaining fatigue life (N_R) of 169,289 cycles and 238 mm. The total fatigue life of the beam was 220,690 cycles including the pre-crack.

4.1.2.4 SHL3103C

SHL3103C was pre-cracked under cyclic loading. The crack was first observed at 27,000 cycles at 3 mm crack length. The 10 mm pre-crack length was reached after 43,920 cycles. At this point the CFRP repair was applied and allowed to cure for seven days. The cycle count was reset to zero and recorded along with the crack length. The beam failed at a remaining fatigue life (N_R) of 146,693 cycles and 238 mm. The total fatigue life of the beam was 190,613 cycles including the pre-crack.

4.1.2.5 SHO3103C

SHO3103C was pre-cracked to 10 mm under cyclic loading. The crack was first observed at 17,380 cycles at 3 mm crack length. The 10 mm pre-crack length was reached after 40,148 cycles. At this point the CFRP repair was applied and allowed to cure for seven days. The cycle count was reset to zero and recorded along with the crack length. The beam failed at a remaining fatigue life (N_R) of 156,394 cycles and 224 mm. The total fatigue life of the beam was 196,542 cycles including the pre-crack.

4.1.2.6 DHA3103C

DHA3103C was notched approximately 0.5 mm using a swiss file with a sharp 60° edge prior to pre-crack loading. The number of cycles required to pre-crack was 39,100. At this point a double sided CFRP patch with three layers per side was applied. Once the patch had cured, the beam was tested cyclically until failure at a remaining fatigue life of 359,681.

Crack length detection was a challenge for this specimen as this was a double sided repair. Consequently, the crack tip was not visible for the majority of the test. The main method used for crack length detection was the use of CFRP mounted strain gauges oriented in the fibre direction. Figure 4-6 shows the

locations of the fibre mounted strain gauges for this specimen. Due to the structure of the CFRP fabric, it was not always possible to locate a gauge at the prescribed distance from the cope. The gauges were mounted in the fibre direction, at the nearest accessible gauge mounting point, centred on the 45° diagonal as shown.

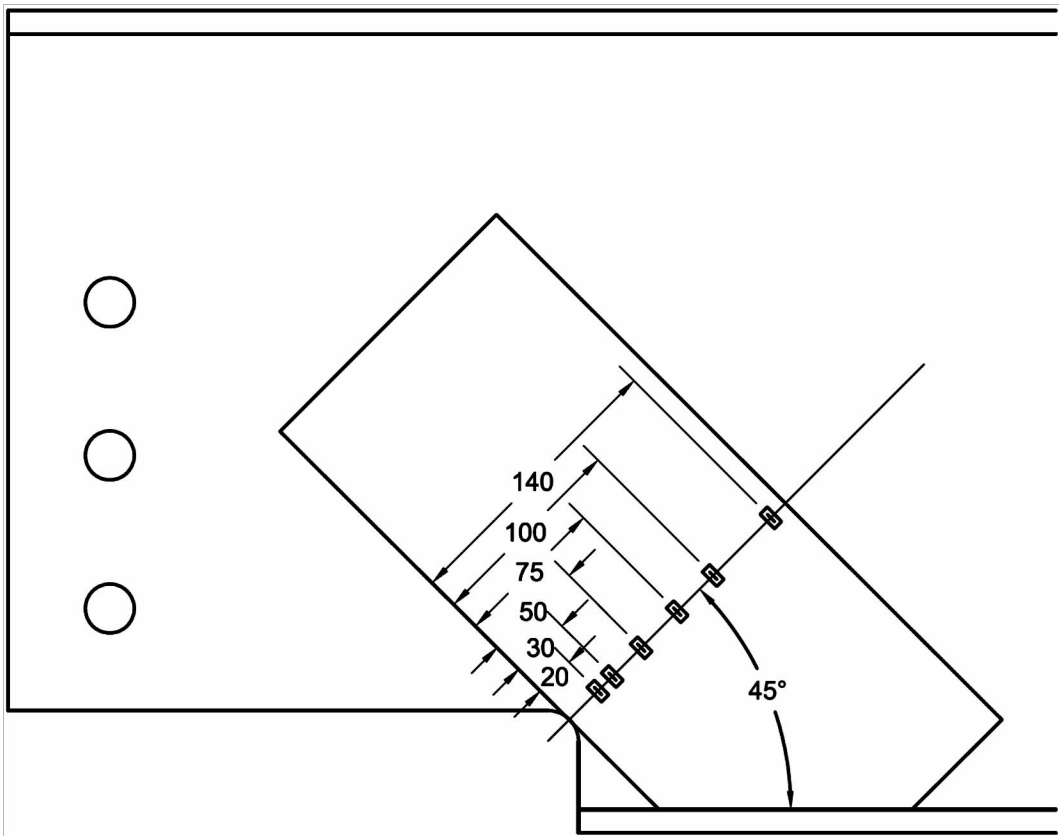

Figure 4-6 CFRP mounted strain gauge placement for DHA3103C

Figure 4-7 shows the strain amplitudes recorded for the CFRP mounted strain gauges on specimen DHA3103C. As discussed in section 3.3.2, the crack is considered to have crossed the gauge when there is a significant change in slope in the strain amplitude. The arrows indicate the points on the graph where the significant change in slope occurred. The arrow labels indicate the number of cycles corresponding to that point.

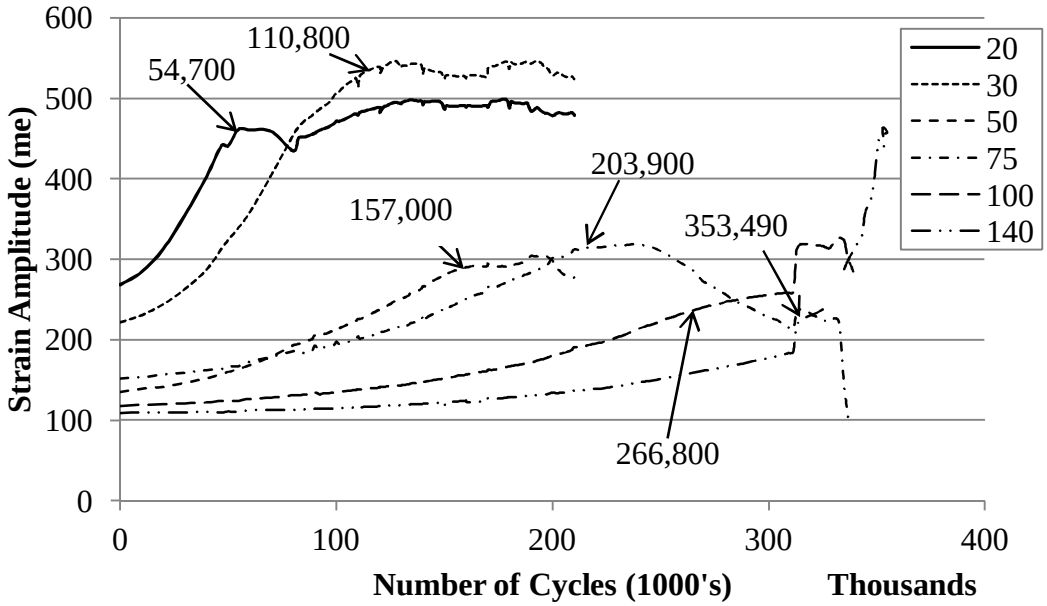

Figure 4-7 Strain amplitudes for carbon fibre mounted gauges on specimen DHA3103C

Table 4-4 shows the summary of the number of cycles at which the strain amplitude chart (Figure 4-7). The actual distance from the cope for the gauges is also reported. The crack length at these numbers of cycles was calculated using calibration equation [4-1].

Table 4-4 CFRP strain gauge calibration data DHA3103C

Gauge	N_R	*Distance from Cope (mm)*	*Calculated Crack Length (mm)*
20	54,700	21	18
30	110,800	32	28
50	157,000	53	48
75	203,900	74	74
100	266,800	101	99
140	353,490	138	140

Figure 4-8 shows the crack growth progression of beam DHA3103C. Detecting the crack length was a challenge as it could not be measured directly in the patched area. Four lines are visible on this chart. The first two lines, with filled

diamonds and squares, indicate the delamination to the end of the patch for the CFRP patch on the West and East sides of the beam respectively. The number of cycles and perpendicular distance from the cope were recorded for each side of the patch as each delamination occurred. The third line, with the filled triangles, indicates interpolated crack length based on the CFRP mounted strain gauges as discussed in section 3.3.2. The fourth line, marked with x's indicates the crack growth measured visually once the crack extended beyond the CFRP patch. The crack length indicated on this line is a chord length from the origin of the crack to the crack tip.

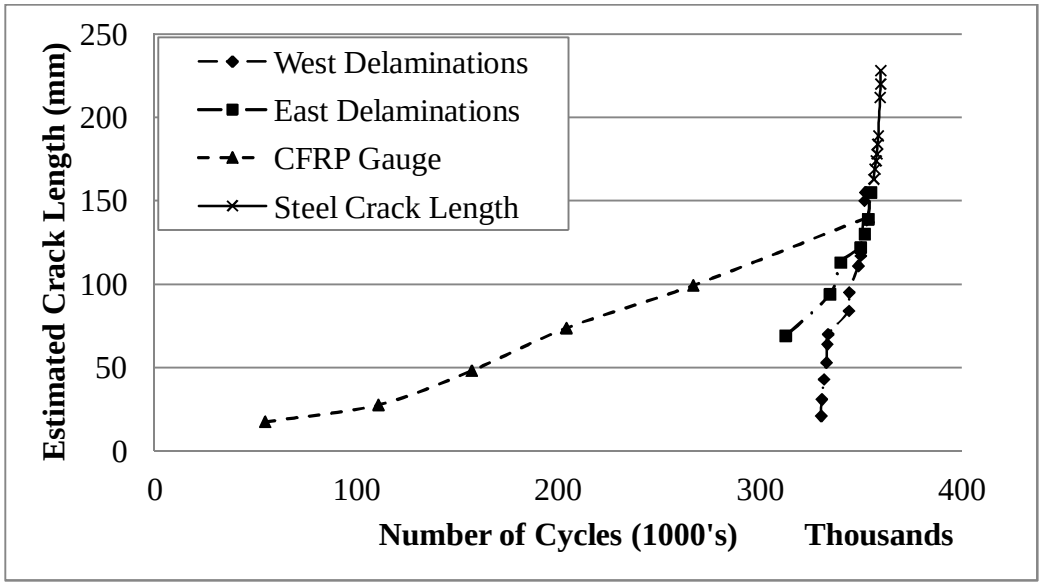

Figure 4-8 Crack length for double sided three layer per side repair DHA3103C

The crack growth for this beam reported in Figure 4-2 is a combination of the strain gauge data and bare steel data from Figure 4-8. The CFRP data for a crack length of 140 mm has been omitted due to the fact that major delamination has already started occurring at that point. For this reason the CFRP data is no longer an indicator of actual crack length.

4.1.3 Crack Propagation Angle

Due to the interaction of the CFRP and steel, the stress state in the steel is altered from the unrepaired stress state. This alteration causes a shift in the crack propagation angle in the steel for the repaired specimens. The crack propagation angle was recorded after beam failure by tracing the crack path onto a transparent sheet. The sheet was first carefully levelled to be along the same horizontal and vertical axes as the beam. Once levelled, it was taped in place and the crack path traced using a wet erase marker. Tangents were drawn to the crack path furthest from the support, and the angles of those tangents were measured.

Figure 4-9 shows all the cracks for all the specimens. In many cases, the crack angle changed very little after the pre-crack, to the extent that it was indistinguishable over the short pre-crack length. In these cases, the first angle includes the pre-cracked section. One notable difference is in the double sided repair, DHA3103C. In many cases, the angle was so close to the pre-crack angle that it could not be visually differentiated over the 10 mm of the pre-crack.

Table 4-5 summarizes crack progression with respect to the vertical axis for each specimen. The angle reported is the angle of the first segment, past the region where the pre-crack occurred. The length reported is the length of the segment of the crack which is parallel to the angle reported. For the unrepaired specimen, the crack angle started at 36.6° degrees and continued at that angle for 145 mm before deviating to 43.9° from the vertical. This correlated well with existing observed crack angles of 35° from the vertical for specimens with similar geometry to those in this experimental study (Yam and Cheng 1990). The crack length reported for the double sided specimen, DHA3103C, includes the pre-crack length, though the crack deviated significantly from this angle as seen in Figure 4-13.

Table 4-5 Angle of major crack propagation

Specimen	*Angle*	*Length (mm)*	*Deviation from unrepaired*
NH	36.56°	145	0°
SHA3103C	30.90°	44	-5.66°
SHL3103C	38.40°	188	+1.84°
SHO3103C	32.54°	151	-4.02°
SHA6103C	28.42°	66	-8.14°
DHA3103C	13.70°	119	-22.86°

Figure 4-10 through Figure 4-15 show a close up of the crack angles for each individual beam.

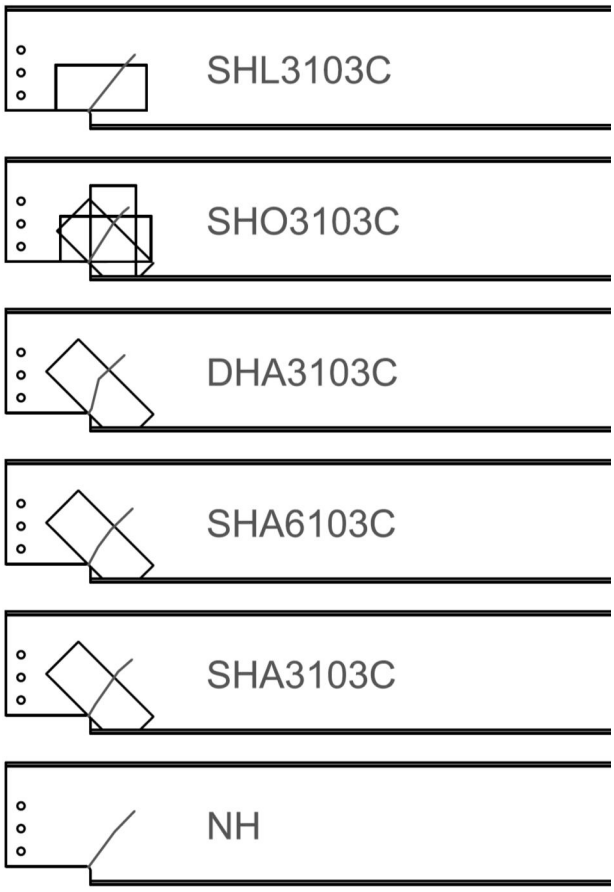

Figure 4-9 Crack Propagation Angles

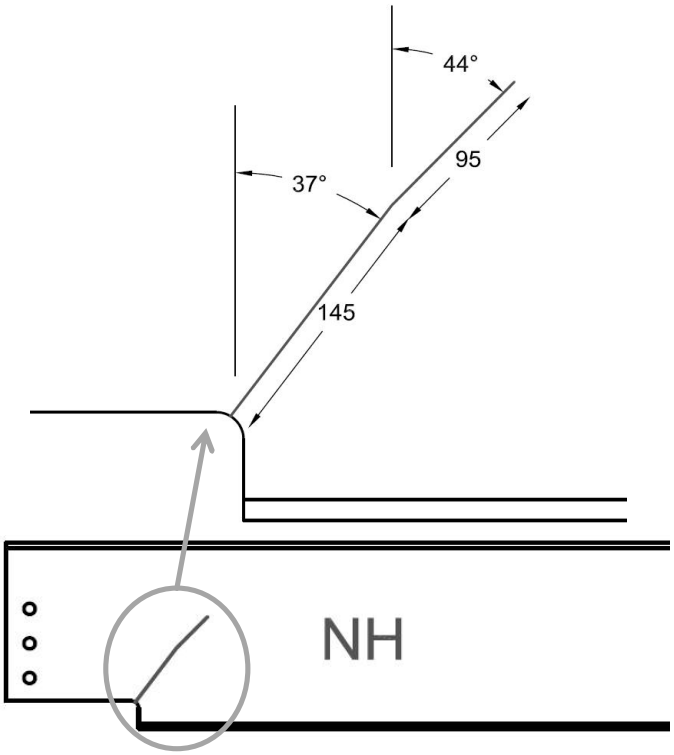

Figure 4-10 Crack angle detail for unrepaired specimen

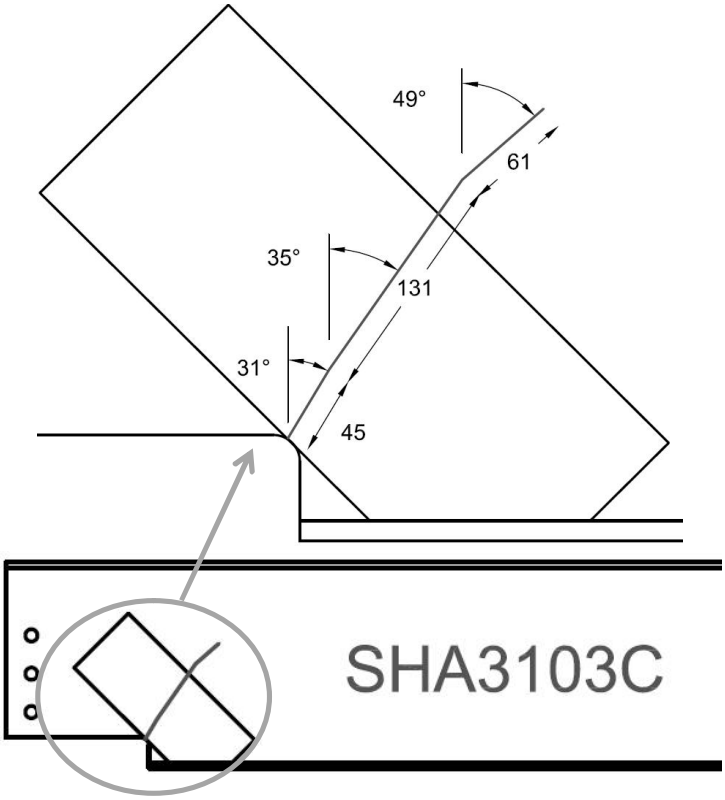

Figure 4-11 Crack angle detail for single sided three layer angle repair

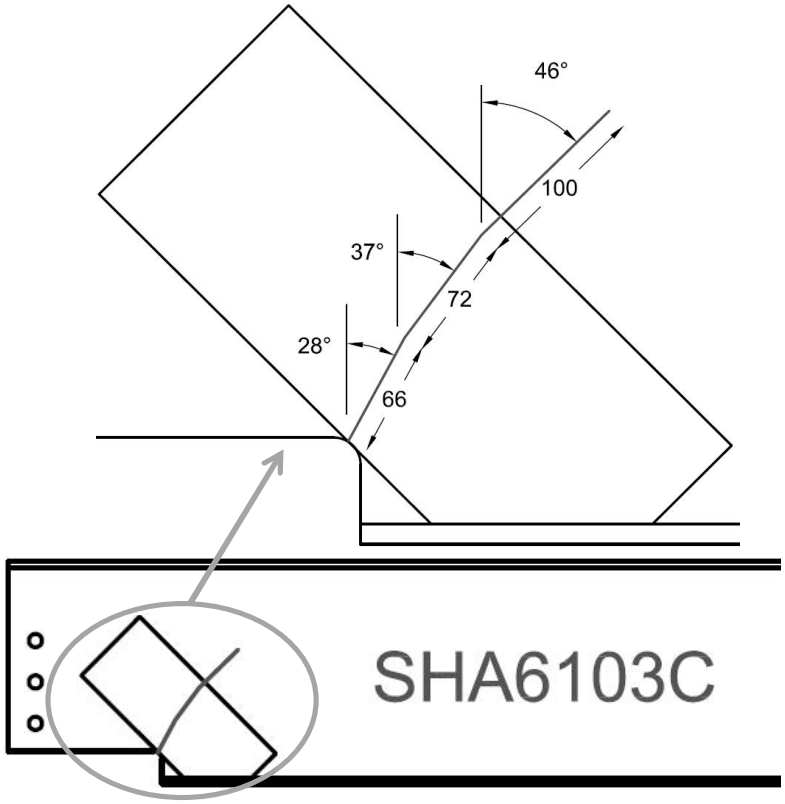

Figure 4-12 Crack angle detail for single sided six layer angled repair

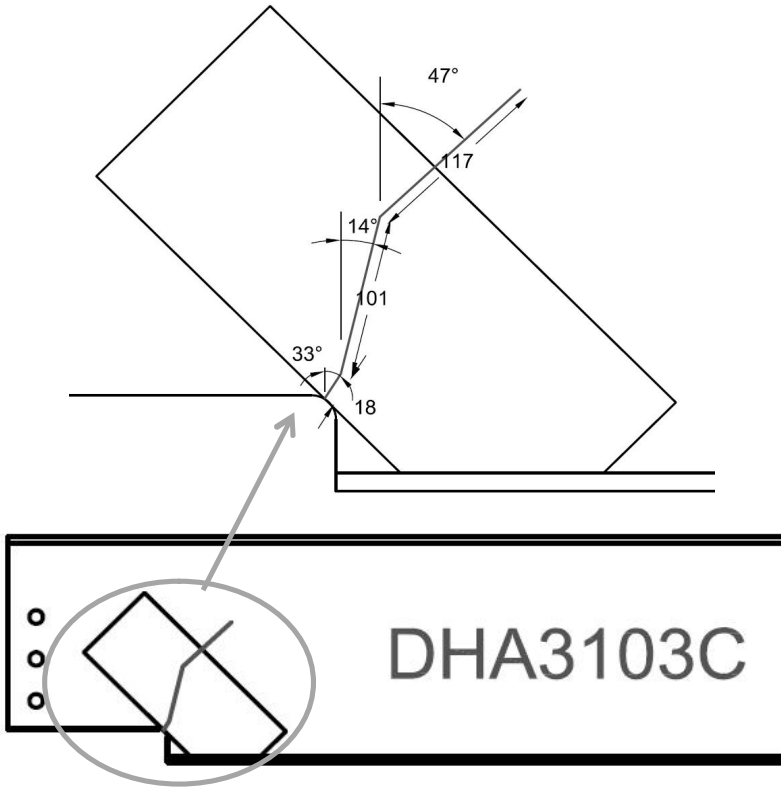

Figure 4-13 Crack angle detail for double sided repair

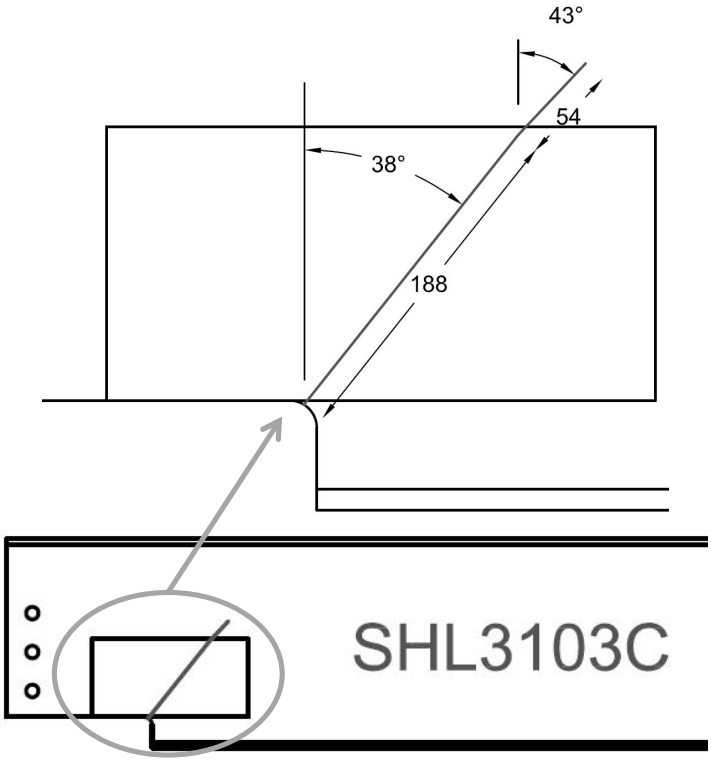

Figure 4-14 Crack angle detail for single sided three layer longitudinal repair

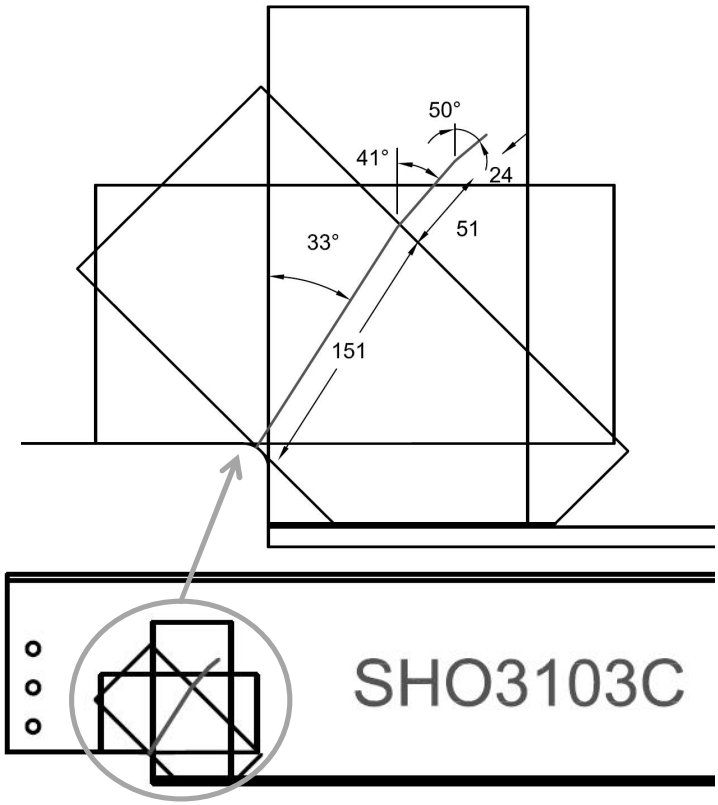

Figure 4-15 Crack angle detail for multi-directional repair

4.2 Discussion

4.2.1 Effect of Repair Eccentricity

Figure 4-16 shows the effect of repair eccentricity on the effectiveness of the repair. The effectiveness of the repair is defined as the remaining fatigue life (N_R) of the repaired specimen divided by the remaining fatigue life of the unrepaired specimen. The double sided repair DHA3103C yielded more than triple the fatigue life of the specimen at a crack growth to 30 mm. The single sided repair with an equivalent number of layers, SHA6103C yielded an increase in effectiveness of only 62%. The effectiveness for all specimens decreased as the crack grew.

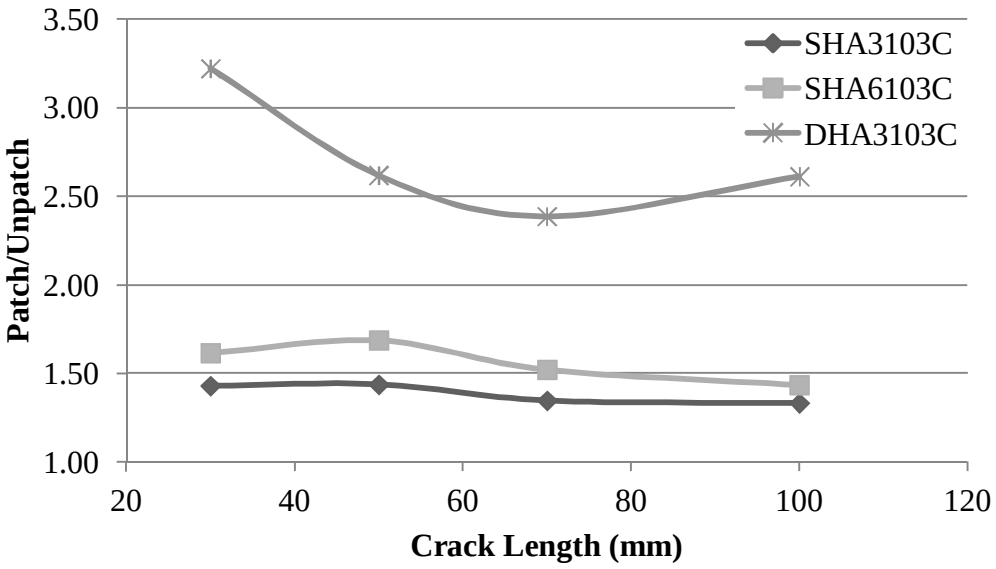

Figure 4-16 Effect of repair eccentricity with respect to crack length

Major failure for all specimens occurred in the adhesive layer. The vast increase in effectiveness for the double sided repair can be explained partially by the fact that for a double sided repair there are two shear planes. Figure 4-17 shows the load transfer mechanism for (a) a double sided repair (DHA3103C) and (b) a single sided repair (SHA3103C). For a member in double shear (a), the total load (P) is divided by the number of shear planes, making the load carried by the patch

on each side only half of the total load. Consequently only half of the load is transferred across each adhesive layer. For a member in single shear (b), however the full load is transferred across the adhesive layer to be carried by the CFRP patch. Since the total thickness of the CFRP patches for DHA3103C and SHA6103C are equivalent, the tensile capacity is also equivalent. Therefore, the shear transferred by each plane of adhesive for DHA3103C is only half of the shear transferred by SHA6103C, an equivalent system with only one shear plane.

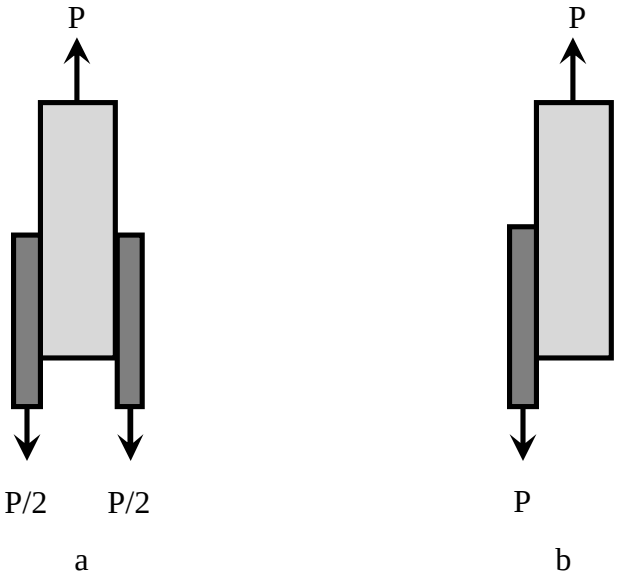

Figure 4-17 Effect of repair eccentricity on the shear transfer to the CFRP patch for a) DHA3103C and b) SHA6103C

Other possible reasons for early failure of the single sided repair include out-of-plane bending in caused by the stress path moving along a path which is no longer concentric to the specimen. Out-of-plane bending can also cause prying action in the adhesive as shown in Figure 4-18. Out-of-plane bending moment causes the entire system to bend, including the CFRP layer. Since the CFRP is continuous where the steel is cracked, it cannot bend at such a sharp angle as the steel does. This gradual curvature causes the CFRP to pull away from the steel, putting tension in the adhesive layer. The prying phenomenon was observed during

testing, however due to physical constraints from the test set-up, it could not be photographed.

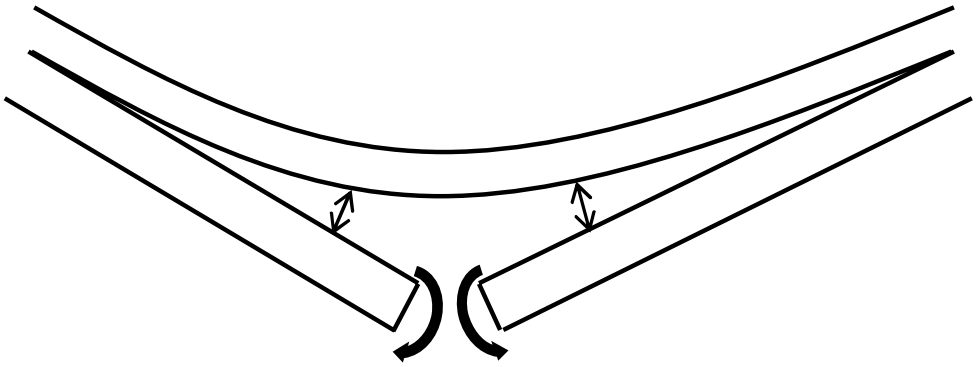

Figure 4-18 Prying action in the adhesive

4.2.2 Effect of Repair Orientation

One interesting thing to note is the change in patch effectiveness as the crack grows, as shown in Figure 4-19. The angled repair lost effectiveness after 50 mm crack length and the longitudinal repair maintained its effectiveness, while the orthogonal repair gained effectiveness. The increase in effectiveness is likely due to the ability of the stress to develop alternate paths along the different fibre orientations as the crack grows.

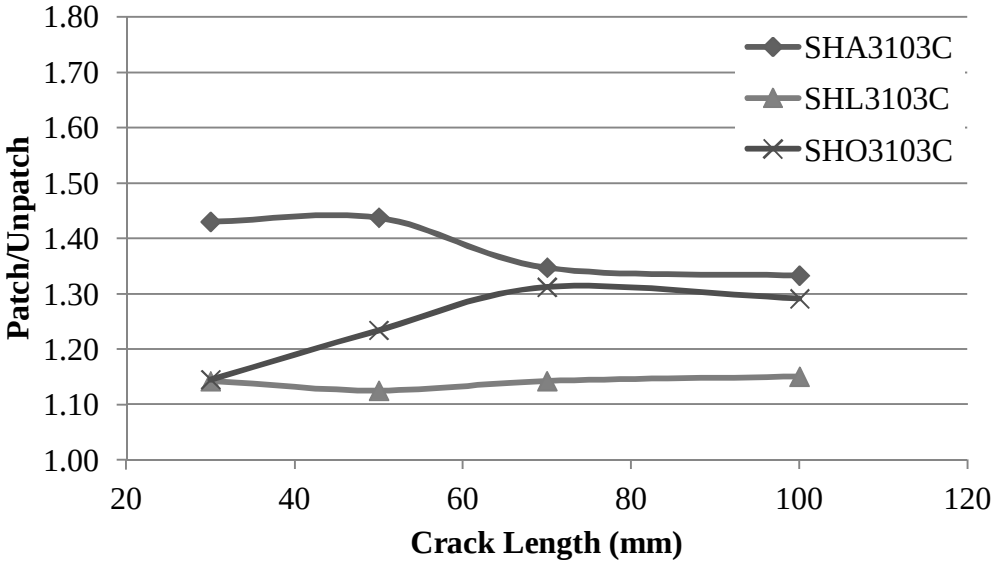

Figure 4-19 Effect of patch orientation with respect to crack growth

CFRP delamination was recorded during testing by use of the tap method. A hard object such as a screwdriver was tapped against the patch at various locations. The sound produced indicated whether the CFRP patch was bonded to the steel (hollow sound) or if it had debonded (sharp, tinny sound). The debond front was recorded directly on the CFRP patch using a white marker. Due to the presence of strain gauges on the angled repairs, this could only be done for the longitudinal and multidirectional repairs. Figure 4-20 shows the progress of CFRP delamination for SHL3103C (a) and SHO3103C (b). As the CFRP debonded from the steel for SHL3103C, the delaminated area propagated very quickly to the edge of the patch. The debond front tended to stay nearly perpendicular to the fibre direction. When the debonded region reached the edge of the patch, the fibres from the debonded area would shear away from the remainder of the patch, leaving no contribution to the CFRP strength from the debonded fibres. In Figure 4-20(b), it is clearly visible that the angle of the debond front changes as the debond encounters the different layers of CFRP. Long past when the longitudinal layer had debonded completely, there was still a contribution to the strength of the patch from the angled and vertical layers.

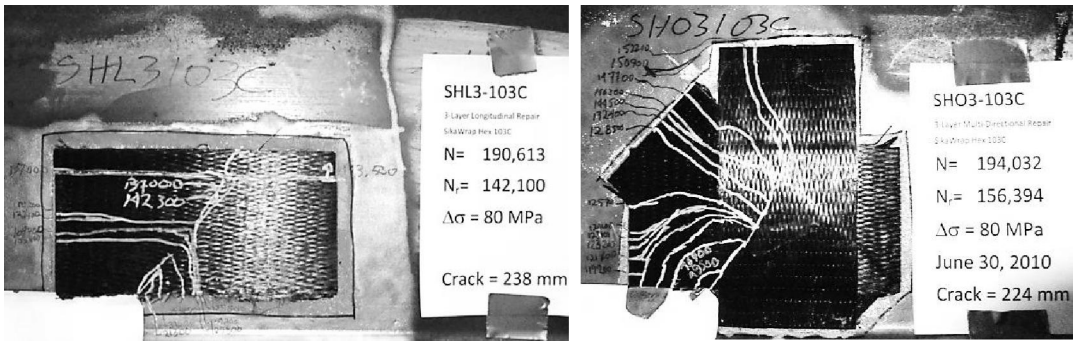

a b

Figure 4-20 CFRP adhesive debond propagation patterns for a) SHL3103C and b) SHO3103C

4.2.3 Effect of ETR

Figure 4-21 shows the change in effectiveness of the two single sided angled repairs, SHA3103C and SHA6103C, with respect to crack length. SHA6103C

had double the ETR over DHA3103C; however, doubling the ETR did not double the patch effectiveness, but rather increased it by only 57% from 1.44 effectiveness to 1.69 effectiveness for SHA3103C to SHA6103C respectively.

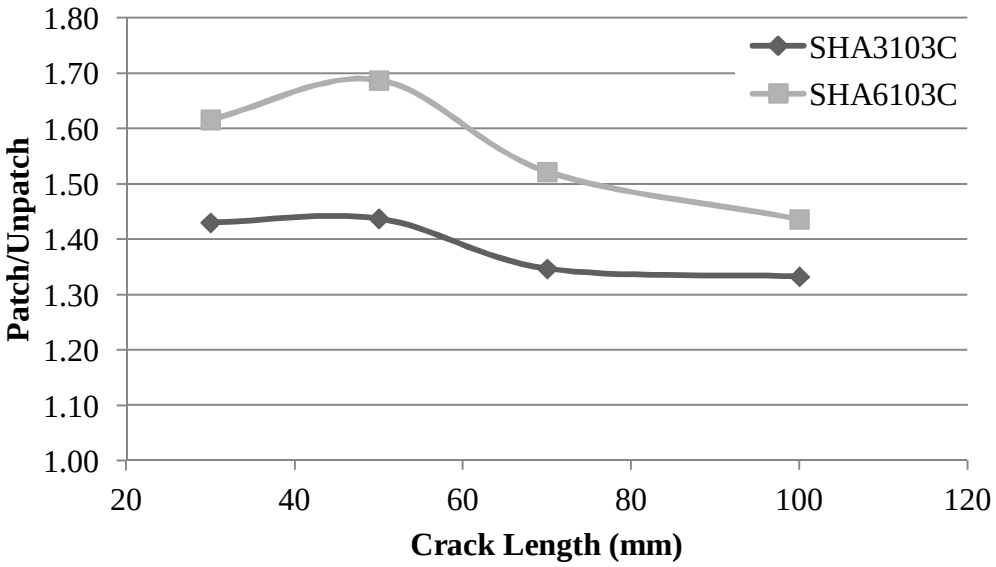

Figure 4-21 Effect of ETR with respect to crack growth

One possible reason for this is related to the fact that the main failure mode was adhesive debond. Failure in every case was in the adhesive layer for the specimens. Increasing the thickness of the patch may increase the theoretical maximum stress the patch can carry; however, the stress the adhesive layer can transfer to the CFRP is not affected. In essence, doubling the ETR did no more than to raise the stress carried in the adhesive. This can be seen by the history of patch debonding. The first major patch debond (where the CFRP debonded completely to the end of the fibres) occurred at N_R = 149,500 cycles and 122 mm crack length for SHA3103C, but at N_R = 109,200 and 55 mm for SHA6103C. For the six layer repair, the fatigue life extension was significant prior to adhesive debond. Unfortunately, debonding progressed more rapidly and debond to the edge of the patch occurred at a much smaller number of cycles and total crack length.

More research is required to determine the effectiveness of increasing the patch thickness. This research includes performing a double sided six layer test for comparison of results, and repeating the experiment with different adhesive/CFRP systems.

4.2.4 Crack Propagation Angle Discussion

An analysis was performed on the crack propagation angle for specimen DHA3103C. This specimen was chosen because the crack propagation angle changed the most drastically from the unrepaired case. For NH, the crack propagation angle in the patch range was 36.6° from the vertical as seen in Figure 4-13. DHA3103C had a main crack propagation angle of 13.7° from the vertical, as seen in Figure 4-10.

The following upper bound analysis was based on the assumptions that the CFRP acts as an anisotropic unidirectional material which can alleviate some of the tension in the fibre direction and that shear influence of the FRP on the steel is negligible. With these assumptions, the analysis can be done using the Mohr's circle method(Beer and Johnston 1992). Using this method, the crack tip region in the steel was analyzed. Figure 4-22 shows the stress state for the unrepaired steel on the left side, and on the right is the respective Mohr's circle representation.

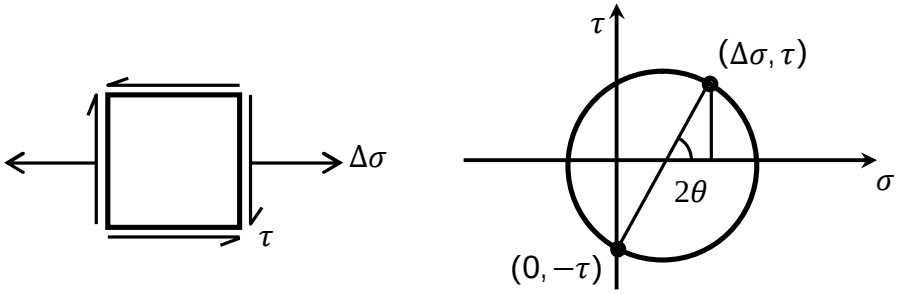

Unrepaired Stress State

Mohr's Circle Representation

Figure 4-22 Mohr's circle representation of unrepaired stress state

Knowing that for an unrepaired specimen, the crack propagation angle (θ) is 37° from the vertical, and that the unrepaired stress state in the steel included pure tension along the longitudinal axis (Δσ) as well as a shear force (τ), the proportion of shear to longitudinal stress can be determined. If we let θ = 37° and solve for τ in terms of Δσ, then the centre of the circle (c) is at Δσ/2 and

$$\tau = \frac{\Delta\sigma}{2}\tan(2\theta) \quad \textbf{[4-2]}$$

From this we determine τ = 1.65Δσ. Knowing both the co-ordinates, we can find the radius (r) and centre (c) of the Mohr's circle and from that, the principal stresses in tension (σ_1) and compression (σ_2).

$$r = \sqrt{\left(\frac{\Delta\sigma}{2}\right)^2 + (\tau)^2} = \sqrt{\left(\frac{\Delta\sigma}{2}\right)^2 + (1.65\Delta\sigma)^2} = 1.7\Delta\sigma \quad \textbf{[4-3]}$$

$$\sigma_1 = c + r = \frac{\Delta\sigma}{2} + 1.72\Delta\sigma = 2.2\Delta\sigma \quad \textbf{[4-4]}$$

$$\sigma_2 = c - r = \frac{\Delta\sigma}{2} - 1.72\Delta\sigma = -1.2\Delta\sigma \quad \textbf{[4-5]}$$

Knowing the principal stresses makes it possible to find the stress state in the fibre direction. Figure 4-23 shows the principal stress state and the Mohr's circle representation of the required rotation to find the stresses in the fibre direction. The fibre direction for this specimen was measured using the same method as the crack angle. For DHA3103C, the fibre direction was calculated to be -46° from the vertical with the negative indicating the rotation is counter clockwise. This gives the principal tension field for the fibre direction of 44° clockwise rotation from the vertical. The additional rotation required to align the steel element with the fibre direction is θ = 8° clockwise. In the figure, σ_x' and σ_y' represent the stresses parallel and perpendicular to the fibre direction and τ' represents the shear stresses at that rotation. Using the following formulas,σ_x', σ_y' and τ' were determined:

$$\tau = r\sin(2\theta) = 1.72\Delta\sigma\sin(16°) = 0.45\Delta\sigma \quad \textbf{[4-6]}$$

$$\sigma_x' = c + r\cos(2\theta) = \frac{\Delta\sigma}{2} + 1.72\Delta\sigma\cos(16°) = 2.16\Delta\sigma \quad \textbf{[4-7]}$$

$$\sigma_2 = c - r\cos(2\theta) = \frac{\Delta\sigma}{2} - 1.72\Delta\sigma\cos(16°) = -1.16\Delta\sigma \quad \textbf{[4-8]}$$

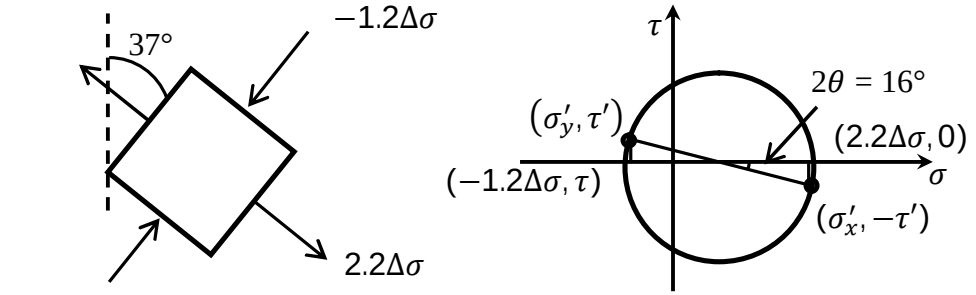

Unrepaired Principal Stresses

Mohr's Circle Representation

Figure 4-23 Mohr's circle representation of unrepaired principal stresses and rotation to fibre direction

Figure 4-24 shows the stress state in the fibre direction and its Mohr's circle representation. The dashed arrows combined with the solid arrows on the stress state represent the stress state in the unrepaired steel. This unrepaired stress state is reflected by the dashed circle on the Mohr diagram. Based on the anisotropic nature of the CFRP patch, one assumption that can be made is that the CFRP takes a portion of the stresses aligned with the fibre direction but does not affect the shear or perpendicular stresses. Using this assumption, then the principal stresses and the principal stress direction in the steel will change to reflect the altered stress state. The upper bound of this assumption is if the CFRP takes 100% of the stress oriented in the fibre direction. Eliminating the dashed arrows in the fibre direction models the stress state in the steel after the CFRP patch has taken this stress from the steel. This repaired stress state in the steel is reflected on the Mohr's circle diagram by the smaller solid circle. The angle of rotation on the Mohr's circle diagram to the new principal stresses was $2\theta' = 38^o$. Therefore, $\theta' = 19^o$. Subtracting this angle from the fibre direction yields a predicted angle of crack propagation of 25° from the vertical, which is not sufficient to explain the full crack propagation angle shift.

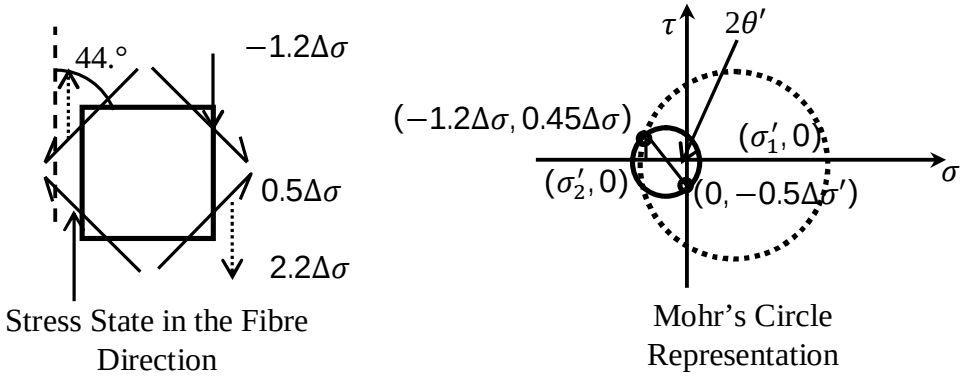

Stress State in the Fibre Direction

Mohr's Circle Representation

Figure 4-24 Stress state in the fibre direction without (dashed) and with (solid) CFRP influence

Alternatively, an analysis can be performed to determine what interaction must occur in order to shift the crack angle to 14° from the vertical. Figure 4-25 shows the unrepaired stress state at the crack propagation angle of 14° from the vertical. The minimum interaction with the CFRP patch that is required to render this the principal stress direction would be to have the entire shear portion of the stress taken by the CFRP. This would leave the principal stresses of $1.7\Delta\sigma$ and $-0.7\Delta\sigma$ for the repaired stress. This repaired stress state is shown as the dashed inner circle in the Mohr's Circle representation.

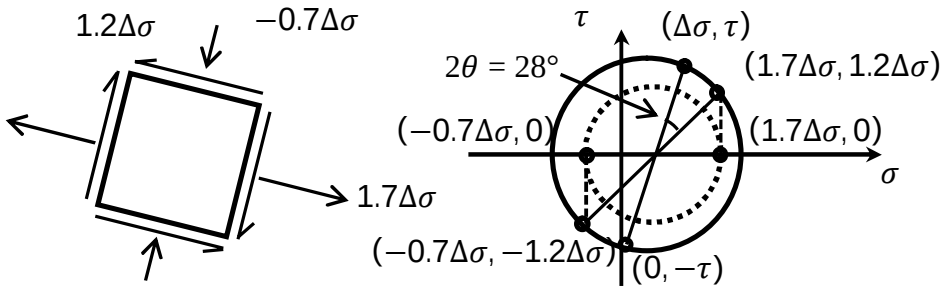

Unrepaired Stress State at Crack Angle (14°)

Mohr's Circle Representation

Figure 4-25 Mohr's circle representation of unrepaired stresses at crack propagation angle

Figure 4-26 shows the repaired element from Figure 4-25, rotated to the fibre direction. On the corresponding Mohr's Circle Representation, this repaired

stress state is shown by the dashed circle and line, and contrasted to the unrepaired stress state in the steel, shown by the solid circle and line. When rotated to the fibre direction, it becomes apparent that the minimum interaction between the steel and CFRP would require the CFRP to share the tensile and compressive forces. Also, using this lower bound assumption, the application of a CFRP patch would increase the shear in the steel.

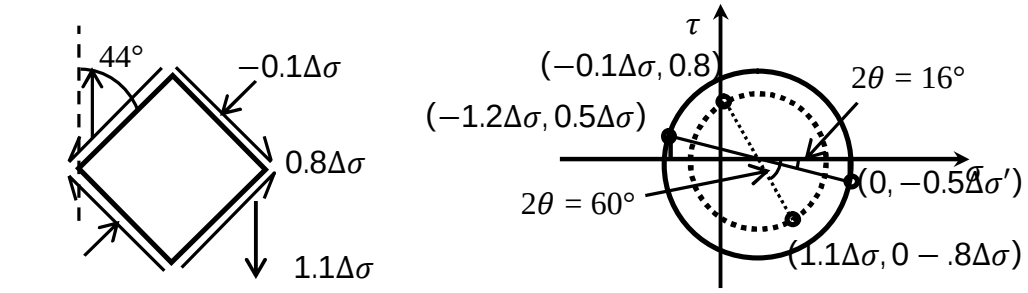

Repaired Stress State in the Fibre Direction

Mohr's Circle Representation

Figure 4-26 Mohr's circle representation of repaired stress state in the steel in the fibre direction

Another consideration for the crack propagation shift is to look at the shear induced from the crack opening at an angle to the CFRP fibre direction. This concept is illustrated in Figure 4-27. Figure 4-27(a) shows the crack closed. The crack opening angle depicted is counter-clockwise of the fibre direction. Figure 4-27(b) shows that the CFRP fibres experience a counter clockwise shear along the plane of crack opening. This is reflected in the steel via a clockwise shear in the steel as shown in the figure. Though this is occurring away from the crack tip, the shear would travel up the crack to be present at the crack tip. The application of a clockwise shear on the crack plane to the principal stress state would shift the crack propagation direction clockwise, away from the vertical. This phenomenon should also be taken into account in further analysis of the crank propagation angle shift.

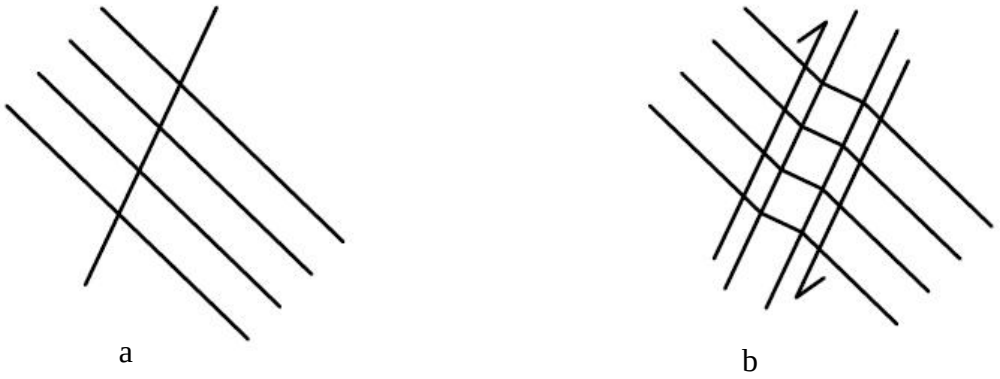

Figure 4-27 Shear induced in steel from crack opening at an angle to FRP fibre direction: a) crack closed, b) crack open

The interaction between the CFRP and steel is complex. Determining the exact mechanism which causes the crack propagation angle to shift is beyond the scope of this project. More detailed analysis is required, including use of finite element modelling, to determine the exact nature of this behaviour.

5 Failure Prediction Model

5.1 Model Parameters

An analytical case study was undertaken to evaluate the effectiveness of an FRP patch applied to a fatigue crack in the web of a coped beam. A coped beam has a complex combination of bending and shear stresses at the cope location. In addition the shape of the section is reduced and there is a stress concentration at the cope location due to the shape of the cope itself. Specimens with the same geometric proportions as those used by Yam and Cheng (1990) were used for the case study. As follows, the stress concentration profile (K_t), and geometric stress correction factor (F_G) were determined from that study directly.

The beam is modelled as simply supported with a span length of 3670 mm. The beam is loaded cyclically at mid span (1605 mm from the cope). The modelled patch is a SikaWrap Hex 103C CFRP patch bonded to the steel at the crack location. The patch is 150 mm in width, 1.016 mm thick per layer and has an average cured modulus of elasticity of 70.5 GPa. Sufficient adhesive bond area to develop the full strength of the patch is assumed to be present, thus the adhesive is not considered in this study. An initial crack size of 10 mm was chosen to simulate the member pre-crack. The final crack length was chosen to be 30 mm.

Three parameters were considered for the analytical study. These were: stress range ($\Delta\sigma$), equivalent stiffness ratio (ETR), and orientation of repair. The parameters were chosen to simulate field conditions. They take into account bridge loadings and accessibility of the repaired member. Eccentricity was not one of the parameters modelled as the source data for ΔSIF does not include any double sided repaired specimens.

Two stress levels are tested: $\Delta\sigma$ = 40 MPa and $\Delta\sigma$ = 80 MPa. These stress ranges were chosen to represent the stress ranges present in beams in service. The high stress range (80 MPa) was modelled after the wheel load from axles 2 and 3 of a CL-800 standard truck. The CL-800 is a specified design load in Alberta, Canada

(Alberta Infrastructure and Transportation 2007). The wheel and axle loads are proportioned from the CL-625 truck specified in the Canadian Highway Bridge Design Code, CSA S6-06 (2006).

The ETR is varied by varying the number of layers of CFRP sheet bonded to the web at the crack location. The patches applied consist of either one or two layers of CFRP attached at the crack location. A three layer repair gives an ETR of 0.132, while six layers give an ETR of 0.264. The SIF at the midline of the specimen was considered based on the study mentioned above.

Lastly, the orientation of the repair is considered. Three configurations for the repair are considered. The first is to have the CFRP patch applied with the fibres oriented perpendicular to the predicted crack direction. This should ensure the tensile stresses in that location are fully engaged by the repair. There are situations in the field, however where it may not be possible to fully develop the tensile strength of the repair perpendicular to a fatigue crack, due to clearances, location of flanges, bolts, holes, etc. In these locations it may be prudent to apply a patch with the fibres oriented in the direction where there is maximum allowable development length. In this study, the maximum allowable development length has been modelled in the longitudinal axis of the W410 x 54 member.

It is assumed that the strength of the FRP repair is unidirectional. In other words, it can only develop tension stress in the direction of the fibre orientation. If the patch is not oriented with the fibres perpendicular to the crack, then the full tension stresses cannot be carried by the patch.

The model assumes crack propagation along a plane of principal tension oriented at 45° to the vertical. To account for difference between the repair orientation and crack direction for the longitudinal and orthogonal models, the following approximation (Equation [5-1]) is used:

$$ETR_{effective} = \sum ETR\, sin(\varphi) \quad [5\text{-}1]$$

Where φ is the angle between the fibre orientation and the crack direction. For example, for a longitudinal repair, the effective ETR would be 3 x 0.044 x $\sqrt{2}$ = 0.092. This is equivalent to three layers at ETR = 0.044/layer at 45° to the crack.

5.2 Linear Elastic Fracture Mechanics

Linear Elastic Fracture Mechanics (LFEM) was employed to determine the remaining fatigue life of the coped girders (Anderson 2005). This section is a summary of the methods used in the analytical model.

In LEFM, the Mode I – pure tension – stress intensity (K_I) factor is a function of stress (σ), crack length (a) and various correction factors (F).

$$K_I = F\sigma\sqrt{\pi a} \quad \textbf{[5-2]}$$

The correction factor [5-3] is a product of various factors to correct for free surface (Fs), finite width (FW), crack front shape (FE) and stress gradient (FG).

$$F = F_S F_W F_E F_G \quad \textbf{[5-3]}$$

For this experiment, a through crack was assumed, forcing F_S to 1.12 and F_E to unity. Another correction factor was added to account for the change in stress intensity due to the addition of the CFRP (ΔSIF). Therefore, the correction factor F can be reduced to:

$$F = 1.12\sqrt{sec\left(\frac{\pi a}{w}\right)}\, F_G(\Delta SIF) \quad \textbf{[5-4]}$$

where a is the crack length and w is the width of the plate. For this study, w was taken as double the depth of the coped section, or 687 mm.

The number of cycles to failure is related to K_I by the empirical formula shown in Equation [5-5]:

$$\frac{da}{dN} = C(\Delta K_I)^m \quad \textbf{[5-5]}$$

where N number of cycles to failure, and C and m are material constants. For this study the values reported by Barsom (1971), C equal to 2.179 x 10^{-13} and n = 3 were used. These values coincide with those used by Yam and Cheng (1990). Equation [5-5] can be manipulated to produce Equation [5-6] :

$$N = \int_{a_i}^{af} \frac{da}{C(\Delta K_I)^m} \quad \textbf{[5-6]}$$

Combining Equation [5-6] with Equations [5-2] and [5-4] yields the following equation for number of cycles to failure:

$$N = \int_{a_i}^{a_f} \left(\frac{da}{C\left(1.12\sqrt{\sec\left(\frac{\pi a}{w}\right)}F_G(\Delta SIF)\Delta\sigma_n\sqrt{\pi a}\right)^m} \right) \quad \textbf{[5-7]}$$

In [5-7], $\Delta\sigma_n$ represents the amplitude of the nominal cyclic stress applied. The nominal stress is the theoretical stress present at the bottom of a T-section with the same dimensions as the section reduced by the cope under equivalent loading.

Due to the complexity of the function direct integration is not possible. Numerical integration was used with an integration step (*da*) of 0.02 mm to determine the fatigue life of the structure. An initial crack size of 10 mm was chosen for a_i to simulate the pre-crack in the steel prior to repair. The final crack length, a_f, was chosen to be 30 mm.

5.3 Stress Gradient

The Green's function method was used by Yam and Cheng (1990) to determine the stress gradient due to non-uniform loading such as cope geometry. It is defined as:

$$F_G = \frac{2}{\pi}\int_o^a \frac{K_t}{\sqrt{a^2 - L^2}}\,dL \qquad \textbf{[5-8]}$$

where Kt is the normalized tension stress perpendicular to the crack.

Figure 5-1 shows the normalized stresses from the finite element analysis of four of the specimens tested by Yam and Cheng (1988) specimens. The specimens shown had a nominal radius of 10 mm, however, the actual measured cope radius after flame cut was 15 mm.

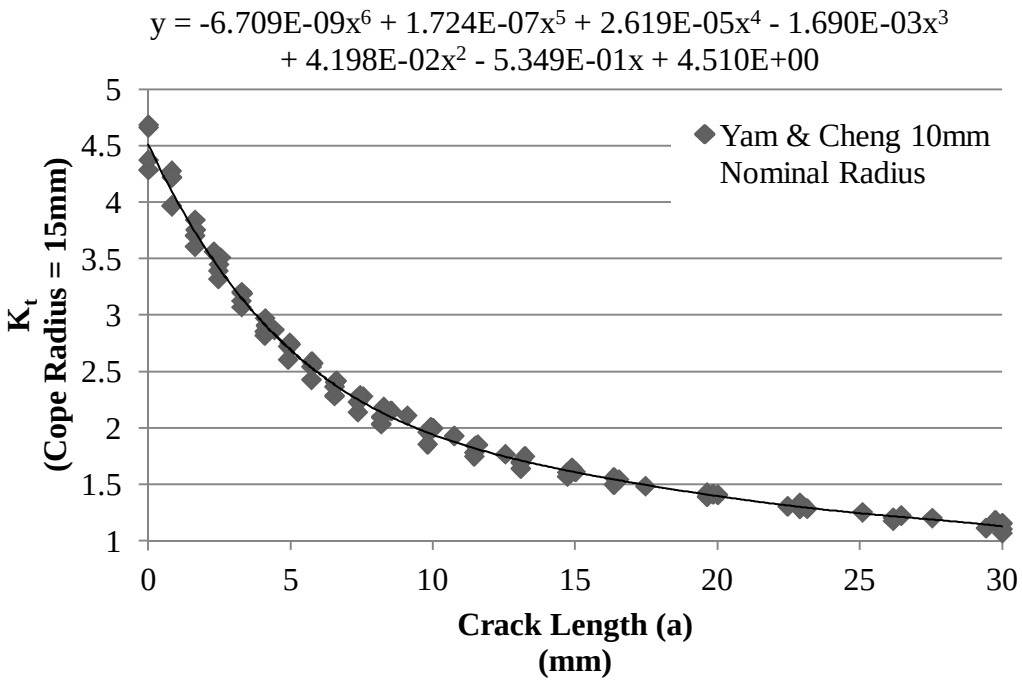

Figure 5-1 Stress concentration perpendicular to crack direction for 15 mm radius specimens (Yam and Cheng 1988)

A sixth degree polynomial was fit to the data in the format shown in Equation [5-9] to obtain a stress gradient:

$$K_t = A + Ba + Ca^2 + Da^3 + Ea^4 + Fa^5 + Ga^6 \quad \textbf{[5-9]}$$

where A through G are the constants fit to the best-fit line of the equation and a is the crack length. By applying integration by parts to Green's function (Equation [5-8]), for a sixth degree K_t as shown in Equation [5-9], a closed form solution for F_G was found, shown in Equation [5-10].

$$K_t = A + \frac{2}{\pi}Ba + \frac{1}{2}Ca^2 + \frac{4}{3\pi}Da^3 + \frac{3}{8}Ea^4 + \frac{16}{15\pi}Fa^5 + \frac{5}{16}Ga^6 \quad \textbf{[5-10]}$$

The final correction factor function is shown in Figure 5-2. It is compared to the correction factor functions Yam and Cheng (1988), calculated for their flame cut specimens with a nominal cope radius of 10 mm, and a measured radius of 15 mm.

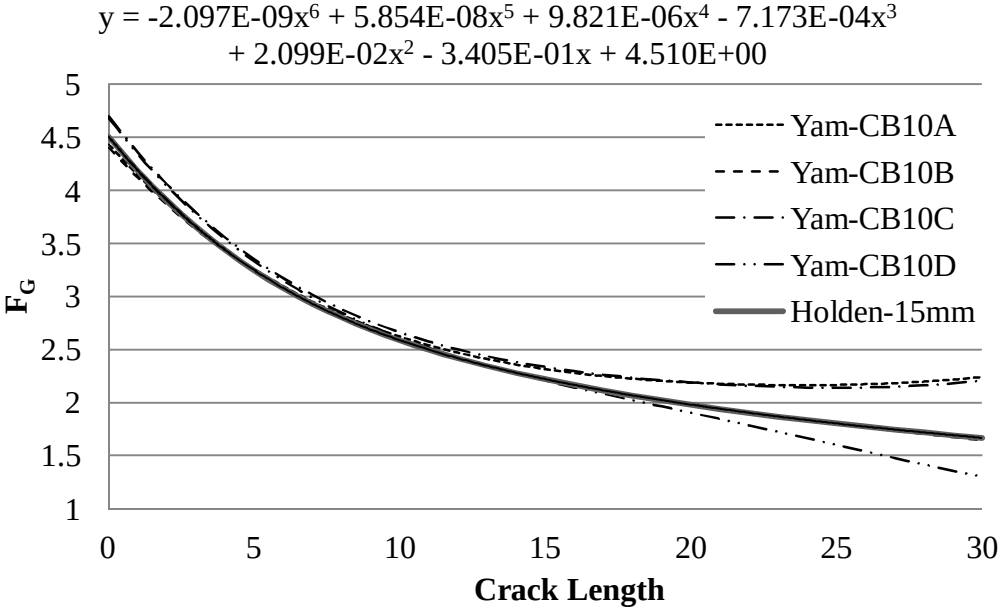

Figure 5-2 Stress gradient correction factor function compared to the correction factor functions reported by Yam and Cheng (1988)

Note the deviation in values nearing the end of the range. Yam and Cheng calculated F_G based on a fourth degree polynomial fit to their original finite element analysis data. This is the likely cause for the variance in values for their data. In no case should F_G increase as the crack lengthens.

5.4 Stress Intensity Factor Modification

Crack bridging repair of steel elements using carbon fiber reinforced polymer (CFRP) was examined by Kennedy and Cheng (1998). Steel plates (dimension = 750 mm x 400 mm x 6.5 mm) with a central crack (80 mm) were tested under uni-axial tensile loading (far end stress = 100 MPa). At the crack location, some of the specimens were reinforced with CFRP on one side. Four or six layers of 0.23 mm thick CFRP repair with an elastic modulus of 128,093 MPa were used.

With a six layer repair applied, the specimen had an equivalent stiffness ratio (ETR) of 0.139. Four layers of CFRP repair yields an ETR of 0.093. Other test parameters included the patch length, patch width, type of tapered end and patch pattern. In their study, the strain distribution in a cracked steel plate with and without CFRP patching was examined. It was shown that the strain at the crack tip could be reduced by applying CFRP patching. Higher stiffness patches reduced the crack tip stresses while lower stiffness patches reduced the stress concentrations in the steel at the patch edge. Kennedy and Cheng (1998), proposed a minimum bond length for load transfer and load redistribution based on these experimental and numerical studies.

A finite element analysis study was carried out by Lam and Cheng (2010), using ABAQUS software to determine the effect of an FRP repair on the stress intensity factor at the crack tip of a fatigue crack. For this study, the specimens tested by Kennedy and Cheng (1998) were modelled using a three layer technique developed by Naboulsi and Mall (1996), as shown in Figure 5-3, in which 2-D elements were used for steel plate, adhesive, and CFRP. The model used static analysis to obtain raw strain results under load. The contour integral method

employing the J-integral was then used to determine the SIF around the crack tip. Using Mindlin plate elements and assuming that the SIF varies linearly through the plate thickness, the SIF can be determined on both the patched and unpatched sides of the steel plate. In order to consider the nonlinear stress distribution in steel plate, a modified three layers model was introduced where the steel plate is modelled using ABAQUS standard C3D20 3-D brick elements, while the adhesive and the FRP repair are modelled as shell elements, as shown in Figure 5-4.

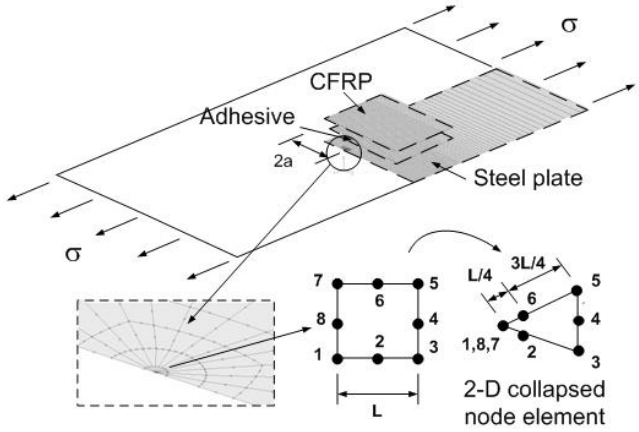

Figure 5-3 Three layers model (Lam et al. 2010)

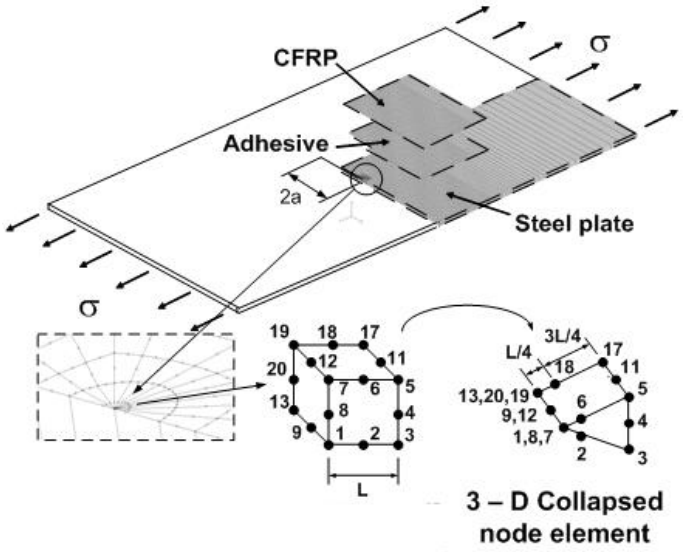

Figure 5-4 Modified three layers model (Lam et al. 2010)

Both repaired and unrepaired specimens were modelled. The SIF for the repaired specimens was normalized against the unrepaired specimens to determine the change in stress intensity at the crack tip due to the repair. Figure 5-5 shows the stress intensity factor through the thickness of the plate using both the three layers technique and modified three layers techniques.

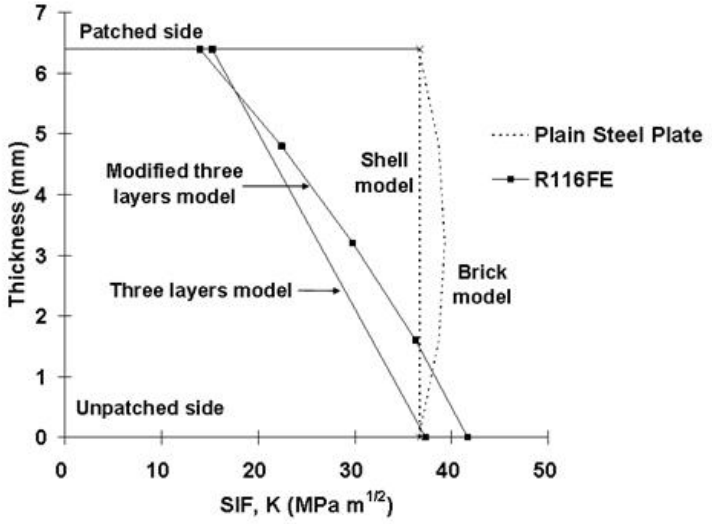

Figure 5-5 Comparison of SIF for the three layers model and the modified three layers model (Lam et al. 2010)

The results of this study (shown in Table 5-1) showed that the effect of equivalent stiffness ratio (ETR) on the SIF is far more pronounced than the effects of patch width, length or shape. When compared to the unrepaired specimen, the average SIF on the patched side was reduced to 39% for specimens with ETR of 0.139 and 46% for specimens with ETR of 0.093. On the unpatched side, the SIF showed an increase of 13% for the specimens with ETR of 0.093 and 15% for those with ETR of 0.139.

Figure 5-6 shows the linear interpolation of these results. The increase in SIF on the unpatched side is due to the eccentricity of a single sided CFRP repair causing out-of-plane bending in the specimen. The average of patched side and unpatched

side values of SIF were used to represent the repairs, representing average crack growth.

Table 5-1 Comparison of SIF values of three layers model to unrepaired plain steel (Lam et al. 2010)

Specimen	*Layer n*	*Width w* (mm)	*Length l* (mm)	*Taper* (mm)	*Modified three layers model SIF(K) MPa√m* Patch	Unpatch	$SIF_{3\text{-}D}/SIF_{steel}$ Patch	Unpatch
Plain Steel	**-**	**-**	**-**	**-**	**36.59**	**36.59**	**1.00**	**1.00**
R116FE	6	160	100	5	13.99	41.65	0.38	1.14
R216FE	6	120	100	5	14.58	41.24	0.40	1.13
R316FE	6	80	100	5	15.50	41.01	0.42	1.12
R226FE	6	120	30	3	13.48	43.01	0.37	1.18
R326FE	6	80	30	5	14.05	42.47	0.38	1.16
ETR=0.139			**Average**		**14.32**	**41.88**	**0.39**	**1.15**
R214FE	4	120	100	5	17.32	40.76	0.47	1.11
R314FE	4	80	100	5	18.12	40.57	0.50	1.11
R224FE	4	120	30	5	16.34	42.12	0.45	1.15
R324FE	4	80	30	3	16.85	41.71	0.45	1.14
ETR=0.093			**Average**		**17.16**	**41.29**	**0.46**	**1.13**

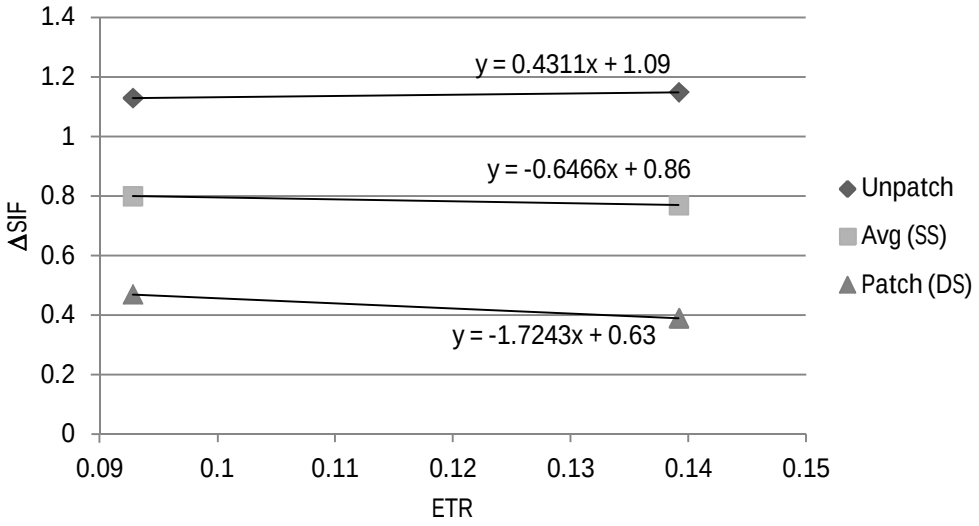

Figure 5-6 Linear interpolation of ΔSIF results (Lam et al. 2010)

5.5 Results and Discussion

The results for the analysis are summarized in Table 5-2. It shows the predicted fatigue life of each test case. Please note that most the double-sided repairs and the six layer repairs are outside the data range for ΔSIF, and therefore the data are less reliable. For this section, effectiveness is defined as the patch/unpatch ratio for the specimen.

Table 5-2 Results of analytical model

Case	*Eccentricity*	*Repair*	$\Delta\sigma_n$	*ETR*	*ΔSIF*	*Fatigue Life*	*Patch/ Unpatch*
NH	NONE	N/A	80	NA	1	33600	-
SHA3	SS	Angle	80	0.138	0.771	73400	2.18
SHA6	SS	Angle	80	0.275	0.682	106000	3.15
SHL3	SS	Long.	80	0.097	0.797	66400	1.98
SHL6	SS	Long.	80	0.195	0.734	85000	2.53
SHO3	SS	Ortho.	80	0.111	0.788	68600	2.04
SHO6	SS	Ortho.	80	0.221	0.717	91300	2.72
DHA3	DS	Angle	80	0.275	0.682	106000	3.15
DHA6	DS	Angle	80	0.550	0.504	262800	7.82
DHL3	DS	Long.	80	0.195	0.734	85000	2.53
DHL6	DS	Long.	80	0.389	0.608	149400	4.45
DHO3	DS	Ortho.	80	0.221	0.717	91300	2.72
DHO6	DS	Ortho.	80	0.443	0.573	178300	5.31

5.5.1 Effect of Effective Thickness Ratio (ETR)

Figure 5-7 shows the change in effectiveness due to effective thickness ratio of the various specimens according to the analytical model. By applying a double sided repair as opposed to a single sided repair with the same number of total layers, the effectiveness increases.

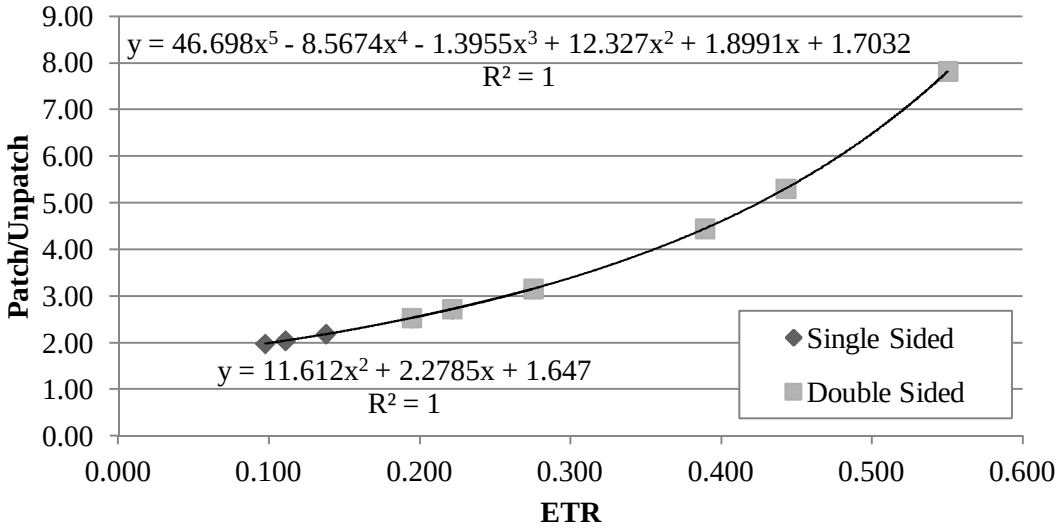

Figure 5-7 Effect of Effective Thickness Ratio (ETR), Comparing single sided to double sided specimens

5.5.2 Effect of Patch Eccentricity

Table 5-3 shows a summary in the change in effectiveness of applying a patch to a single side of a specimen as opposed to applying the same patch to both sides. The change in effectiveness DS/SS ranges from 1.28 for the 3 layer longitudinal repair per side to 2.48 for a six layer angled repair per side.

Table 5-3 Comparison of single sided repairs to double sided repairs of equivalent thickness per side

SS	*DS*	*Pattern*	*# Layers/ Side*	*N (SS)*	*N (DS)*	*DS/SS*
SHA3	DHA3	ANGLE	3	73400	106000	1.44
SHL3	DHL3	LONG	3	66400	85000	1.28
SHO3	DHO3	Ortho	3	68600	91300	1.33
SHA6	DHA6	ANGLE	6	106000	262800	2.48
SHL6	DHL6	LONG	6	85000	149400	1.76
SHO6	DHO6	Ortho	6	91300	178300	1.95

Table 5-4 shows the change in effectiveness of applying a patch of equivalent total thickness to one side as opposed to splitting the layers between the two sides

of a double-sided repair. According to the failure prediction model, there is no change in effectiveness.

Table 5-4 Comparison of single sided repairs to double sided repairs of equivalent total thickness

SS	*DS*	*Pattern*	*Total # Layers*	*N (SS)*	*N (DS)*	*DS/SS*
SHA6	DHA3	ANGLE	6	106000	106000	1.00
SHL6	DHL3	LONG	6	85000	85000	1.00
SHO6	DHO3	Ortho	6	91300	91300	1.00

5.6 Comparison with Test Results

Table 5-5 shows the comparison of the analytical model to the experimental data. All single sided repairs failed by adhesive debond in the experiment. This indicates that the CFRP could not develop its full strength. If the CFRP is at less than full strength, then the DSIF is affected, and is less than predicted by Lam and Cheng (2010).

Table 5-5 Comparison of analytical model to experimental results

Specimen	**Case**	**Test**	**Predicted**	**Test/ Predicted**	**Failure Mechanism**
NH	NH	34,400	33,600	1.02	Steel
SHA3-103C	SHA3	49,200	73,400	0.67	Adhesive debond
SHA6-103C	SHA6	55,600	106,000	0.52	Adhesive debond
SHL3-103C	SHL3	39,300	66,400	0.59	Adhesive debond
SHO3-103C	SHO3	39,400	68,600	0.57	Adhesive debond
DHA3-103C	DHA3	110,800	106,000	1.05	Adhesive debond

All single-side patched specimens had a test to predicted ratio of around 0.6. The mean test to predicted ratio was 0.59 with a standard deviation of 0.061. Though these results are quite low, this is a relatively consistent number. In fact, all single sided repair cases were within 1.4 standard deviations from the mean. The implication of this is that though the actual failure mechanism is not accounted for in the model, the model still reflects the effects of the parameters effectively.

Another possible reason for lower test to predicted results is the uneven crack front due to eccentric loading. Since the SIF is higher on the unpatched side, the crack will grow faster on that side until a critical crack angle is reached between sides where rate of crack growth becomes even from the unpatched side to the patched side. The difference this would make would be in the order of one to five millimeters extra crack length from the patched side to the unpatched side.

5.6.1 Effect of Repair Orientation

Figure 5-8 shows the effect of the repair orientation. All specimens for the repair orientation parameter are three layer single sided repairs. The effectiveness in this case is measured as the number of cycles to grow the crack from the 10 mm pre-crack to a final length of 30 mm for the unrepaired specimen divided by the number of cycles for the same crack growth for the unrepaired control specimen. The dark bar shows the theoretical effectiveness based on the analytical model proposed in chapter 5. The light bar represents the effectiveness as observed in the experiment. The most effective repair was the angled patch at an effectiveness of 1.43, followed by the orthogonal patch and finally the longitudinal patch with effectiveness of 1.15 and 1.14 respectively.

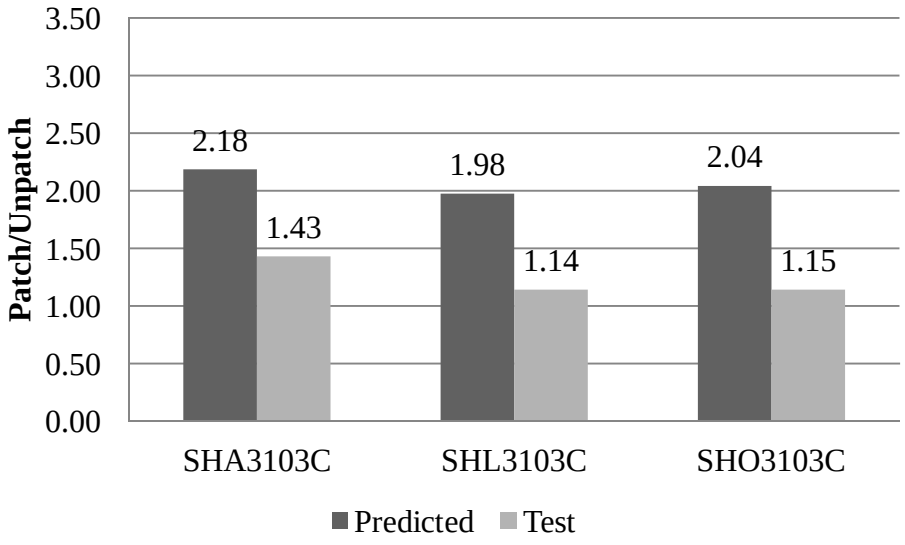

Figure 5-8 Effect of patch orientation at 30 mm crack length, comparing analytical model to experimental data

5.6.2 Effect ETR

Figure 5-9 shows the effect of the ETR. All specimens for the repair orientation parameter are single sided repairs. The effectiveness in this case is measured as the number of cycles to grow the crack from the 10 mm pre-crack to a final length of 30 mm for the repaired specimen divided by the number of cycles for the same crack growth for the unrepaired control specimen. The dark bar shows the theoretical effectiveness based on the analytical model proposed in chapter 5. The light bar represents the effectiveness as observed in the experiment. Though the analytical model predicted an increase in effectiveness of 44% (from 2.18 for the three layer repair to 3.15 for the six layer repair) by doubling the patch thickness, the actual increase was only 13% (from 1.43 to 1.62).

The decreased effectiveness can be explained by the primary failure mode, which is adhesive failure and debonding. Since the failure occurred in the adhesive layer, the patch could not have developed its full tensile strength. In this case, the effectiveness of the patch is limited by the ability of the adhesive layer to transfer the stresses to the FRP.

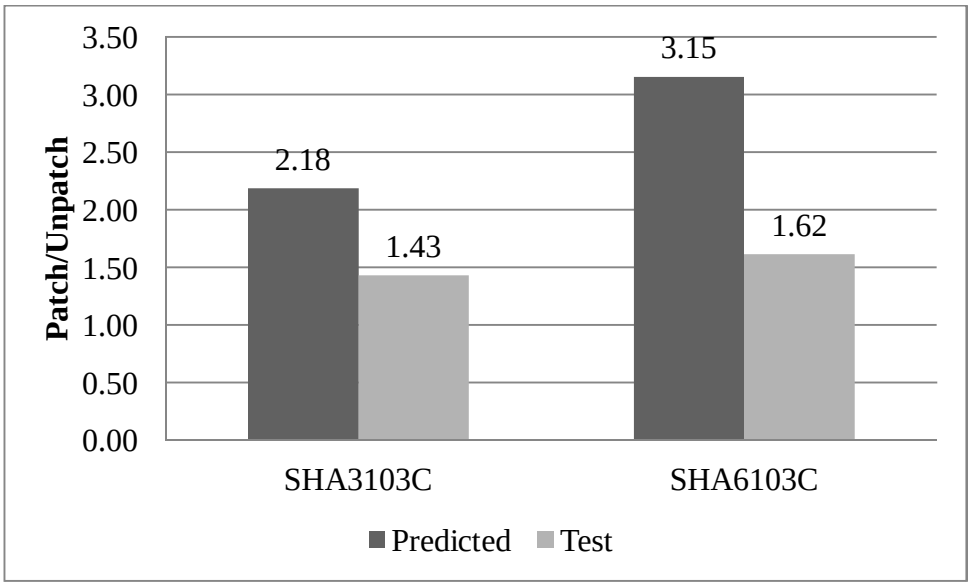

Figure 5-9 Effect of Effective Thickness Ratio (ETR) at 30 mm crack length, comparing analytical model to experimental data

5.6.3 Effect of Eccentricity of Repair

Finally, Figure 5-10 shows the comparison of the effectiveness between the analytical model and the experimental test for specimens SHA6103C with six layers applied to a single side, and specimen DHA3103C with three layers applied to each side of the web. For these two specimens the ETR is equivalent, and thus the predicted effectiveness is also equivalent at 3.15 repaired/unrepaired. The measured effectiveness in the test was only 1.62 for the single sided repair and is nearly doubled at 3.22 for the double side repair.

The single sided repair was significantly less effective in the experiment. This is due to the primary failure mode, which is adhesive failure and debonding. The double sided repair has two adhesive layers, and thus also has two shear planes for transfer of shear to the FRP patch. Two shear planes means that the stresses in each shear plane is only half that of an equivalent repair system with only one shear plane. The double sided repair, then had a much greater ability to develop full tensile strength in the patch.

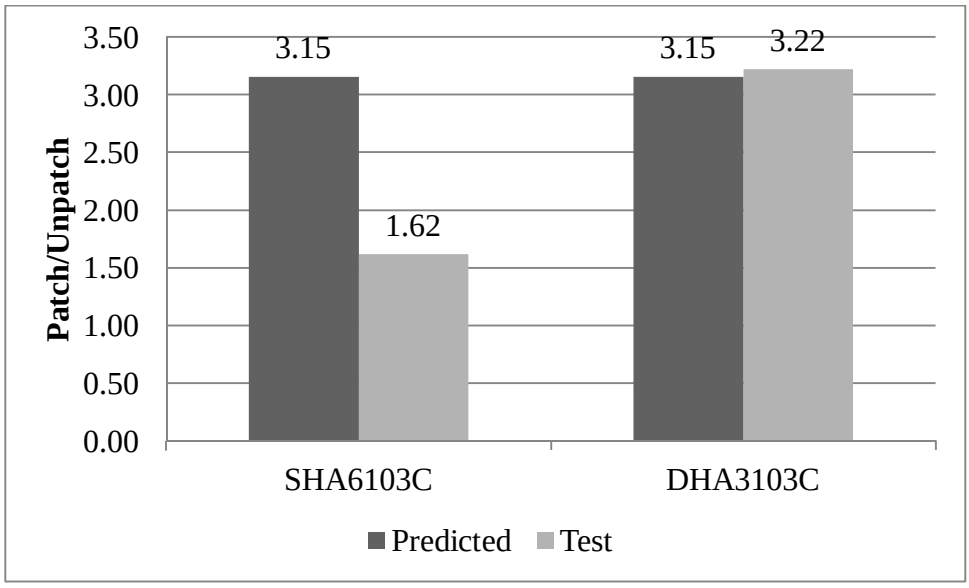

Figure 5-10 Effect of patch eccentricity

5.7 Conclusions

The following conclusions were drawn from the analytical model:

1) The effective thickness ratio has a significant effect on the effectiveness of the CFRP repairs.
2) Eccentricity of repair is the most significant factor in this model.
3) More research is needed into the effect of ETR on ΔSIF. Limited data in this area makes the model statistically insignificant.
4) More research is needed on the effect of pre-crack length to the effectiveness of FRP repairs.

6 Complementary Study: Effect of Pre-crack Length on CFRP Repair

Though much research has been done up to this point on the effectiveness of CFRP patches to extend fatigue life, little attention was paid to the pre-crack length and its effect on fatigue life extension. A further study was undertaken at the University of Alberta to examine the effect of pre-crack length on an FRP patch. A large portion of the work for this study is to be credited to undergraduate students David Murphy and Ashish Agrawal.

Table 6-1 shows the test matrix for this experiment. Two specimens were left unrepaired to act as a baseline to quantify the effectiveness of the repair. The unrepaired specimens numbered 1 and 2 are differentiated by the presence of beach marking in specimen 2. Since specimen used beach marking, specimen 2 was used as the baseline for all repaired specimen tests. The main parameter varied was the pre-crack length for the specimens in specimens 3, 4, 5, 6 and 7 with pre-crack lengths of 1.6, 5.0, 7.5, 10.0 and 15.0 mm respectively. The eccentricity of the repair and the use of a crack arrest stop hole were also considered in specimens 8 and 9.

Table 6-1 Experimental matrix for pre-crack length study

Specimen Number	*Pre-crack Length (mm)*	*Number of CFRP Layers*		*Special Notes*
		Front	*Back*	
1	-	0	0	no beach markings
2	-	0	0	Baseline - beach markings
3	1.6	2	2	
4	5.0	2	2	
5	7.5	2	2	
6	10.0	2	2	
7	15.0	2	2	
8	10.0	2	0	Single Sided Repair
9	10.0	2	2	Crack arrest hole

6.1 Methodology

The specimens tested were 300W steel flat bar with a nominal thickness and width of 10 mm and 90 mm, respectively. The specimen length was 500 mm. Figure 6-1 shows the overall specimen and repair design configuration.

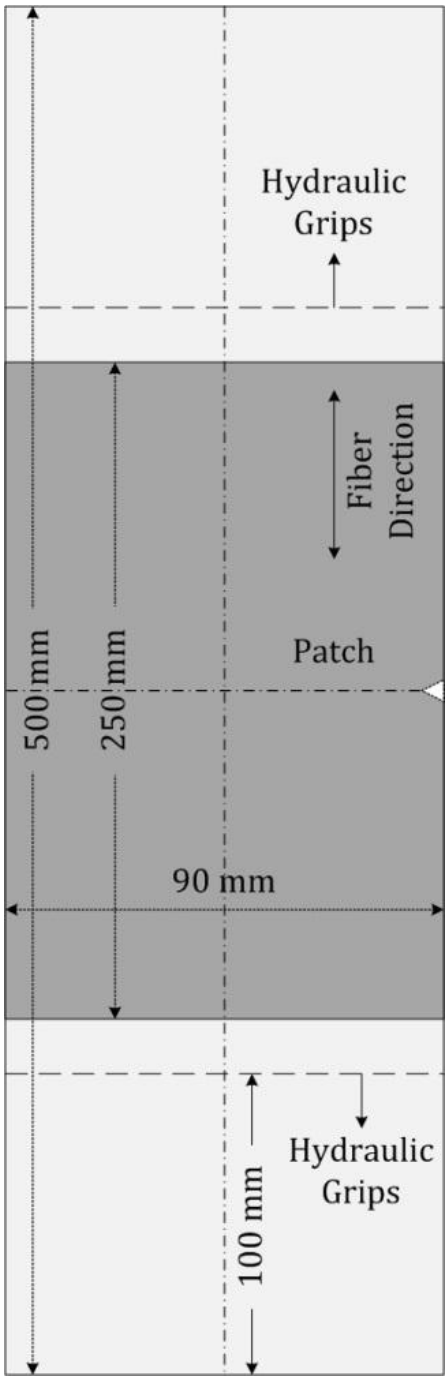

Figure 6-1 Specimen and repair design

The mill test report listed an average yield strength of 363 MPa and an average ultimate tensile strength of 491MPa for this batch. The CFRP patches consisted of SikaWrap® Hex 103C applied with a primer layer of Sikadur® 330 a fabric saturant of Sikadur® 300. The CFRP patch has an elastic modulus of 71,000 MPa and an ultimate strength of 662 MPa. The specimens were loaded with a nominal loading range of 20 kN to 200 kN, and an R value of 0.1 (see [6-1])

$$R = \frac{\sigma_{min}}{\sigma_{max}} \qquad [6\text{-}1]$$

where σ_{min} and σ_{max} are the minimum and maximum applied stresses respectively.

Table 6-2 shows the measured dimensions and applied loading ranges for each specimen. The loading ranges were applied based on the actual dimensions of the specimens to give a consistent stress range from one specimen to another.

Table 6-2 Dimensions and loading ranges for specimens

Specimen Number	*Notch Depth (mm)*	*Specimen Dimensions (mm)*		*Area (mm^2)*	*ETR*	*Load Range (kN)*	
		Average Thickness	*Avg. Width*			*Normal*	*Beach Mark*
1	1.40	9.44	89.29	843	-	20-202	N/A
2	1.41	9.22	89.14	822	-	20-197	108.5-197
3	1.40	9.23	88.97	821	0.141	20-197	108.5-197
4	1.43	9.26	89.29	817	0.140	20-196	108-196
5	1.36	9.37	88.27	827	0.139	20-198	109-198
6	1.40	9.50	88.48	841	0.137	20-202	111-202
7	1.34	9.29	89.02	827	0.140	20-198	109-198
8	1.42	9.37	88.54	829	0.139	20-199	109.5-199
9	1.41	9.43	89.04	839	0.138	20-201	110.5-201

For pre-cracking purposes and for Specimen 8, Figure 6-2 illustrates the notch design. The notches were modified from ASTM E-338-97. The standard called

for an 11 mm notch. However, this large notch size did not accommodate the small size of the specimens or the small pre-crack lengths considered in the study. For this reason the notch depth was modified to 1.4 mm. Notches were applied using a sharp 60° Swiss file. The notch was placed along one edge at mid span of the specimen, 250 mm from one end. Actual measured notch depths are recorded in Table 6-2.

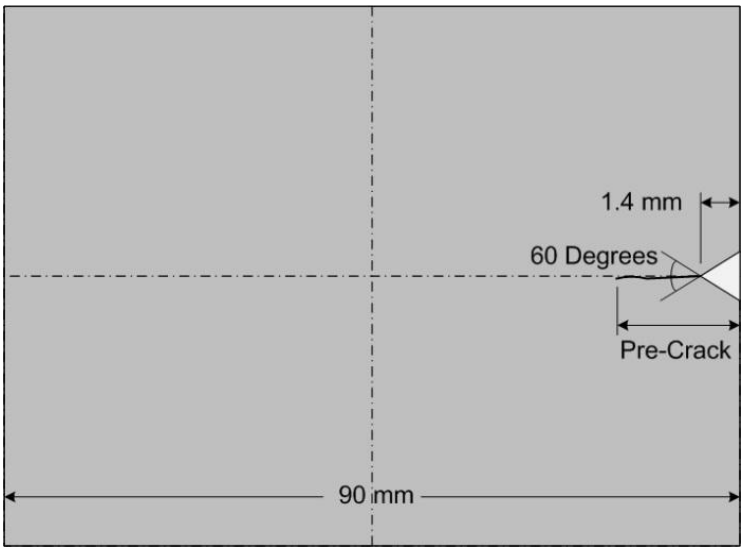

Figure 6-2 Steel notch design

All specimens were sandblasted to a uniform white metal finish, then loaded cyclically in the MTS 1000 test frame until the desired pre-crack length was reached. For pre-cracking purposes, and for the single sided repair, visual crack detection was aided by application of a lime whitewash to bare steel. The brittle nature of the whitewash caused it to flake away from the steel as the crack progressed, enhancing the visibility of the crack tip.

Once the desired pre-crack length was reached, the repair was applied. The repair used was the SikaWrap® Hex 103C system. The application procedure was the same as denoted in section 3.4.4. For Specimen 9, a 3.6 mm stop hole was introduced at the crack tip.

Once the repair patches were cured, a minimum of seven days at ambient room temperature, the specimens were again loaded cyclically in the MTS 1000 at 6

Hz, using the loading ranges specified in Table 6-2. Because visual detection of crack length was impossible once double sided repairs were applied, a technique called Beach Marking was used.

Beach marking is a natural phenomenon present in fatigue fractures, particularly fatigue fractures with variable loading ranges. As the crack propagates, the crack front will leave striations on the fracture surface (Anderson 2005). Individually, these striations can be very difficult to detect visually. Reducing the cyclic stress range for a predetermined number of cycles reduces the stress intensity at the crack tip, causing the crack propagation rate to decrease. With the decreased propagation rate, the striations are spaced more closely, causing a visible change in appearance of the fracture surface. The crack front at the point in which the reduced loading range is applied appears similar to a wave mark on a beach, hence the name "beach marking." This technique was used successfully by Liu et al. (2009b).

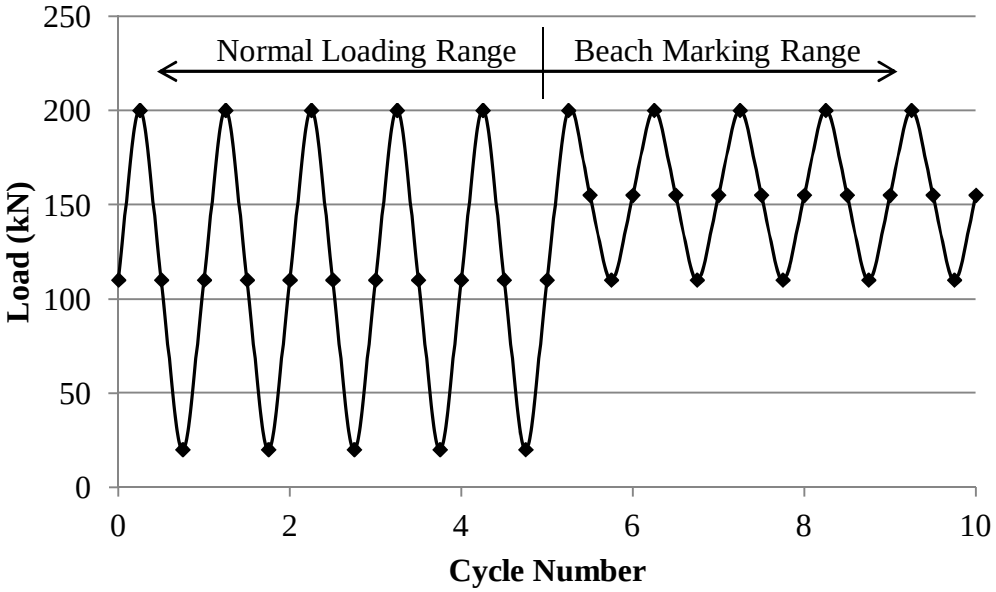

Figure 6-3 Loading ranges for normal loading and beach marking

Figure 6-3 shows the loading ranges and application of beach marking used in this study. While the nominal loading range was from 20 kN to 200 kN for the normal loading cycles, the cyclic loading for the beach marking cycles was run in the upper half of this loading range, from 110 kN to 90 kN. Specimens tested

with beach marking were loaded with an initial ratio of 20,000 cycles in the normal range followed by 5,000 cycles in the beach marking range. The number of cycles between beach marking cycles was reduced as the crack progressed to accommodate increased crack growth rate at longer crack lengths. An average of 5 beach marking cycles was used on the specimens to develop a detailed crack propagation curve.

The number of beach marking cycles was converted to equivalent cycles for constant amplitude loading at the normal loading range by use of the Linear Damage Model for Variable Amplitude Loading (Anderson 2005). According to this model, an equivalent constant amplitude stress range ($\Delta\sigma_{\text{eff}}$) can be determined from a variable amplitude loading scenario by the following equation:

$$\Delta\sigma_{eff} = \left(\frac{\sum_{i=1}^{n} \Delta\sigma_i^m N_i}{N_{tot}}\right)^{\frac{1}{m}} \quad \textbf{[6-2]}$$

where the subscript *i* denotes a discrete stress range and the subscript *tot* denotes the total number of cycles. The term *m* represents a material constant, which is taken as 3 for ferrite-pearlite steel (J. Barsom 1971). *N* represents the number of cycles. This can be rearranged to

$$\Delta\sigma_{eff}{}^m N_{tot} = \sum_{i=1}^{n} \Delta\sigma_i^m N_i \quad \textbf{[6-3]}$$

If we set the variable, effective stress, in the equation to equal the normal stress range [6-4], then the number of cycles becomes the variable as seen in equation [6-5].

$$\Delta\sigma_{\text{eff}} = \Delta\sigma_{normal} \quad \textbf{[6-4]}$$

$$N_{tot} = N_{eq} \quad \textbf{[6-5]}$$

Thus the equation becomes

$$\Delta\sigma_{normal}{}^m N_{eq} = \sum_{i=1}^{n} \Delta\sigma_i^m N_i \quad \textbf{[6-6]}$$

Since there are only two discrete stress ranges, this can be expanded to:

$$\Delta\sigma_{normal}{}^{m} N_{eq} = \Delta\sigma_{normal}{}^{m} N_{normal} + \Delta\sigma_{beach}{}^{m} N_{beach} \quad \textbf{[6-7]}$$

$$N_{eq} = \frac{\Delta\sigma_{normal}{}^{m} N_{normal} + \Delta\sigma_{beach}{}^{m} N_{beach}}{\Delta\sigma_{normal}} \quad \textbf{[6-8]}$$

$$N_{eq} = N_{normal} + \left(\frac{\Delta\sigma_{beach}}{\Delta\sigma_{normal}}\right)^{m} N_{beach} \quad \textbf{[6-9]}$$

Using equation [6-9], we can determine that the number of cycles for beach marking is equivalent to 0.125 times the number of cycles for the normal stress range. Therefore, each 5000 cycle beach marking period is equivalent to only 625 cycles for the normal stress range.

6.2 Results

Table 6-3shows the experimental results of this test program. In this table, l_p represents the pre-crack length. The third column explains any extra parameters considered. Specimen 8 is a single sided (SS) repair, while specimen 9 had a stop hole. Both specimens 8 and 9 were pre-cracked to 10 mm. N_{tot} represents the total number of cycles to failure of the specimen, while N_R represents the remaining number of cycles to failure after pre-crack length has been reached. The number of unrepaired cycles to failure was based on the remaining fatigue life of specimen 2, which had a total fatigue life of 138,600. Specimens 3, 4, 5, 6 and 7 all had double sided repairs. Specimen 8 had a single-sided repair and specimen 9 had a double sided repair with a drilled stop-hole at the crack tip. Both Specimens 8 and 9 were pre-cracked to 10 mm.

Table 6-3 Experimental results

Specimen	l_p *(mm)*	*Other Features*	N_{tot}	N_R *(unrepaired)*	N_R *(repaired)*	*Increased Life (%)*
3	1.6	-	215611	46600	110611	46
4	5.0	-	201354	20100	76354	41
5	7.5	-	231826	13600	55826	30
6	10.0	-	155560	8400	18560	7
7	15.0	-	134354	4000	19354	11
8	10.0	SS	152500	8400	10500	2
9	10.0	Hole	169132	8400	36132	20

Figure 6-4 shows the fracture surfaces for the specimens. Beach marking is clearly visible in this image. Crack lengths were determined by measuring the outermost edge of the crack front for each beach mark. This was recorded along with number of cycles at beach marking to create the crack propagation curves once the repairs were applied.

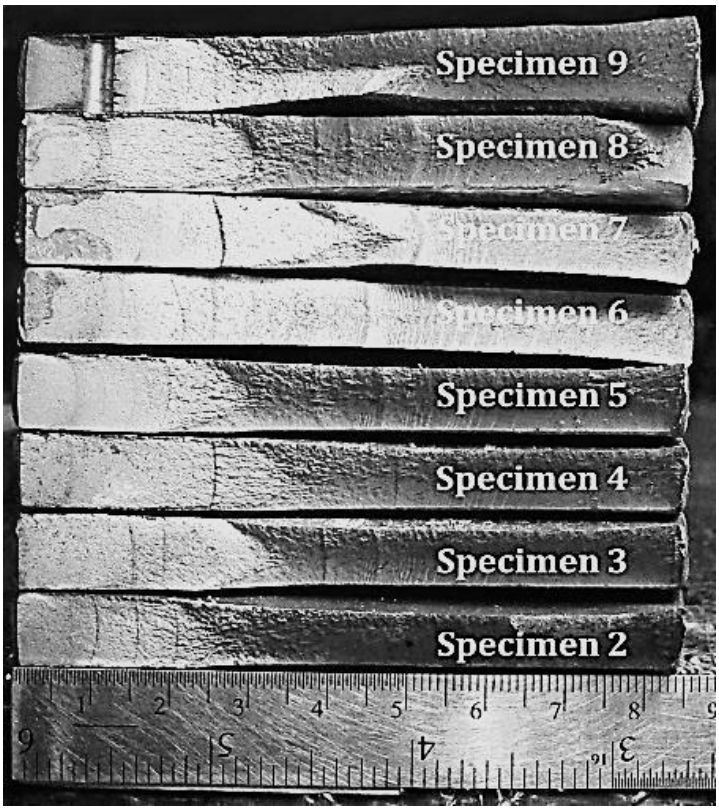

Figure 6-4 Fracture surfaces of Specimens 2 through 9

Figure 6-5 shows the crack propagation of the specimens. The horizontal axis represents the number of cycles (N_{tot}) while the vertical axis represents crack length. Though all specimens were prepared identically, microscopic differences between specimens and notches cause earlier crack initiation in some than in others.

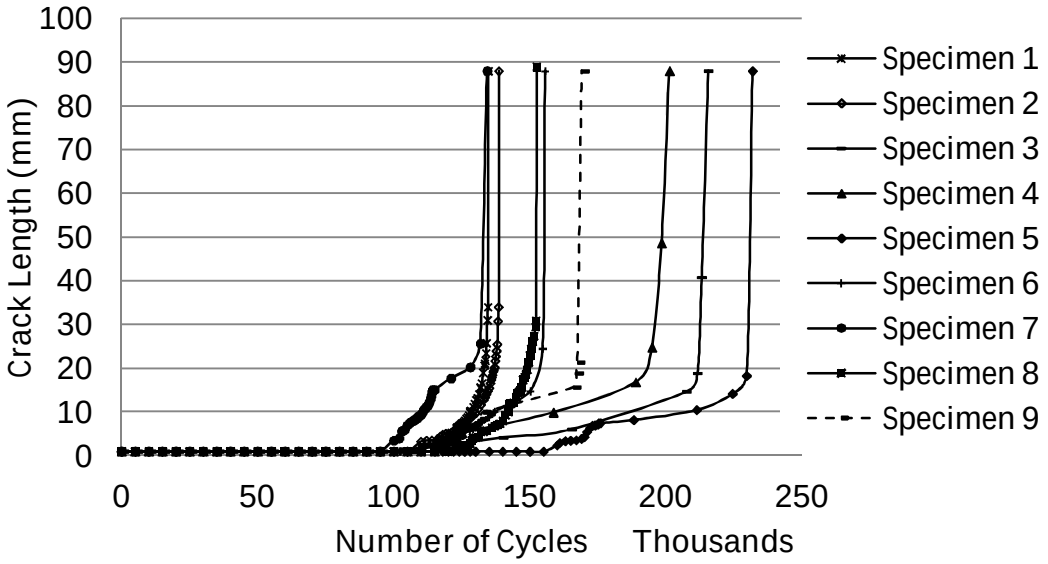

Figure 6-5 Crack propagation

Figure 6-6 is essentially the same as Figure 6-5, but this time with the crack length normalized at 3.5 mm. This was done to account for the differences in crack initiation time. Once initiated, crack propagation rate is predictable. By normalizing the crack length, the remaining fatigue life becomes comparable. The crack length was normalized by subtracting the number of cycles to reach a 3.5 mm crack length from the total number of cycles. Specimen 3, however, was pre-cracked to only 1.6 mm, and could not be normalized in the same manner; it did not have an unrepaired crack length of 3.5 mm at which to normalize. In this case, Specimen 2 was used as a standard. For the purposes of Figure 6-6, the number of cycles required from Specimen 2 to grow the crack to 3.5 mm was subtracted from Specimen 3's cycle count.

The failure mode for all specimens was adhesive debond and delamination within the FRP matrix. The patch debonded from the steel, beginning at midspan, and

spread towards the ends of the specimens. The extent of debonding could be detected by tapping the specimen with a metal object. The tone of the sound produced differed between the bonded and debonded areas. The bonded areas sounded sharp, where the debonded areas sounded hollow and tinny. When debonding reached the end of the patch, an audible crack sound could be heard. This coincided with a marked increase in crack growth rate for the specimen. Specimen 6 exhibited early debonding of the patch. The audible debond was heard at 154,695 cycles, while the test was stopped to switch stress ranges from the beach marking stress range to the normal stress range.

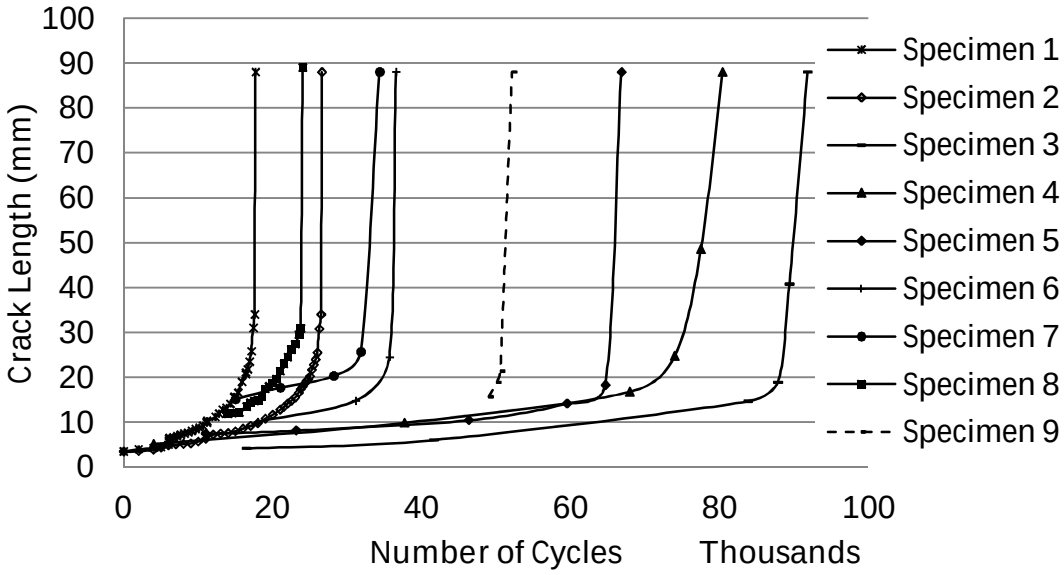

Figure 6-6 Crack propagation normalized at 3.5 mm crack length

For the main parameter, increase in crack length, the increase in fatigue life decreased as the pre-crack length increased. The most significant increase in fatigue life (46%) was for Specimen 3 with a pre-crack length of 1.6 mm and a N_R = 110611 cycles. This was followed by Specimen 4 with a 5.0 mm pre-crack at 41% increased fatigue life with N_R = 76,354. Specimen 5 with a 7.5 mm pre-crack had an increase in fatigue life of 30% at N_R = 55,826. Following this, came Specimen 7 with a pre-crack length of 15 mm and an increase in fatigue life of 11% at N_R = 19,354. Specimen 6 with a pre-crack of 10 mm, however, did not fit

in with this pattern of fatigue life changes; it experienced only a 7% increase in fatigue life.

Specimens 8 and 9 were based on Specimen 6 as a standard, with a pre-crack length of 10.0 mm for each specimen. Specimen 8 was a single sided repair, and showed an increase in fatigue life of only 2% over the unrepaired specimen at N_R = 10,500 cycles. Specimen 9 with a drilled stop hole at the crack tip had an increase in fatigue life of 20% with N_R = 36,132 cycles.

Figure 6-7 plots the effect of pre-crack length on fatigue life. The percent increase in fatigue life for Specimens 3, 4, 5 and 7, shown as diamonds, decreases nearly linearly as the pre-crack length increases. Specimen 6 is an outlier. Due to early adhesive debond; it falls well below the trend. Specimens 8 and 9 are plotted to show the comparative effects of the single sided and stop hole repair. The single sided repair was not nearly as effective with an increase of only 2%. The 2% increase in fatigue life experienced by the single sided repair is not a statistically significant improvement. Specimen 9 with the stop hole did not increase the fatigue life as expected. The increase in fatigue life is better than specimen 8; however it still is not an improvement compared to the expected fatigue life shown by the trend line through points 3, 4, 5 and 7.

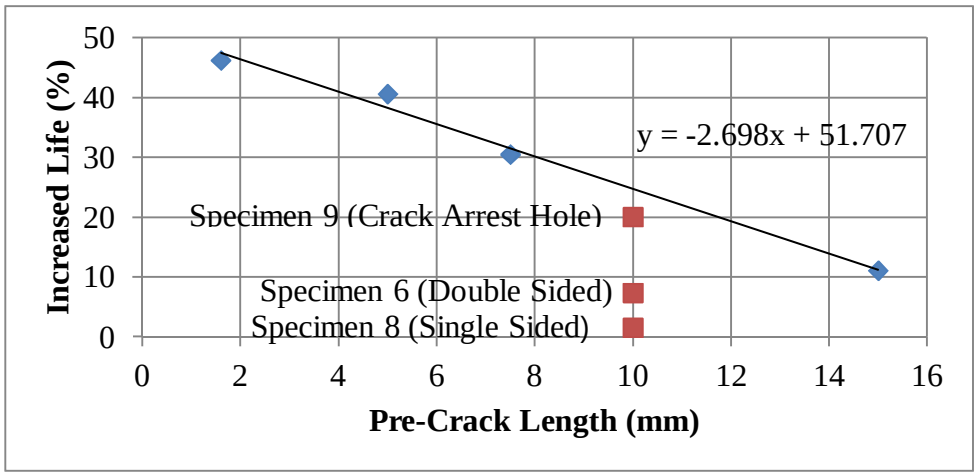

Figure 6-7 Effect of Pre-crack length on increase in fatigue life

6.3 Discussion of Results

6.3.1 Double Sided Repairs

The application of FRP repairs after a crack has been initiated did extend the fatigue life of the specimens. The extension of fatigue life decreases as the pre-crack length increases. This decrease was linear; from pre-crack length of 1.6 mm to 15.0 mm, the extension of fatigue life dropped from 46% to 11%. These specimens were all repaired on the same day, and using the same batch of Sikadur® 300 and Sikadur®330 mixtures. The same batch was used to ensure there were no inconsistencies between batch mix proportions. Specimen 6, with a 10.0 mm pre-crack, was the only double-sided repair to fall outside the linear variation due to its early adhesive debonding. Early debond of specimen 6 may have been a result of air bubbles in the adhesive layer, improper surface preparation of the steel or improper application of repair.

The linear relationship between the pre-crack length and extension of fatigue life is significant. It provides a basic understanding of the potential for CFRP repair in a real structure. It can help with the decision making process as to whether or not a repair is deemed necessary for a particular application. Once a crack is noticed, based on the stress ranges, crack length, and member geometry, a decision can be made whether a repair is necessary or if the cracked member should simply be replaced.

6.3.2 Single Sided Repair

The single sided repair did not provide a significant extension of fatigue life. There are several factors affecting the performance of the single-sided repair. The first is the total thickness of the repair itself. While all double sided repairs had two layers per side of the repair for a total of four layers of CFRP, Specimen 8 had only two layers on one side. This means that the total thickness of the CFRP patch is only half that for the double sided repairs. The capacity of the fibres, then, would also be less.

A second consideration is the number of shear planes. In a single sided repair, there is only one shear plane to transfer all load from the steel into the CFRP patch. A double sided repair, conversely, has two shear planes. This means that the shear stresses carried in that plane are double for the single sided repair than for an equivalent thickness double sided repair. Since failure occurred in adhesive debond for all double sided repaired specimens, doubling the stresses in the adhesive will reduce the capacity of the adhesive to maintain the necessary bond.

A third consideration is the creation of a loading eccentricity by moving the stress path to the side of the specimen rather than through the center. This eccentricity would cause there to be out-of-plane bending in the system. Out-of-plane bending could cause several interactions within the system, which may include: Prying forces within the adhesive layer; bending within the FRP layer; increased crack growth on the unrepaired side of the specimen (Lam et al. 2010) or other adverse effects. These effects cannot be determined properly without further modelling and investigation.

6.3.3 Stop Hole Repair

Specimen 9 used a combination of a stop-hole repair and double sided CFRP repair. The extension of fatigue life for this specimen was 20% which was less than the expected linear relation for the double sided repairs. However, the expected extension is of 24.5% (Figure 6-7), which is not significantly higher. It would appear that the combination of stop hole and double sided repair had no effect on the fatigue life extension over the double sided repair.

The poorer than expected improvement may be due to the fact that the stop hole was undersized. The crack repair method from *Engineering and Design: Inspecition, Evaluation, and Repair of Hydraulic Steel Structures* (US Army Corps of Engineers 2001) provides a series of linear elastic fracture mechanics equations to determine the optimal crack blunting stop hole radius. For an edge crack on a plate, in pure tension, the equation for stress intensity factor (K_I) is:

$$K_I = 1.12\,\sigma\sqrt{\pi a}\cdot k\left(\frac{a}{b}\right) \qquad \textbf{[6-10]}$$

where σ is the nominal stress applied and $k(a/b)$ is a dimensionless constant which can be determined from Figure 6-8 shown below. From the figure, $k(a/b)$ was calculated to be 1.090. Therefore, using Equation [6-10] yielded a value of stress intensity range of ΔK_I = 46.8 MPa$\sqrt{\text{m}}$ for the stress range applied.

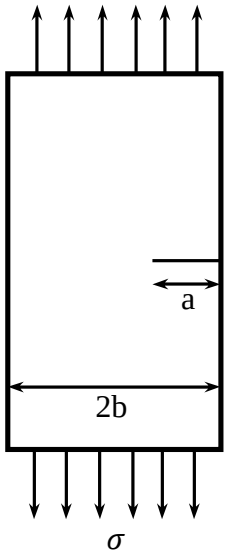

a/b	$k(a/b)$
0.10	1.03
0.20	1.07
0.30	1.15
0.40	1.22
0.50	1.35
0.60	1.50
0.70	1.69
0.80	1.91
0.90	2.20
1.00	2.55

Figure 6-8 Linear Elastic Fracture Elastics constants for edge cracked plate in tension (Barsom and Rolfe 1987)

The stress intensity was then put into the Equation [6-11] to determine the radius of the recommended stop hole.

$$\frac{\Delta K_I}{\sqrt{r}} = 26.7\sqrt{\sigma_y} \qquad \textbf{[6-11]}$$

where ΔK_I is the stress range in MPa$\sqrt{\text{m}}$, r is the radius of the hole in meters and σ_y is the yield strength of the steel in MPa. This yields a stop hole radius of r = 0.0078 m or 7.8 mm, centred at the crack tip. This was modified to a 3.6 mm diameter hole in consideration to the short width of the specimens.

The stress concentration at the crack tip, though blunted by the 3.6 mm diameter stop hole, may have still been high enough to induce further crack initiation. The radius of the stop hole has a great effect on the stress concentration at the crack tip. This can be shown by looking at the cope radii in the study by Yam and Cheng (1990). As the cope radius increased, the stress concentration in the study decreased drastically.

The US Army Corps of Engineers (2001) further specifies that if the stress range is greater than 40 MPa, the radius required to blunt the crack tip may be prohibitively large. In these cases, the recommendation is to drill a hole big enough to blunt the crack tip, and to repair the remaining crack by welding or a bolted cover plate. While the CFRP repair may be considered a form of cover plate, it is possible that due to the very small nature of the hole drilled, that the entire crack tip was not effectively removed by the drilling. If that is the case, then the repair would have acted identically to a repair where no stop hole was present. This seems to be the case shown in Figure 6-7. Unfortunately, since the equivalent 10 mm pre-crack double-sided repair (Specimen 6) did not give valid data due to early adhesive debonding; this cannot be stated with any certainty. More research into the phenomenon is needed.

6.4 Conclusions

Nine steel coupons were notched and failed under fatigue loading. Specimens 1 and 2 were unrepaired and used as benchmarks for the effectiveness of the repair. The remaining seven were repaired by application of CFRP Patches after a specific pre-crack length had been reached. The patch applied was a two-ply application of SilaWrap® Hex 103C. Specimens 3, 4, 5, 6, and 7 were all repaired using a double sided CFRP patch repair after reaching pre-crack lengths of 1.6 mm, 5.0 mm, 7.5 mm, 10.0 mm and 15.0 mm respectively. The percent increase in fatigue life for these specimens was 46%, 41%, 30%, 7%, and 11% respectively. Specimen 6 experienced premature adhesive debond due to

imperfections in the repair. The increase of fatigue life for specimens 3, 4, 5 and 7 varied linearly, decreasing as the crack length increased.

Specimen 8 was repaired on only one side with the same configuration of patch mentioned above. The increase in fatigue life observed for this specimen was only 2% over an unrepaired specimen. This is not a statistically significant increase in fatigue life. Poor increase in fatigue life is due to increased shear at the adhesive interface, out-of-plane bending in the specimen due to stress path eccentricity and possible prying action within the adhesive layer. A single sided repair appears not to be a viable option for rehabilitation of real plate structures. When feasible, any CFRP repair applied should be double sided.

Specimen 9 was repaired using a 3.6 mm diameter stop hole centred at the crack tip. This was then combined with a double sided repair similar to those used in Specimens 3 to 7. The increase in fatigue life was 20%. This increase was similar to the expected increase for a 10.0 mm pre-crack length. The presence of a stop hole appeared to have no effect on the effectiveness of the repair. It is possible that due to the small size of the stop hole used, the entire crack tip was not blunted. More research is needed into this topic. No test was done as a control for an unrepaired stop-hole. Also, since Specimen 6 failed early, there is no valid control for a double sided CFRP repair with the same pre-crack length but no stop hole.

Beach marking was used effectively as a method of measuring crack length and crack propagation rate in the double sided repaired specimens. It allowed accurate and precise measurement of the crack front at pre-specified cycle counts. The fracture surface must be visible and accessible to use this method of crack measurement; the measurements can only be taken after the specimen has already failed. This makes it a good method for experimental use only.

CFRP patching can be a cost effective and rapid repair method for fatigue cracked steel structures. A linear relationship exists between the fatigue life extension and

length of crack at the time of the repair application. Using this relationship, upon fatigue crack detection, the crack length can be used to determine the expected fatigue life extension if repaired with a double sided CFRP patch. This information will aid engineers in determining the most cost-effective and efficient method of fatigue crack remediation.

More research is required into the phenomenon to be fully implemented in practice. This research would include testing specimens of different initial geometries, patch configurations and loading conditions at various pre-crack lengths. The further data that would be acquired from these tests can be used to develop a comprehensive model for the effect of pre-crack length that can be applied to most fatigue cases.

7 Summary, Conclusions and Recommendations

7.1 Summary

Six full-scale specimens were tested. Fatigue cracks were initiated, grown to 10 mm and subsequently repaired using adhesively bonded CFRP patches. The patches were applied with three orientations; along the longitudinal axis of the beam (0°), angled at 45° to the longitudinal axis, and multidirectional (45°, 0°, 90°). Single sided repairs and double sided repairs were considered. The thickness of repair was also varied.

In all cases the main failure mode was debonding in the adhesive layer. Doubling the thickness of the patch did increase the fatigue life, but not as much as expected. The double sided repair was superior to the single sided repair with equivalent effective thickness of CFRP. The crack propagation angle for the double sided repair shifted towards the vertical axis by more than 20° from the unrepaired state. This shift was more than could be explained by simple mathematical material models, suggesting a complex interaction between the CFRP patch and the web of the beam.

A Linear Elastic Fracture Mechanics analytical study was carried out to predict the fatigue life of the specimens. The study combined elements from two previous works. The bare specimen fatigue prediction model was taken from work by Yam and Cheng (1988, 1990). This was combined with a stress intensity factor modification which was calculated based on work by Lam et al. (2010). The resulting predictions were consistently under predicted for the single sided repairs at approximately 60% test to predicted due to premature adhesive failure caused, in part, by out of plane bending in the specimens. It was, however, a very good prediction for fatigue life of the double sided repair with a test/predicted ratio of 1.05.

A further experimental study was carried out on nine small-scale specimens to determine the effect of pre-crack length on repaired specimens. The specimens

were repaired with double sided repairs. The crack length was detected using beach marking, which was a very effective method of determining the crack length. The study found a linear relationship between the pre-crack length and the fatigue life extension experienced by the specimens. As the pre-crack length increased, the fatigue life extension decreased.

7.2 Conclusions

Based on the investigations presented herein, the following conclusions were drawn.

1) The weak link of the CFRP repairs was the adhesive bond. Failure in every case, full-scale and small-scale, took place primarily in the adhesive layer. The repairs therefore could not develop their full strength, particularly the single sided repairs, which had higher adhesive stresses.
2) Double sided repairs were far superior to single sided repairs.
3) Angled repairs are more effective, particularly if perpendicular to the crack propagation angle.
4) Multi-directional repairs are more versatile, taking on strength from other fibre directions as the crack length increases.
5) Increasing the patch thickness increased the fatigue life, though not proportionally to the increase in ETR.
6) The large shift in crack angle on the double sided repair suggests a complex interaction between CFRP and steel which bears further investigation.
7) The analytical model was effective for the double sided repair. The single sided repairs failed in the adhesive layer and did not develop full strength in the CFRP patch.
8) Beach marking is a very effective method for determining of crack length on double sided specimens. This method is limited for use by the fact that crack length cannot be detected in real time, but only after the specimen has failed and the fracture surface is available for visual inspection.

9) The benefit of a CFRP patch decreases as the pre-crack length increases. This relationship is nearly linear.

7.3 Recommended Future Works

The following works are recommended for future investigation in order to develop a complete understanding of the behaviour of CFRP patches applied to coped beams.

1) A parametric study of coped beams varying the adhesive and CFRP patch type should be conducted. This study should focus primarily on double sided repairs.
2) A study should be undertaken to determine an effective monitoring method to detect crack length on double sided repaired beams
3) A further parametric study on the effect of pre-crack length should be undertaken varying the plate width and thickness of the specimens.
4) A study should be undertaken to explore the difference in behaviour of patches with equivalent ETR, but which are made from materials with different moduli of elasticity and patch thicknesses.
5) More analysis should be done to determine the change in stress intensity factor of cracked steel with different patch geometries and fibre orientations.

References

Alberta Infrastructure and Transportation. *Bridge Design Criteria: Version 2.0.* Edmonton, Alberta: Alberta Infrastructure and Transportation, 2007.

Albrecht, P, and K Yamada. "Rapid Calculation of Stress Intensity Fators." *Journal of the Structural Division ASCE* 103, no. ST2 (February 1977): 377-389.

Anderson, T.L. *Fracture Mechanics: Fundamentals and Applications.* 3rd. Boca Raton, Florida: CRC Press, 2005.

ASTM A 370-02. "Standard test methods and definitions for mechanical testing of steel products." West Conshohocken: ASTM International, 2002.

ASTM D 3039/D 3039M-00. "Standard test method for tensile properties of polymer matrix composite materials." West Conshohocken: ASTM International, 2006.

ASTM E 338-97, . "Standard notch method of sharp-notch tension testing of high-strength sheet materials." West Conshohocken, PA: American Society for Testing and Materials, 2003.

Barsom, J. M., and S. T. Rolfe. *Fracture and Fatigue Control in Structures.* Englewood Cliffs, NJ: Prentice-Hall, 1987.

Barsom, J.M. "Fatigue crack propagation in Steels of Various Yield Strengths." *Transactions, American Society of Mechanical Engineers, Journal of Engineering for Industry* 93 Series B, no. 4 (1971).

Bassetti, Andrea, Alain Nussbaumer, and Pierluigi Colombi. "Repair of riveted bridge members damaged by fatigue using CFRP materials." *Advanced FRP Materials for Civil Structures*, October 2000: 33-42.

Beer, Ferdinand P, and E. Russell Jr. Johnston. *Mechanics of Materials.* 2nd. London: McGraw Hill, 1992.

Bocciarelli, Massimiliano, Pierluigi Colombi, Guilia Fava, and Carlo Poggi. "Fatigue performance of tensile steel members strengthened with CFRP plates." *Composite Structures* 87 (2009): 334-343.

Canadian Standards Association. *Canadian Highway Bridge Design Code.* Ontario, 2006.

Cheng, J. J. Roger. "Design of steel beams with end copes." *Journal of Construction Steel Research* 25 (1993): 3-22.

Dawood, M., S. Rizkalla, and E. Sumner. "Fatigue and overloading behaviour of steel-concrete composite flexural memnrs strengthened with high modulus CFRP materials." *Journal of Composites for Construction* 11, no. 6 (2007): 659-669.

Dawood, Mina, Murthy Guddati, and Sami Rizkalla. "Effective splices for a carbon fibre reinforced polymer." *Transportation Research Record: Journal of the Transportation Research Board* 2131 (2009): 125-133.

Deng, J., and M. M. K. Lee. "Adhesive Bonding in Steel Beams strengthened with CFRP." *Structures and Buildings* 162, no. SB1 (2009): 241-249.

Environment Canada and Health Canada. "Priority Substances List Assessment Report - Road Salts." 2001.

Gagnon, Mychèle, Valérie Gaudreault, and Donald Overton. *Analysis in Brief: Age of Public Infrastrcture: A Provincial Prospective.* Analytical Paper, Investment and capital Stock Division, Statistics Canada, Ottawa: Minister of Industry, 2008.

Hammad, Amin, Jianxia Yan, and Behzad Mostofi. "Recent Development of Breidge Management Systems in Canada." *Transportation Association of Canada.* Transportation Association of Canada. 2007. http://www.tac-atc.ca/english/resourcecentre/readingroom/conference/conf2007/docs/s7/hammad.pdf (accessed December 19, 2010).

Jones, Sean C., and Scott A. Civjan. "Aplication of Fiber Reinforced Polymer Overlays to Extend Steel Fatigue Life." *Journal of Composites for*

Construction (American Society for Civil Engineering) 7, no. 4 (November 2003): 331-339.

Kennedy, Gaylene D., and J. J. Roger Cheng. "Repair of cracked steel elements using composite fiver patching." Structural Engineering Report, Department of Civil and Environmental Engineering, University of Alberta, Edmonton, 1998.

Lam, Angus C. C., J. J. Roger Cheng, Michael C. H. Yam, and Gaylene D. Kennedy. "Repair of steel structures by bonded carbobn fibre reinforced polymer patching: experimental and numerical study of carbon fibre reinforced polymer - steel double lap joints under tensile loading." *Canadian Jouirnal of Civil Engineering* 34 (2007): 1542-1553.

Lam, Angus C. C., Michael C. H. Yam, J. J. Roger Cheng, and Gayleen D. Kennedy. "Study of stress intensity factor of a cracked steel plae with a single-side CFRP composite patching." *Journal of Composites for Construction*, November/December 2010: 791-803.

Lam, Chi Chiu Angus, and J. J. Roger Cheng. "Repair of cracked steel structures by FRP patching." Structural Engineering Report 285, Department of Civil and Environmental Engineering, University of Alberta, Edmonton, 2008, 250.

Linghoff, Dag, Reza Hagani, and Mohammad Al-Emrani. "Carbon-fibre composites for strengthening steel structures." *Thin-Walled Structures* 47 (2009): 1048-1058.

Liu, Hongbo, Riadh Al-Mahaidi, and Xiao-Ling Zhao. "Experimental study of fatigue crack behaviour in adhesively reinforced steel structures." *Composite Structures* 90 (2009b): 12-20.

Liu, Hongbo, Xiao-Ling Zhao, and Riadh Al-Mahaidi. "Boundary element analysis of CFRP reinforced steel plates." *Composite Structures* 91 (2009a): 74-83.

Liu, Hongbo, Zhigang Xiao, Xiao-Ling Zhao, and Riadh Al-Mahaidi. "Prediction of fatigue life for CFRP strengthened steel plates." *Thin Walled Structures* 47 (2009c): 1069-1077.

Naboulsi, S., and S Mall. "Modelling of a cracked metallic structure with bonded composite patch using the three layer technique." *Composite Structures*, 1996: 295-308.

Photiou, N. K., L. C. Holloway, and M. K. Chryssanthopoulos. "Strengthening of an artificially degraded steel beam utilising a carbon/glass composite system." *Construction and Building Materials* 20 (2006): 11-21.

Rice, J. R. "A path independent integral and approximate analysis of strain concentration by notches and cracks." *Journal of Applied Mechanics* 35 (1968): 379-386.

Roberge, Pierre R. *Corrosion Engineering: Principles and Practice.* McGraw Hill, 2008.

Roeder, Charles W., Gregory MacRae, Amy Leland, and Athena Rospo. "Extending the fatigue life of riveted coped stringer connections." *Journal of Brige Engineering* 10, no. 1 (January 2005): 69-76.

Sika Canada Inc. "Sika (R) 300." *Product Data Sheet.* July 2007.

Sloan, F. E., and J. B. Talbot. "Corrosion of graphite-fiber-reinforced composites I - Galvanic coupling damage." *Corrosion* (National Association of Corrosion Engineeers), October 1992: 830-838.

Sloan, F. E., and J. B. Talbot. "Corrosion of graphite-fiber-reinforced composites I - Galvanic coupling damage." *Corrosion* (National Association of Corrosion Engineeers), October 1992: 830-838.

Taljsten, Bjorn, Christian Skodborg Hansen, and Jacob Wittrup Schmidt. "Strengthening of old metallic structures in fatigue with prestressed and non-prestressed CFRP laminates." *Construction and Building Materials* 23 (2009): 1665-1677.

Tavakkolizadeh, M., and H. Saadatmanesh. "Repair of damaged steel-concrete composite girders using carbon fibre-reinforced polymer sheets." *Journal of Composites for construction* (ASCE) 7, no. 4 (2003a): 311-322.

Tavakkolizadeh, M., and H. Saadatmanesh. "Strengthening of steel-concrete composite girders using carbon fibre reinforced polymer sheets." *Journal of Structural Engineering* (ASCE) 129, no. 1 (n.d.): 30-40.

Tavakkolizadeh, Mohammadreza, and Hamid Saadatmanesh. "Galvanic corrosion of carbon and steel in agressive environments." *Journal of Composites for Construction* 5, no. 3 (August 2001): 200-210.

Tavakkolizdeh, M., and H Saadatmanesh. "Fatigue strength of steel girders strengthened with carbon fibre reinforced polymers." *Journal of Structural Engineering* 129, no. 2 (February 2003b): 186-196.

Tucker, Wayne C., and Richard Brown. "blister formation on graphite/polymer composites coupled galvanically with steel in seawater." *Journal of Composite Materials* (Technomic Publishing Co., Inc.) 23 (April 1989): 389-395.

Tucker, Wayne C., Richard Brown, and Laureen Russell. "Corrosion between a graphite/polymer composite and metals." *Journal of Composite Materials* (Technomic Publishing Co., Inc.) 24 (January 1990): 92-102.

US Army Corps of Engineers. *Engineering and Design: Inspection, evaluation, and repair of hydraulic steel structures.* US Army Corps of Engineers, 2001.

Yam, Michael C. H., and J. J. Roger Cheng. "Fatigue Strength of Coped Steel Beams." *Journal of Structural Engineering* (ASCE) 116, no. 9 (September 1990): 2447-2463.

Yam, Michael C. H., and J. J. Roger Cheng. "Fatigue Strength of Coped Steel Beams." Structural Engineering Report 160, Department of Civil Engineering, University of Alberta, Edmonton, 1988, 101.

Zhao, Xiao-Ling, and Lei Zhang. "State-of-the-art review on FRP strengthened steel structures." *Engineering Structures* (Elsevier Ltd.) 29 (2007): 1808-1823.